Stacks of high temperature superconducting tape as trapped field magnets for energy applications

Algirdas Baskys
Department of Materials Science and Metallurgy
University of Cambridge

This dissertation is submitted for the degree of
Doctor of Philosophy

Robinson College April 2017

I would like to dedicate this thesis to my family and friends. I’d like to express gratitude to my loving parents Algirdas and Janina and my sister Lina for their unwavering support.

Declaration

I hereby declare that except where specific reference is made to the work of others, the contents of this dissertation are original and have not been submitted in whole or in part for consideration for any other degree or qualification in this, or any other University. This dissertation is the result of my own work and includes nothing which is the outcome of work done in collaboration, except where specifically indicated in the text. This dissertation contains less than 60,000 words including summary/abstract, tables, footnotes and appendices, but excluding table of contents, photographs, diagrams, figure captions, list of figures/diagrams, list of abbreviations/acronyms, bibliography and acknowledgements.

Algirdas Baskys
April 2017

Acknowledgements

I would like to thank all of those who has helped and supported me over the four years. First and foremost, I'd like to thank to my supervisor Prof. Bartek Glowacki for all the invaluable support, guidance and advice he has given me during the course of my PhD. I would also like to express sincere gratitude to Dr Anup Patel fruitful discussions, encouragement, guidance, support and research material kindly provided.

Thank you goes to Dr Simon Hopkins and Tom Mitchel-Williams for all the stimulating conversations and help with the experimental equipment, Prof. Archie Campbell for enlightening discussions on the topic of crossed field demagnetisation of trapped field magnets.

I would like to acknowledge Dr Victor Manuel Rodriguez Zermeno and Shengnan Zou for collaborative work described in sections 5.3.1 and 4.7 respectively.

I would also like to thank Xiao Teng, Dr Rumen Tumov, Dr Vasilka Tsaneva and all students that joined our small research group over the last four years for creating a fun and sociable environment.

Abstract

The world demand for energy is estimated to increase by up to 70% from 2016 to 2040. To meet this demand in a sustainable way, the power density of electric motors and generators can be increased by using superconducting materials. In particular, trapped field superconducting magnets, where the field is generated by a circulating persistent current in the sample, can create magnetic fields an order of magnitude higher than possible using conventional ferromagnets, thus increasing the power density of motors and generators. This is of great interest where added weight comes at a premium, such as for naval propulsion motors, wind generators and motors/generators for future electric aircraft.

This work investigates the suitability of stacked tape layers of second generation high temperature superconductors (HTS), such as $YBa_2Cu_3O_{7-x}$ (YBCO) for trapped field applications. The present limits for trapped field magnitude have been determined, which provide a basis for the optimization of pulsed field magnetization techniques for in-situ magnetization in motors and generators. Trapped fields were increased by optimising the magnetic pulse sequence, using thermally conductive material to reduce temperature rise during pulse and changing the duration of the magnetic field pulse.

Finite element method computer modelling was used to model and predict the behaviour of the trapped field magnets made of HTS tape with good agreement to experiment for both field cooling and pulsed field magnetisation. The models rely on critical current data for the HTS tape and its dependence on magnetic field and temperature. For this reason, a critical current testing facility was developed and constructed as a part of this work capable of measuring critical current up to 900 A, magnetic field of 1.5 T and down to temperatures of ~10 K in forced and dynamically controlled helium vapour flow.

Lastly, first steps into scaling up by pulse magnetising an array of HTS tape stacks were made, allowing for larger overall trapped flux values. Such an array exhibits geometry, similar to what is going to be used in a functional motor prototype being developed in our research group (Applied Superconductivity and Cryoscience Group, ASCG).

The work done culminated in the highest trapped field achieved to date using both field cooling (13.4 T between two stacks) and pulsed field magnetization (2.1 T above a single stack), for this type of trapped field magnet.

Contents

List of Figures

List of Tables

Nomenclature and abbreviations

(RE)BCO or (RE)123	(RE)$Ba_2Cu_3O_{7-x}$ where RE denotes a rare-earth element
AC	Alternating current (time-varying)
BSCCO	A class of compounds with formula $Bi_2Sr_2Ca_{n-1}Cu_nO2_{n+4+x}$, n = 1-3
DC	Direct current (static in time)
FC	Field cooling
FEM	Finite element method
FM	Ferromagnetic material
HTS	High temperature superconductor
IMRA	Iterative magnetization with reducing amplitudes (using pulsed field)
LHe	Liquid helium
LN_2	Liquid nitrogen
LTS	Low temperature superconductor
MPSC	Multi-pulse technique with step-wise cooling
MRI	Magnetic resonance imaging
NMR	Nuclear magnetic resonance
OD/ID	Outer/Inner diameter
PFM	Pulsed field magnetization
RT	Room temperature
SC	Superconductor
SF	Self-field
TFM	Trapped field magnet
ZFC	Zero-field cooling

List of symbols

a, b, c	Crystallographic axes
B	Magnetic flux density [T]
C	Heat capacity [J/(kg K)]
e	Charge of an electron ~1.60×10^{-19} [C]
E, E_0	Electric field [V/m]; electric field criterion [V/m]
F	Force per unit volume [N/m^3]
H	Magnetic field strength [A/m]
h	Plank constant ~6.63×10^{-34} [m^2 kg/s]
I, I_c	Current [A]; critical current [A]
J, J_c	Current density [A/m^2]; critical current density [A/m^2]
J_e	Engineering critical current density [A/m^2]
k	Thermal conductivity [W m^{-1} K^{-1}]; Boltzmann constant ~1.38×10^{-23} [J/K]
l	Length [m]
M	Magnetisation [A/m]
n	Exponent of E-J power law; number density [m^{-3}]
Q_V	Volumetric heat flux [W/m^3]
t	Time [s]
T, T_c	Temperature [K]; critical temperature [K]
U	Activation energy [J]
θ, ϕ	Rotational and tilt angles respectively [degrees]
λ	London penetration depth [m]
μ_0, μ_r	Vacuum permeability $4\pi\times10^{-7}$ [N/A^2]; relative permeability
ξ	Coherence length [m]
ρ	Material density [kg/m^3]; electrical resistivity [Ω m]
σ	Electrical conductivity [S/m]
Φ	Magnetic flux [Wb]

Chapter 1 Introduction

1.1 Short historical perspective

Superconductivity is a phenomenon where in some materials below a certain critical temperature and magnetic field, the material loses any DC electrical resistance and expels magnetic fields. Since the discovery of superconductivity by Heike Kamerlingh Onnes in 1911 [1] it was envisaged that superconductors will be used to create sustained, high strength magnetic fields. Static magnetic fields beyond several tesla were hard to achieve using regular metallic conductors because of large energy losses due to Joule heating.

However, it was soon discovered that most single chemical element superconductors have very low transition temperatures and can only carry small current densities, before the material reverts to its non-superconducting state. It was later understood that it is not the current itself but the magnetic field, created by the current (self-field) or other applied field that destroys superconductivity upon reaching a limit, referred to as the critical field, H_c. This behaviour is typical of type-I superconductors. In contrast, most superconducting metal alloys, intermetallics and ceramics are classified as type-II superconductors. Type-II superconductors have two critical applied field values. When the lower critical field is exceeded the magnetic field can penetrate the superconductor by formation of quantised magnetic flux vortices, however the material remains superconductive until the upper critical field is reached (typically a much higher value than in type-I superconductors). As a result, only type-II superconductors are considered for most applications as they can operate at much higher magnetic fields.

Type-II superconductors such as NbTi and Nb_3Sn were amongst the first practical superconductors capable of generating fields in excess of 10 tesla. The critical surface below which a material superconducts, is shown Figure 1.1 (for NbTi) with relation to pure Ti and Nb.

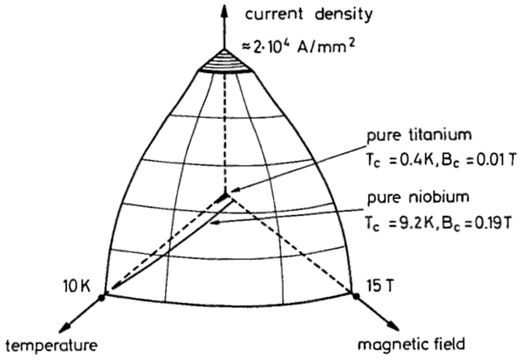

Figure 1.1– Critical surface of NbTi, niobium and titanium. Reproduced from [2].

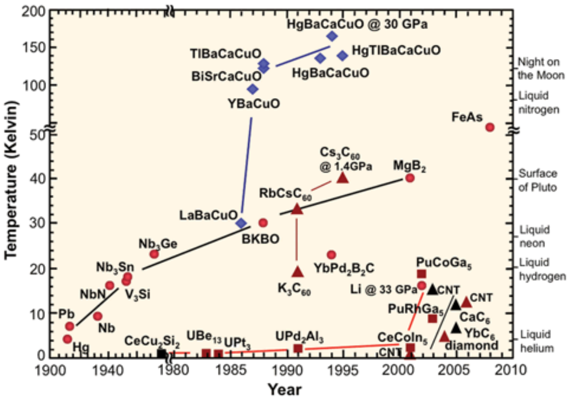

Figure 1.2– Superconducting materials and the dates of their discovery. From [3].

Nevertheless, the increase in the transition temperature for these alloys and compounds was only marginal (see Figure 1.2) and the superconductors still needed to be cooled with liquid helium making the operation of the superconducting systems complicated and costly. It was widely believed that superconductivity is not possible above 30 K, when in 1986 a new class of superconductors based on cuprate-perovskite ceramic materials was discovered [4] which quickly led to increase of critical temperature above LN_2 temperature. One of the new materials was $YBa_2Cu_3O_{7-x}$ [5], often abbreviated simply as YBCO or Y123, part of larger (RE)123 family where RE stands for a rare-earth element. Having a critical temperature of 92 K, YBCO is superconductive at liquid nitrogen temperatures, making it attractive for practical applications: power transmission, magnetic field sources, magnetic levitation, drug delivery, cathodes for magnetron sputtering, etc. However, many materials science challenges had to be overcome for this to come true.

1.2 Definition and basic properties of a superconductor

Superconducting materials have two defining properties:

I. Zero resistivity below a certain temperature, magnetic field and DC current density (below a critical surface, as in Figure 1.1).

II. Expulsion of magnetic field from the material, also called the Meissner effect. The Meissner effect cannot be explained by zero resistivity alone.

Zero resistivity has been verified by a number of experiments indicating that the life-time of a supercurrent within a closed loop of a superconductor exceeds 10^4 years, giving an upper bound resistivity of 10^{-22} Ω m [6].

The Meissner effect was first explained by the London brothers [7], who showed that the electromagnetic free energy is minimised, provided that:

$$\nabla^2\mathbf{H} = \lambda^{-2}\mathbf{H} \tag{1.1}$$

This shows that the magnetic field within the superconductor decays exponentially from the value B_0 at the surface (see Figure 1.3):

$$H = H_0 \exp\left(-\frac{x}{\lambda}\right) \tag{1.2}$$

Where λ is the characteristic London penetration depth. The shielding of the magnetic field is caused by the supercurrent circulating around the circumference of the sample, within thickness ~λ of the sample surface. This behaviour is maintained until the external magnetic field exceeds a critical value H_c (ignoring geometric effects) when the superconductor transitions to normal state. However, there is another type (type-II) of superconductors, which can be penetrated by magnetic flux, even though the material has not fully returned to the normal (non-superconducting) state. The differences between the two types of superconductors are discussed in the next section.

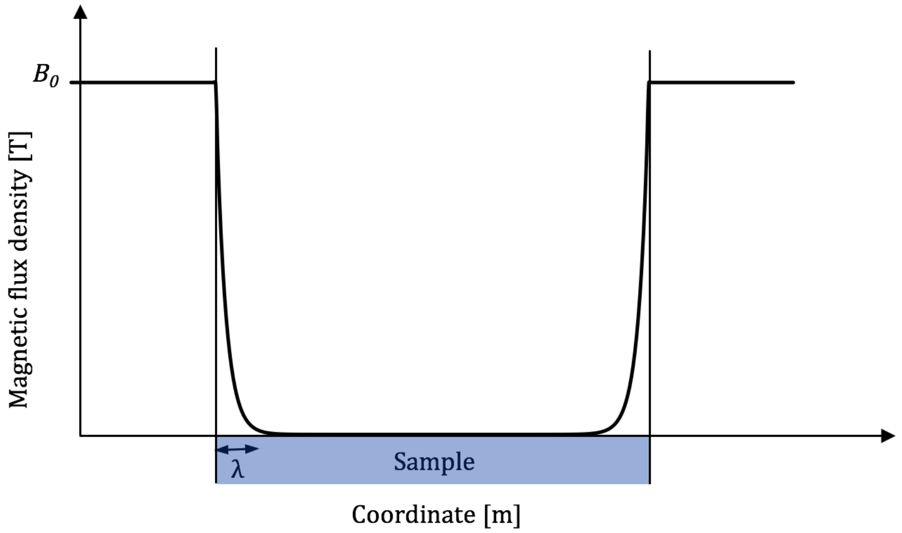

Figure 1.3– Exponential decay of magnetic flux density in a superconducting sample, characteristic width λ.

1.2.1 Distinction between type I and type II superconductors

Type-I superconductors maintain zero resistivity only if the magnetic field inside the superconductor does not exceed a critical value, H_c. If the field exceeds H_c, the superconductivity is abruptly destroyed by a first order phase transition.

However, type-II materials start to be penetrated by magnetic flux when magnetic field exceeds the lower critical field H_{c1}, while the bulk of the material remains superconducting. As the magnetic field is increased further, more and more of the magnetic flux penetrates the superconductor until the normal state is reached at the upper critical field H_{c2}. This effect is illustrated by a section of the magnetisation curves in Figure 1.4.

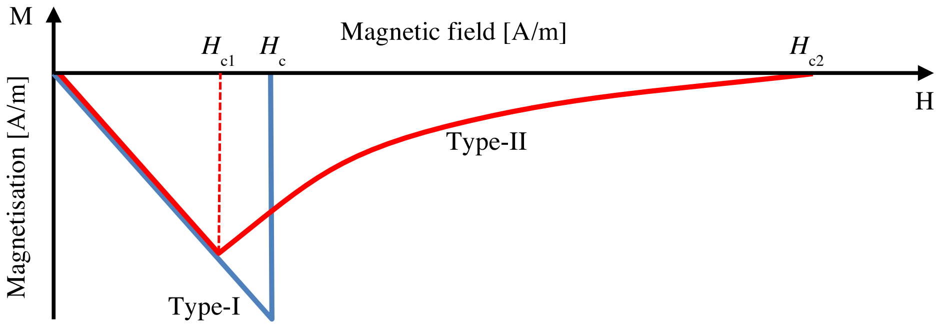

Figure 1.4– Part of magnetisation curve for type-I and type-II superconductors.

Most superconducting compounds are attributed to type-II superconductors, while most pure metallic superconductors exhibit properties of type-I superconductors (with the exception of Nb, V and Tc which are elemental type-II superconductors).

The critical flux density $\mu_0 H_c$ for type-I superconductors is less than 1 T even at temperatures near 0 K, hence they are of limited practical use. On the other hand, the upper critical fields for type-II superconductors can be much higher, enabling applications which require high magnetic fields.

1.2.2 Flux vortices in type II superconductors

At magnetic fields above H_{c1} the magnetic field starts to penetrate the type-II superconductors in discrete flux quanta, of:

$$\Phi_0 = \frac{h}{2e} \approx 2.07\times10^{-15}\ \mathrm{Wb} \tag{1.3}$$

Each fluxon is of a cylindrical shape with its axis parallel to the applied field. The radius of the fluxon is related to the coherence length ξ, a parameter introduced in the phenomenological Landau-Ginzburg theory [8]. The core of the fluxon is not superconducting, however the surrounding material is. Magnetic field within the superconductor must decay with a characteristic length of λ as shown in Figure 1.5a). This is achieved by a circulating current around each fluxon, shielding the superconducting material from the magnetic field (Figure 1.5b). In pure, defect free superconductors, due to mutual repulsion, the flux lines form a regular hexagonal lattice as first predicted by Abrikosov [9] from the solutions of Landau-Ginzburg equations for:

$$\kappa = \frac{\lambda}{\xi} > \frac{1}{\sqrt{2}} \tag{1.4}$$

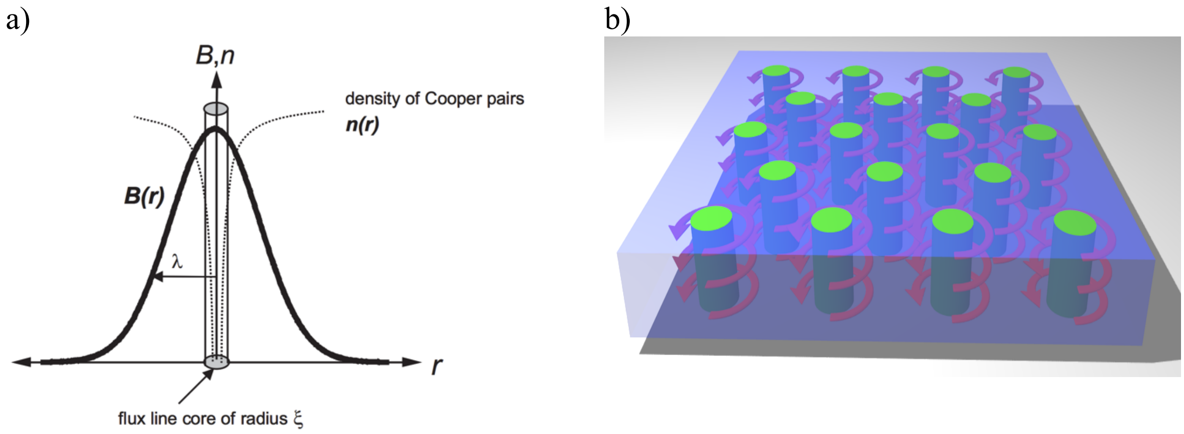

Figure 1.5– a) Schematic representation of an isolated flux line. The figure shows distributions of flux density $B(r)$, and density of Cooper pairs $n(r)$. The core of the flux line is non-superconducting and its radius is the coherence length ξ, while the magnetic field decays with a characteristic length λ (London penetration depth). Taken from [10]. b) Flux line lattice (green) in a type-II superconductor (blue), shielded by circulating currents (red). Additional shielding currents at the surface of the SC not shown.

This provides a distinction between type-II and type-I superconductors, i.e. for type-I $\kappa < 1/\sqrt{2}$ and for type-II $\kappa > 1/\sqrt{2}$. When a current is passed through the superconductor, the flux lines experience a Lorentz force per unit volume:

$$\mathbf{F}_\mathrm{L} = \mathbf{J} \times n\mathbf{\Phi_0} = \mathbf{J} \times \mathbf{B} \tag{1.5}$$

where n is the density of the flux lines. If the flux lines are able to move, the resulting change of magnetic flux produces electric field in the direction of current transport, thus leading to dissipation Q (see equations (1.6) and (1.7)), even though the material is not fully in the normal state.

$$\nabla \times \boldsymbol{E} = -\frac{d\boldsymbol{B}}{dt} \tag{1.6}$$

$$Q = \boldsymbol{E} \cdot \boldsymbol{J} \tag{1.7}$$

Due to the above, defect free crystals of superconductors cannot carry a current without dissipation above the lower critical field H_{c1}. Nevertheless, the flux lines can be pinned by the presence of defects in the crystal lattice or particles of non-superconducting phases (see section 1.2.4).

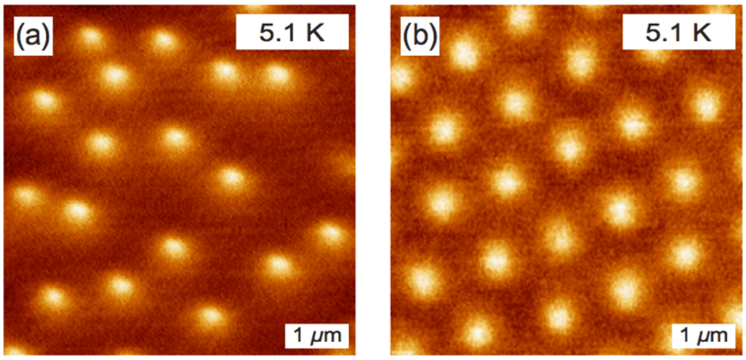

Figure 1.6– Magnetic force microscopy image of flux lines in a neutron irradiated sample with random arrangement of flux lines a) and a defect free $Bi_2Sr_2CaCu_2O_{8+\delta}$ showing a hexagonal arrangement b). Taken from [11].

This is illustrated by Figure 1.6, where it is shown that flux lines preferentially arrange themselves on pre-existing defects, to minimise free energy. Flux pinning is vital for lossless current transport at fields above H_{c1} and it is also the basis for Bean's critical state model, described in the following section. The pinned flux lines are termed to be in a vortex glass phase. Upon increasing the magnetic field further, a field is reached, where the pinning force $\mathbf{f}_p$ exceeds the Lorentz $\mathbf{F}_L$ (see equation (1.5)) and the SC no longer can support a lossless current. This field is called the irreversibility field H_{irr} and $H_{c1} < H_{irr} < H_{c2}$. At fields above H_{irr} the flux lines are free to move, transforming from vortex glass to vortex fluid, as shown in the schematic diagram in Figure 1.7. Therefore, for practical applications, H_{irr} and not H_{c2} is the limiting factor.

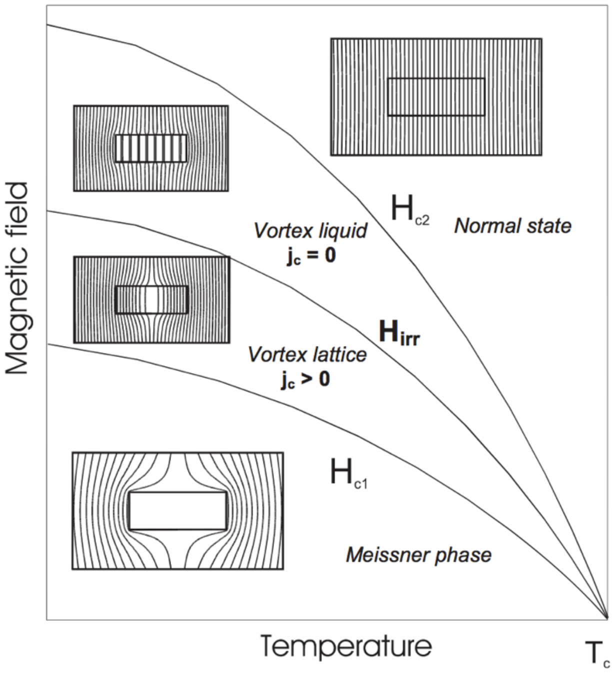

Figure 1.7– Schematic view of the magnetic phase diagram of type-II superconductors. From [10].

1.2.3 The critical state model

The critical state model, first introduced by Bean [12,13] describes the magnetic flux profile in type-II superconductors at fields above H_{c1}. As discussed in the previous section as the magnetic field increases and flux starts to penetrate the sample in the form of flux lines, they are acted upon by Lorentz force $\mathbf{F}_L$, and the flux lines redistribute themselves until the pining force $\mathbf{f}_p$ balances the Lorentz force. By combining Ampere's law (1.8) and equation (1.5) we arrive at (1.9):

$$\nabla\times\mathbf{B} = \mu_0\mathbf{J} \tag{1.8}$$

$$\mathbf{F}_\mathrm{L} = \mathbf{J}\times\mathbf{B} = \frac{1}{\mu_0}(\nabla\times\mathbf{B})\times\mathbf{B} = \mathbf{f}_\mathrm{p} \tag{1.9}$$

For instance, if the current is in the y direction and the applied induction is along z it follows that:

$$\frac{\partial B_z}{\partial x} = -\mu_0 J_y \tag{1.10}$$

hence

$$f_p = J_y B = -\frac{1}{\mu_0}\frac{\partial B_z}{\partial x}B \tag{1.11}$$

For a given pinning force f_p, the maximum lossless current that can pass through the superconductor is called the critical current density J_c. Therefore, the gradient of the magnetic field inside the SC has the value $\partial B_z/\partial x = -\mu_0 J_c$ within regions penetrated by the magnetic field and $\partial B_z/\partial x = 0$ for regions where there is no magnetic field (see Figure 1.8).

The Bean model neglects the $J_c(B)$ dependence on the magnetic field, however refined critical state models were later suggested, e.g. by Kim et al. [14] that incorporates $J_c(B)$ dependence in equation (1.10) and solves the resulting differential equation. The $J_c(B)$ dependence, that is consistent with experimental data for $J_c(B)$ values determined from magnetisation curves of V_3Ga cylinder was found to be:

$$J_c(B) = \frac{J_{c0}}{1 + \frac{B}{B_0}} \tag{1.12}$$

where J_{c0} and B_0 are constants. Many other relationships exist, also those that take into consideration the direction of the applied magnetic field, like the elliptical model to describe anisotropy of critical current with respect to magnetic field:

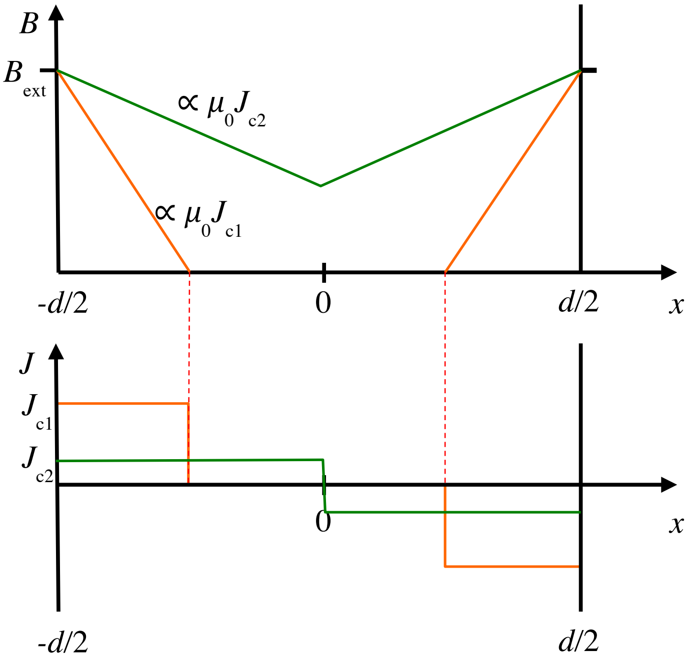

Figure 1.8– Magnetic field distribution inside an infinite superconducting slab of thickness d according to the Bean critical state model. B_{ext} is the external field. Higher pinning force leads to higher critical current density and higher field gradients.

$$J_c(B) = \frac{J_{c0}}{\left(1 + \frac{\sqrt{k^2 B_x^2 + B_y^2}}{B_0}\right)^{\beta}} \tag{1.13}$$

Or even more intricate functions for fitting experimental data for $J_c(B,T,\theta)$. Fitting functions are very useful when complete datasets over the whole range of interest are not available or actual transport measurements are difficult to perform, as is the case for bulk (RE)BCO [15]. However, with increasing commercialisation of (RE)BCO coated conductors, the availability of experimental $J_c(B,T,\theta)$ data is increasing, as the manufacturers see the need to characterise their products in wide range of conditions. In this case, direct interpolation of $J_c(B,T,\theta)$ data in numerical models is more accurate and easier to implement. Artificial pinning centres or inclined substrate deposition [16] can lead to very complicated $J_c(B,T,\theta)$ datasets, and fitting those requires great many fitting parameters, which in most cases do not have a clear physical meaning.

1.2.4 Flux pinning

Flux vortices in type-II superconductor (section 1.2.2) are acted upon by a Lorentz force when a current is passed through the sample, and the flux vortices must be prevented from moving to avoid energy dissipation. Crystal defects change material properties locally and can couple to the variation of order parameter (related to Cooper pair density, see Figure 1.5a) and local magnetic field. The former is usually the dominant mechanism. Crystal defects such as dislocations, point defects, voids, grain boundaries and precipitates can interact with the cores of flux lines by changes of material density, elasticity, electron-phonon coupling (δT_c pinning due to local changes in critical temperature) or electron mean free path length (δl pinning) [17]. The size of the defects is critical for effective pinning and they should be roughly the same size as the spatial variations of the order parameter, namely ξ, the coherence length.

The shape of the pinning centres affect the pinning at different angles of magnetic field. Point defects and spherical precipitates tend to increase the pinning and hence the critical current more or less isotropically (at any applied field direction), whilst, for example, elongated defects tend to preferentially enhance the pinning when the applied field is aligned with the defect (see Figure 1.9a). It is important to realise that in applications such as a magnet coil, it is the segment in the least favourable magnetic field orientation that limits the overall current, thus an isotropic improvement in critical current is often preferable. Whereas in a trapped field magnet made of HTS tape segments (section 1.4) each layer acts independently. Given that the field experienced by the superconductor is mainly along a single direction, columnar pining sites can be very effective. In (RE)BCO such defects can be made by self-assembled nanorods [18] (see Figure 1.9b), or irradiation by neutrons, protons or heavy ions [19]. (RE)BCO tape is particularly suitable for ion irradiation due to small thickness of the (RE)BCO layer, however this approach is not scalable, whereas tape with columnar nanorods is already commercialised. Nevertheless, making the distribution and morphology of these artificial pinning centres uniform in kilometre length scales is still a problem [20].

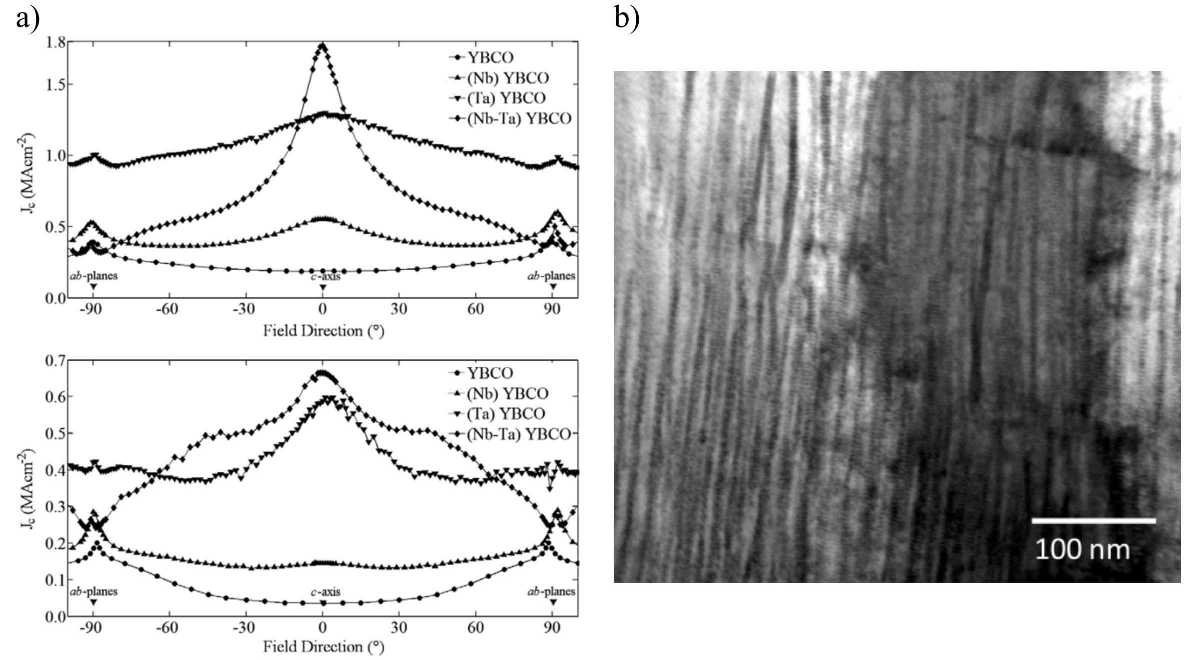

Figure 1.9– a) Improvement of critical current with additional doping (top – 1 T, bottom – 3 T applied field), forming precipitates aligned with crystallographic axes, note the increased critical current with field parallel to *c*-axis, taken from [18]; b) microstructure of a sample containing Barium Zirconium Oxide (BZO) nanorods as pinning centres, taken from [20].

1.3 Summary of technical (type-II) superconductors

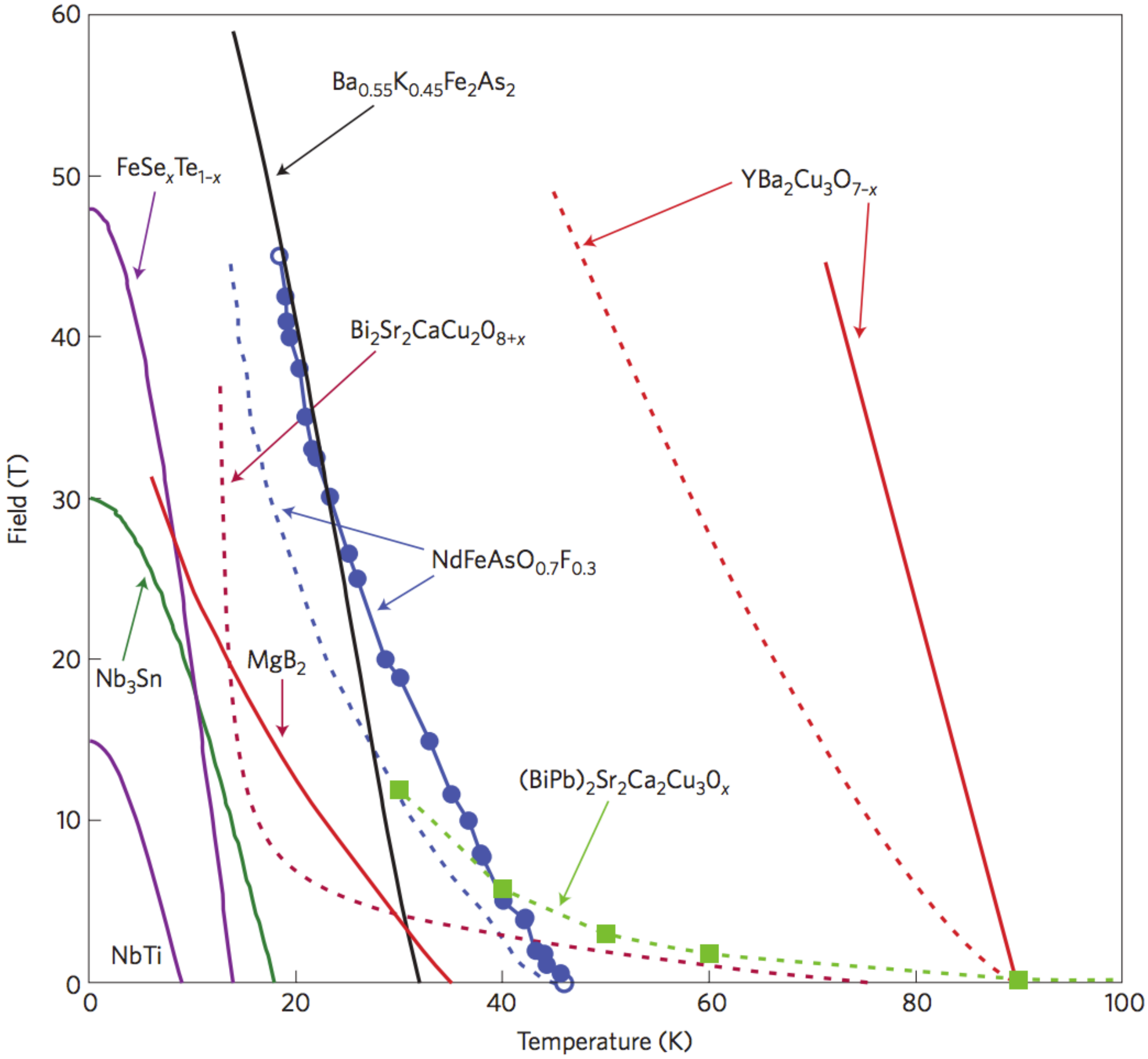

Figure 1.10– Comparative diagram of irreversibility and upper critical fields for selected superconductors. Solid lines show upper critical fields and the dashed lines show irreversibility fields. For LTS the irreversibility field is close to the upper critical field and not shown. From [21].

1.3.1 Nb_3Sn, NbTi

NbTi is an alloy of Nb and Ti, usually used as fibres in copper matrix and has a T_c of 9.2 K. The upper critical field is only 15 T, however its ease of manufacture and handling makes it a widely used superconductor for high field magnets, e.g. in magnetic resonance imaging (MRI) magnets and particle accelerators like the large hadron collider [22] (LHC). It was discovered to be superconductive in 1962 and it is still termed to be the workhorse of the superconducting magnet industry.

Nb_3Sn is more expensive than NbTi, however, the upper critical field is ~30 T, twice that of NbTi. Critical temperature is also higher at 18.3 K. Hence it is used in applications where extremely high fields are necessary, e.g. nuclear magnetic resonance (NRM) and fusion plasma confinement in the International Thermonuclear Experimental Reactor (ITER) [23]. Nb_3Sn is a brittle intermetallic compound, therefore the magnets must be wound before reacting the precursor materials. The most common manufacture methods include internal tin, bronze as well as the PiT (powder in tube) route [24].

The major drawback for these low temperature superconductors is that their operation temperature must be close to liquid helium temperatures, making their operation relatively expensive, moreover, for a given temperature their performance for trapped field applications (which this report is concerned about) is worse than that of (RE)BCO.

1.3.2 MgB_2

Magnesium diboride was discovered to be superconducting only in 2001 by Akimitsu et al. [25], even though the compound was already synthesized in 1953. MgB_2 has T_c of ~39 K, which is remarkably high for a binary compound. MgB_2 is attractive for multitude of reasons: the precursor materials are relatively cheap and widely available, it is much more isotropic than (RE)BCO and BSCCO with a longer coherence length eliminating the need for textured material. This also allows for a variety of different fabrication methods and sample geometries. Wires can be made via PiT (as first demonstrated by Glowacki et al. [26]) or Mg diffusion route, and bulk samples with arbitrary geometries can be made using Mg liquid infiltration [27]. Relatively high transition temperature means that MgB_2 can be cooled by liquid hydrogen (20.3 K) or modern cryocoolers as opposed to liquid helium, the price of which is rising every year [28]. Irreversibility field and critical current density data of MgB_2 collected from various researchers is shown in Figure 1.11.

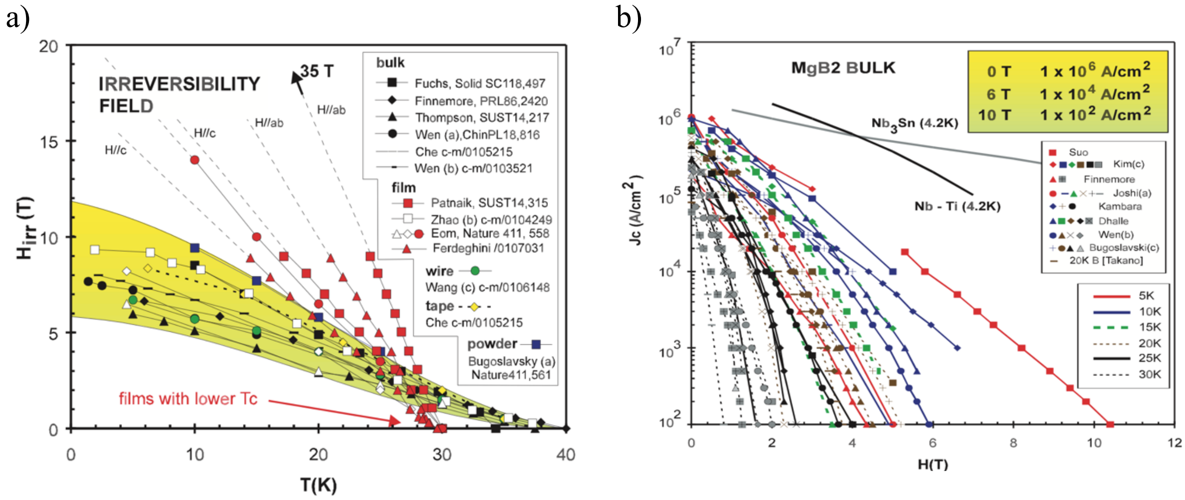

Figure 1.11– Irreversibility field of MgB_2 a) and critical current density for bulk samples b) at different temperatures. Taken from [29].

The ability to easily fabricate bulk samples, makes MgB_2 a candidate for trapped flux applications. However, as of yet, the trapped fields do not exceed 4 T for field cooling magnetization due to relatively low irreversibility field of bulk samples compared to (RE)BCO. The performance is even lower for pulse field magnetization due to low thermal capacity at operating temperatures and low temperature margin below the critical temperature, as shown by experiments and computer modelling by Fujishiro et al. [30]. A more comprehensive review of MgB_2 properties and fabrication methods can be found in a review article by Buzea et al. [29].

1.3.3 BSCCO

BSCCO is class of cuprate superconducting compounds with a general formula $Bi_2Sr_2Ca_{n-1}Cu_nO2_{n+4+x}$. The transition temperature increases with *n*, but the most common compound is $n = 2$ referred to as Bi2212 with T_c up to 93 K [17]. $n = 3$ is also common, known as Bi-2223 with T_c of approximately 108 K. Both T_c and the irreversibility line are strongly dependent on the oxygen content as in the case of (RE)BCO (section 1.3.4). Also, similarly to (RE)BCO, the coherence length for BSCCO is small (on the order of 1.6 nm in the ab plane at 0 K), therefore, there must be texture (grain alignment) to allow the passage of supercurrents. However, unlike in YBCO, BSCCO allows for texturing by deformation and subsequent melt processing, due to mechanically weak Bi-O layers in the crystal structure and comparatively low melting temperature (lower than Ag). For this reason, BSCCO was the first HTS material to be commercialized as multifilamentary wires, made by powder in tube (PiT) process [31]. Although the critical temperature is high, BSCCO is rarely used at temperatures above the 77 K as the irreversibility line (Figure 1.9) is relatively low due to decoupling of flux lines in to so called flux pancakes that are confined to CuO_2 planes and only weakly coupled across the CuO_2 planes via Josephson effects [32], see Figure 1.12b. For this reason, BSCCO is now is being superseded by 2nd generation (RE)BCO coated conductors, that show much better performance at higher temperatures and magnetic fields.

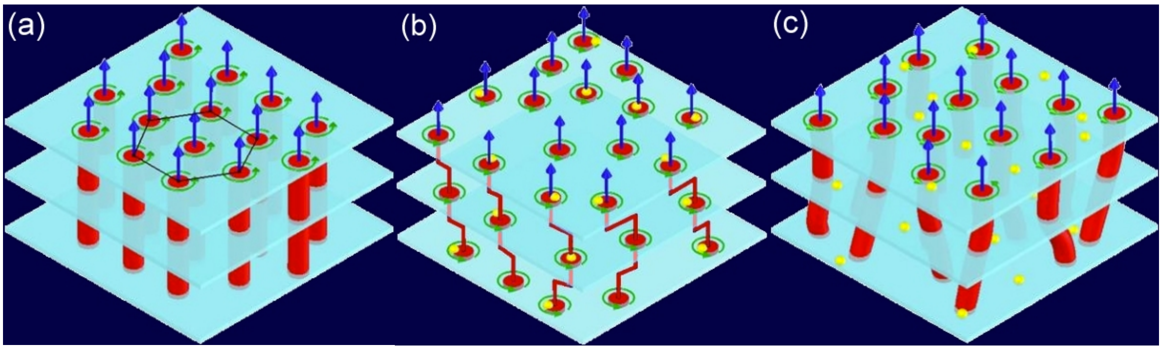

Figure 1.12– Different pinning scenarios. a) negligible pinning – vortices form hexagonal lattice. b) Strong pinning with large coherence length anisotropy – vortices separate into pancakes connected by Josephson vortices between layers. c) Strong pinning, small anisotropy – vortices form a disordered lattice as they bend to slightly to accommodate bulk pining sites. Taken from [33].

1.3.4 (RE)BCO

$(RE)Ba_2Cu_3O_{7-\delta}$, where (RE) denotes a rare-earth element, is a family of ceramic, perovskite related compounds that exhibit superconductivity at relatively high temperatures. The structure is also referred to as (RE)BCO or (RE)123. The most widely studied and produced compound of the family is $YBa_2Cu_3O_{7-\delta}$, depicted in Figure 1.13a). The properties of YBCO vary widely on the oxygen stoichiometry, with $\delta > 0.6$ showing semiconducting behaviour at low temperatures, and optimal superconducting properties are achieved at $\delta \approx 0.07$ (see Figure 1.13b).

Figure 1.13a also shows that the crystal structure is highly anisotropic, with most of the current transport associated with the Cu-O planes, hence the critical current in the crystallographic *a-b* plane is much higher than in the *c* direction. The anisotropy is also reflected in the coherence length, which is about 2 nm in the ab plane and 0.4 nm in the *c* direction at 0 K [10]. The ratio $\Gamma = \xi_{ab}/\xi_c$ is termed as the anisotropy parameter.

The magnitude of the coherence lengths is also comparatively small with respect to low temperature superconductors, which leads to a serious engineering challenge as the grain boundaries, which act as pining centres in LTS, now dramatically reduce the current carrying capacity. For useful engineering J_c to be retained, only low angle grain boundaries can be tolerated with missorientation being less than 4° [34]. For this reason, YBCO is usually textured either by top seeded melt growth method or deposition on a textured substrate (see section 1.5).

Even though there are many challenges associated with YBCO, it is now commercially made in the bulk and coated conductor form. It has a high T_c = 92 K, allowing it to be used at liquid nitrogen temperature (77 K), and the irreversibility line shows that the performance of YBCO rapidly gets better as the temperature is decreased further (Figure 1.10).

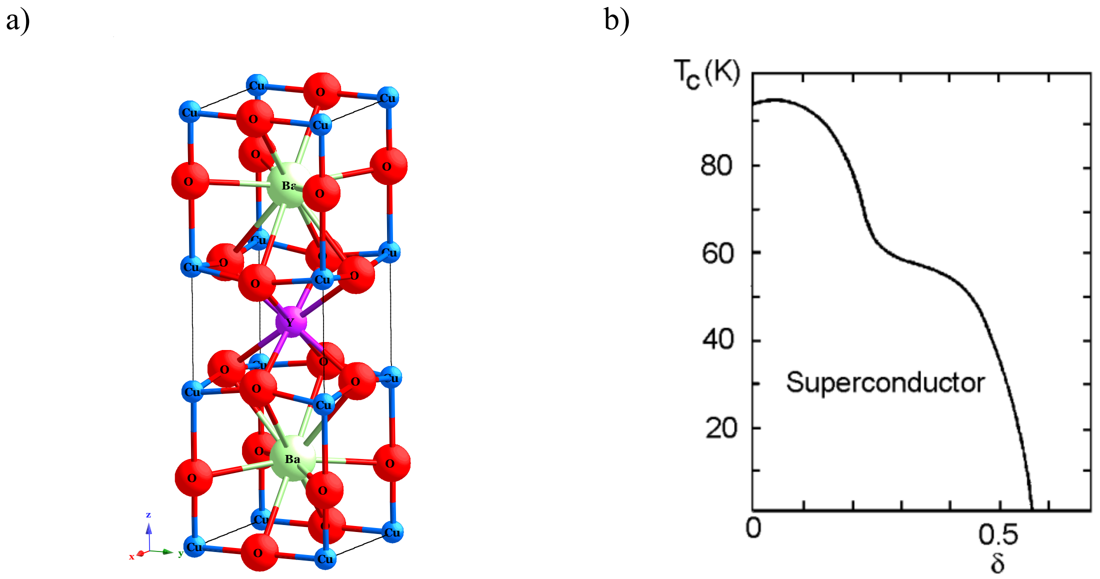

Figure 1.13– a) Orthorhombic unit cell of Y123 phase. Rendered using CrystalMaker software. b) Transition temperature of YBCO for different oxygen contents. The transition to superconductor is not seen for $y > 0.6$. Taken from [35].

1.4 Bulk superconductors as permanent magnets

In conventional ferromagnets, magnetisation is achieved by the cooperative alignment of atomic magnetic dipoles. Currently, the strongest ferromagnets are limited to remnant magnetic flux densities of about 1.5 T. As an alternative, superconducting bulks (Figure 1.14a) can act as compact sources of magnetic field by circulating a persistent, macroscopic current in the interior of the superconductor (Figure 1.14b) that produces a magnetic field above the superconductor. Fields of up to 10 times higher can be achieved in this manner, enabling higher power and torque densities in motors and generators. The differences in the nature of how the magnetic field is generated are evident in the vastly different magnetic field profiles above a permanent magnet and a superconductor as illustrated in Figure 1.15. Moreover, unlike for ferromagnets, the field above a trapped field magnet scales with its size. According to the Biot-Savart law and assuming the Bean model (no J_c dependence on magnetic field), the trapped field is given by [36]:

$$B_{trap} = \frac{\mu_0 J_c}{2}\left[(z+t)\ln\left(\frac{R+\sqrt{R^2+(z+t)^2}}{z+t}\right) - z\ln\left(\frac{R+\sqrt{R^2+z^2}}{z}\right)\right] \tag{1.14}$$

where z is the distance above the surface of the sample, R is the radius of the sample and t is its thickness. For the case when $t = R$ and $z = 0$, the above can be simplified as:

$$B_{trap} = A\mu_0 J_c R \tag{1.15}$$

where A is a constant and the trapped field is proportional to the sample size R.

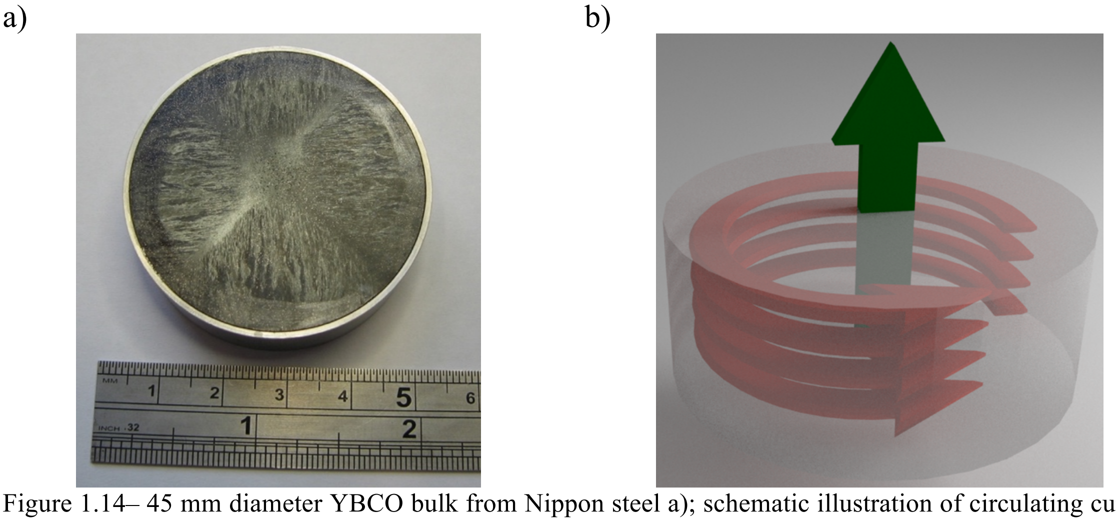

Figure 1.14– 45 mm diameter YBCO bulk from Nippon steel a); schematic illustration of circulating currents within a magnetized bulk superconductor (red) and resulting magnetic field (green) b).

There are several techniques to magnetise a bulk SC, which are discussed in section 1.5. The trapped field record to date is 17.6 T at 26 K between two 2.42 cm diameter (RE)BCO bulks [37] indicating huge potential of bulk (RE)BCO compact field sources in motors, generators and magnetic levitation applications.

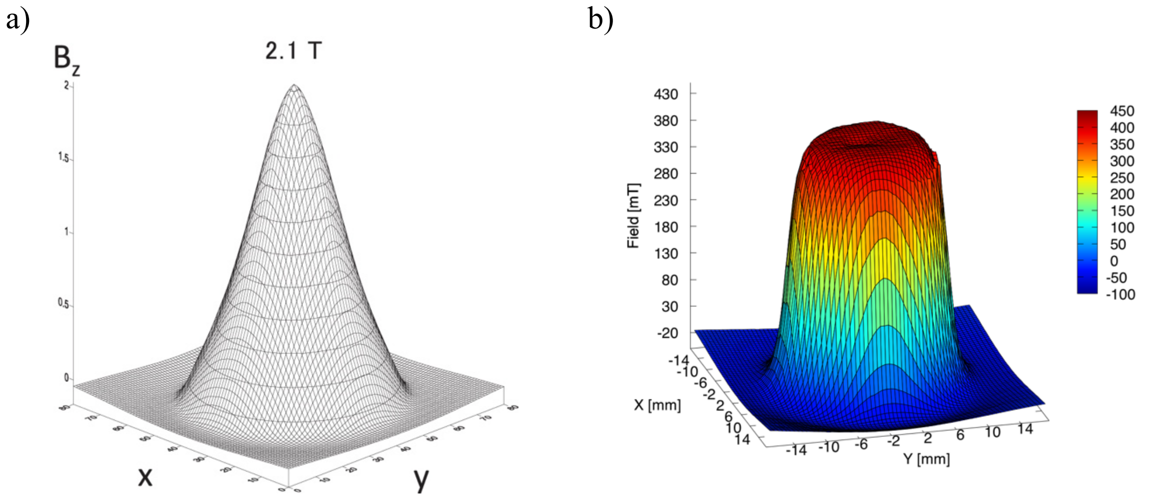

Figure 1.15– Magnetic flux density above a bulk superconductor with trapped magnetic flux [38] a); and a conventional permanent magnet b) showing a pyramidal and a flat-topped field profiles respectively.

1.4.1 Magnetisation

The magnetisation of a superconductor is defined as the total magnetic moment of the superconductor over its volume as:

$$\mathbf{M} = \frac{\mathbf{m_0}}{V} = \frac{1}{2V}\int_V (\mathbf{r}\times\mathbf{J})dV \tag{1.16}$$

The sample can be magnetized using an external magnetic field to induce currents within the sample. The induced currents create a magnetic field, termed as the trapped field. The trapped field profile depends on the shape of the SC, but for a cylindrical sample, the trapped field is conical as predicted by the Bean model described in section 1.2.3. Due to pinning, the magnetisation curve depicted in Figure 1.4 changes as the magnetisation is no longer reversible. Reversible M_{rev} and irreversible M_{irr} components of magnetisation in a type-II superconductor with strong pinning are shown in Figure 1.16.

As the magnetic field is increased past the lower critical field H_{c1}, the magnetisation keeps increasing with the same trend due to pinning until field H_{p} when the critical state is achieved and the critical current density flows across the sample. The magnitude of the magnetisation can no longer increase, but in fact decreases with increasing magnetic field due to critical current density, $J_c(B)$ dependence on magnetic field. Finally, at field H_{irr}, the irreversible magnetisation component goes to zero. As the field is ramped down, currents going in the opposite direction are induced until at $H = 0$, the sample is left with a conical trapped field profile with the maximum trapped field of H_p in the centre of the sample.

One of three methods are usually employed for magnetizing SC bulks, each of which will be discussed here in turn.

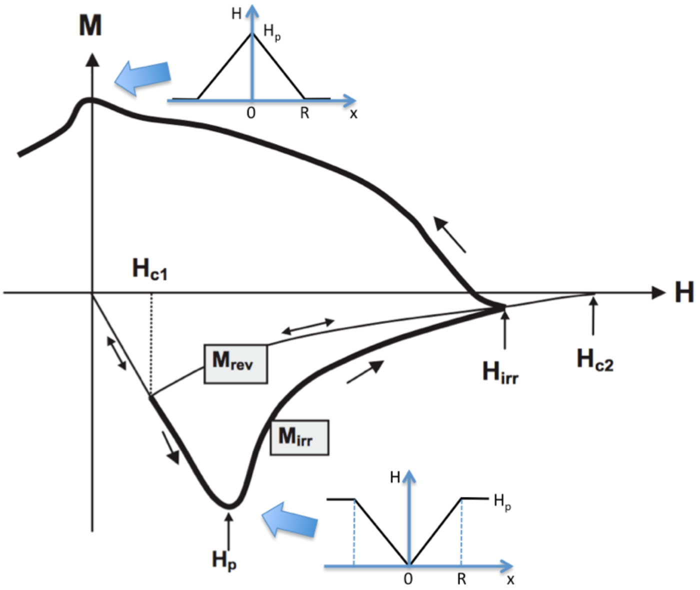

Figure 1.16– Magnetisation curve of type-II superconductor with strong pinning. Adapted from [10].

1.4.2 Field cooling

Field cooling (Figure 1.17b) involves applying an external flux density with the magnitude at least equal to the one intended to be trapped. The sample temperature is then lowered below the critical temperature to the operational temperature. The field is steadily reduced with a rate as slow as 0.1 T/min. A slow ramp-down rate is necessary to allow time to dissipate heat produced by movement of any de-pinned flux lines, that may cause flux avalanches. The main drawback of this technique is the requirement of sustained high magnetic fields, which call for superconducting magnets, making the magnetisation setup large and expensive. This also precludes the possibility of *in situ* magnetisation of bulks, e.g. inside the machinery requiring the SC bulks.

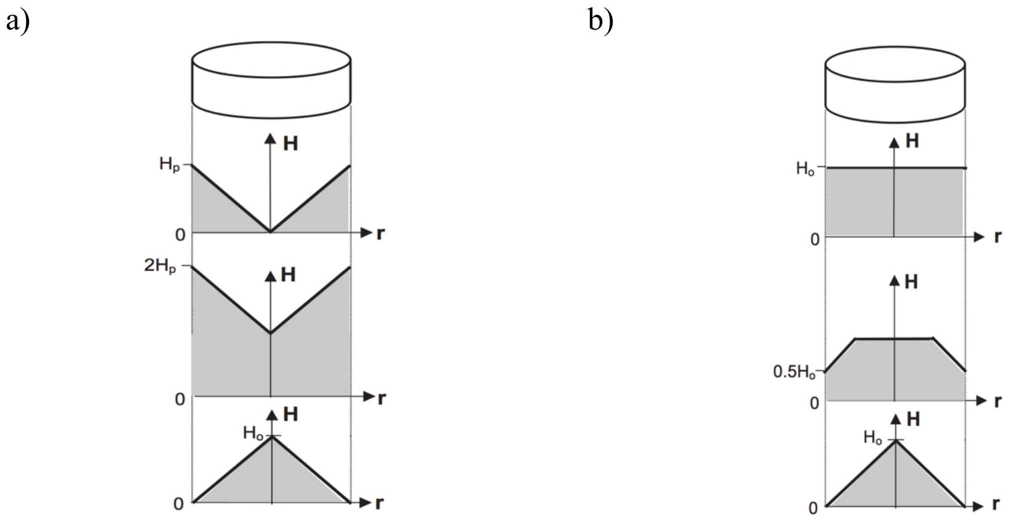

Figure 1.17– Comparison of magnetisation methods. a) zero-field cooling and b) field cooling. For zero-field cooling one needs to apply twice the expected trapped field (assuming constant J_c). The figures show the field profile across the centre (inside) the sample. Taken from [10].

1.4.3 Zero-field cooling

In contrast to field cooling, the sample is already in the superconducting state before the start of the magnetisation procedure. The applied field is ramped to twice the value needed to fully penetrate the bulk with magnetic field (see Figure 1.17a), as it is evident from the Bean model discussed in section 1.2.3. In order to avoid flux avalanches at high fields, the magnetic field ramp rates must be low as in the case of field cooling.

1.4.4 Pulse magnetisation

Pulse magnetisation is considered to be the most practical way to magnetise trapped field magnets [39] as the magnetising coils can be made of normal conducting materials. The basic principle is similar to zero-field cooling, however the time scale of magnetisation is on the order of 20 to 100 ms. The external field is applied in the form of a pulse to a sample that is already in the superconducting state. This way the magnetizing coil can be a compact copper coil, which only needs to survive a short pulse of very high current, provided by an external capacitor bank, as in the system described in section 2.4. This opens the possibility of *in situ* magnetisation, where the bulks on the rotor of a machine can be magnetised by e.g. the stator or separate normal state magnetisation coils.

A major drawback of this technique is the generation of heat during the pulse as the flux rapidly penetrates the sample, causing dissipation. The heat is generated quickly, within the timeframe of the pulse, causing the sample to heat up. The heat can't be conducted away quickly enough due to low thermal conductivity of YBCO. The rise in temperature lowers critical current density which leads to a reduction in the trapped field. Due to the positive feedback between the temperature rise and the energy dissipation rate, the sample may heat up sufficiently to become non-superconducting, causing a 'quench'. The problem of heat generation during pulse magnetisation can be mitigated in several ways, two of the most common being:

- use of several pulses instead of one (multi-pulse magnetisation),
- improving cooling power.

1.4.4.1 Multi-pulse magnetisation

Multi-pulse techniques can be employed to trap the field over a course of several pulses in order to add flux lost during the initial pulse due to excessive heating. Even though the time taken to magnetize each sample increases, these techniques are universally applicable and can be used for all types of bulks/stacks without adding much additional complexity to the system. Two most widely used techniques are IMRA and MPSC.

Iteratively Magnetizing pulsed field operation with Reducing Amplitudes (IMRA) first developed by Mizutani et al. [40], as the name suggests, employs several pulses at constant temperature. The first pulse is the largest and penetrates to the centre of the bulk. Some initially trapped flux is lost (especially in the periphery of the bulk) as the bulk heats up. The following pulses of decreasing amplitude are employed to return the lost flux. The reduced magnitude pulses no longer penetrate to the centre of the bulk, however they do not generate as much heat in the periphery of the bulk. The increase in trapped field compared to the single-pulse method is especially apparent at lower temperatures where the heat capacity of materials is very low, leading to large increases in temperature during PFM (Figure 1.18a).

Alternatively, Multi-Pulse technique with Sequential Cooling (MPSC) can be used. MPSC involves applying several pulses at constant temperature before cooling the bulk to a lower temperature and repeating the process. The resulting flux profile is rather flat (see Figure 1.18b) unlike the sharp cone profile produced by field cooling. A qualitative explanation in terms of the Bean model is given by Sander et al. [39].

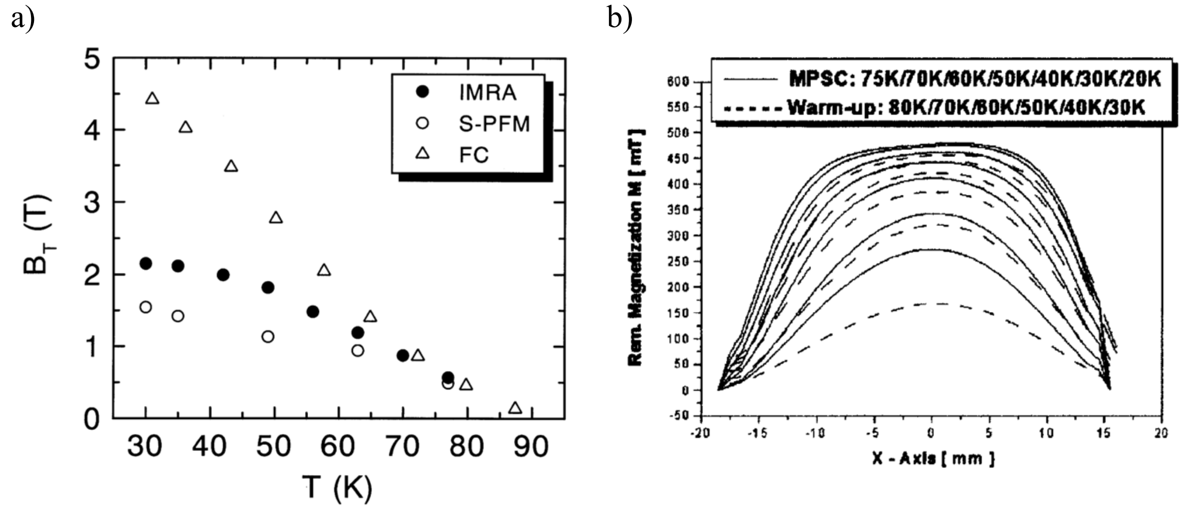

Figure 1.18– a) Temperature dependence of the maximum trapped flux density with the IMRA, single-pulse magnetization (S-PFM) and field cooling (FC) methods in a 34 mm diameter, 12 mm thick YBCO bulk. Reproduced from [40]. b) Remanent magnetization measured 4 mm above the centre of a 29.5 mm diameter 16 mm thick YBCO bulk after three 1.9 T/30 ms pulses at successively lower temperatures. The dashed line represents flux distribution as the bulk is being warmed up again. Reproduced from [39].

The best results are achieved when both MPSC and IMRA are combined. Fujishiro et al. [41] trapped a record 5.2 T (30 K, 0.5 mm above sample surface) in a 45 mm diameter, 15 mm thick $GdBa_2Cu_3O_{7-\delta}$ bulk by modified MPSC technique. However, this is still far below the maximum value that can be achieved by field cooling. This indicates some limitations of pulsed field magnetization as well as motivates to push this limit in order to make the gap between FC and PFM smaller.

1.4.4.2 Flux jumps during PFM

The Bean model predicts that the trapped field cannot be higher than half the applied field during zero-field cooling or pulsed-field magnetisation (see Figure 1.17). Usually it is significantly lower than half the applied field due to large temperature rise during pulse magnetisation (in particular at low temperatures). However, work reported in multiple research groups [41–43] has shown that so called flux jumps, rapid movement of flux lines into the interior of the sample during a fast rising edge of the applied field, can penetrate the sample with relatively small applied field magnitude. The large flux line redistribution (flux jump) happens as a small temperature perturbation due to heat release causes a decrease in critical current density in the sample. Due do decrease in critical current density, the current that is screening external magnetic field is reduced, allowing the movement of flux lines to the interior of the sample (due to the Lorentz force acting on the flux lines). This flux motion results in the electric field, which is accompanied by further release of heat and temperature increase. It is obvious that this can lead to an avalanche effect, i.e. a flux jump where magnetic field penetrates the sample. In case of most superconductors, the thermal diffusion time t_k is much larger than of the flux diffusion, t_m, which leads to rapid propagation of flux followed by adiabatic heating of the superconductor $t_m/t_k \ll 1$ [44] as there is not sufficient time to remove the evolved heat.

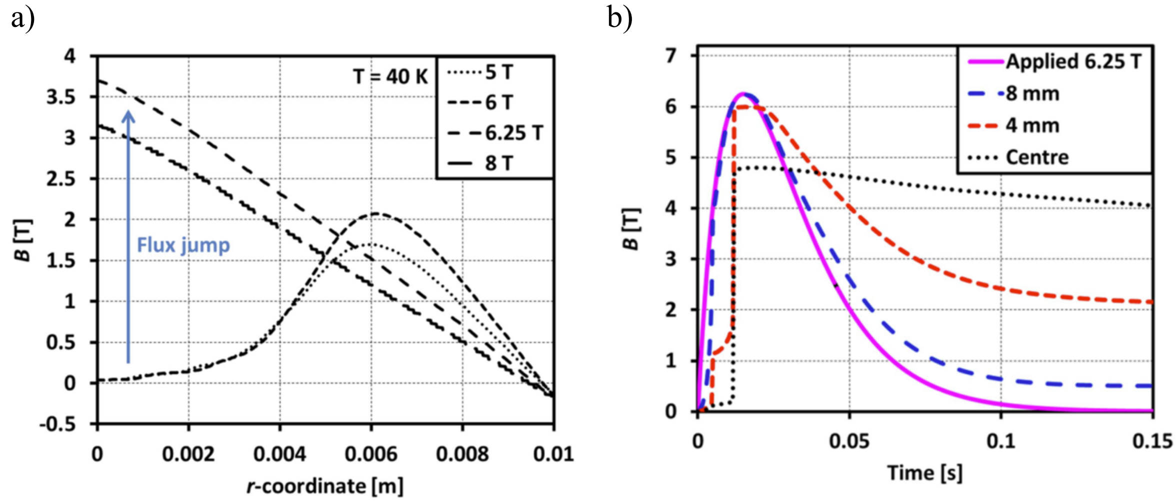

Figure 1.19– a) Numerical simulation results for trapped magnetic field profile across top surface (r – distance from the center of a cylindrical TFM) of the trapped field magnet for different applied fields at 40 K. Flux jumps observed after increasing the applied field from 6 to 6.25 T. b) Calculated trapped field at different locations on the sample surface against time for applied field of 6.25 T. Reproduced from [45].

A modelling study by Ainslie et al. [45], has shown evidence that very high Lorentz force acting on the flux lines is the reason for this behaviour. High critical current of the sample and high ramp rates dB_{ext}/dt increase the likelihood of a flux jump. The flux jump is usually triggered upon applying high enough pulsed field B_T. Below this field, the central region of the sample has no induced currents, and the resulting field profile above the sample resembles the letter M. Above the field B_T, the flux enters the central region of the sample as well giving the usual cone shaped magnetic field profile. In most experimental setups, the pulse duration is fixed, hence the dB_{ext}/dt and B_T are directly linked. Flux jumps may also occur during the magnetic field ramp-down, as shown in section 4.5. However, it is often the case that in pulse magnetisation systems the ramp-up is much shorter e.g. 35 ms than the ramp-down ~500 ms, like in [43]. Even though very high trapped field (up to 5 T [41]) can be achieved, the rapid flux motion does heat up the sample, by as much as 20 K or more, limiting the attainable trapped field.

Utilising this behaviour when magnetising trapped field magnets in-situ would allow to reach higher trapped fields without the need to apply very high pulsed fields, making the technology more feasible.

1.4.5 Relaxation of trapped flux density

After a magnetisation procedure, the trapped field within a sample starts to decay even if a stable temperature is maintained and no external magnetic field is applied. This is referred to as “flux creep”. This effect is relatively well understood and does not pose significant technological difficulties for incorporating trapped field magnets into most applications. The decay is logarithmic with time, hence the absolute decay rate gets progressively smaller after a short while subsequent to the magnetisation procedure.

However, the decay of magnetisation in the presence of an AC magnetic field is less well studied. In particular, trapped field magnets in motors may experience an oscillating magnetic field perpendicular to the magnetisation direction (crossed-field). This was observed to cause significant demagnetisation rates. Both flux creep and crossed field demagnetisation are considered in the following subsections.

1.4.5.1 Flux creep

As discussed in the previous section, in order for the SC to carry a lossless current, the flux lines inside the SC must be pinned. However, at temperatures $T > 0$ K, there is a finite probability that the flux lines will overcome the potential barrier, U_p, of the pinning site. The resulting thermally activated flux motion is called flux creep. It is particularly important for high temperature superconductors, because at their operating temperatures, the thermal energy can be similar to the pining energy barrier $U_p/kT \approx 2$ as determined for YBCO single crystals [46] whereas for typical low temperature superconductors $U_p/kT \approx 100$. The collective flux creep theory, proposed by Feigel'Man et al. [47], takes into account the elastic properties of the flux line lattice and assumes weak random pinning, giving the time dependence of the persistent current as:

$$J(t,T) = \frac{J_{co}}{[1 + (\mu kT/U_0)\ln{(t/t_0)}]^{1/\mu}} \tag{1.17}$$

where J_{c0} is the current density at 0 K with no flux creep and $J \ll J_{c0}$. The parameter μ (not to be confused with permeability) is field and temperature dependant. Predicted values are:

- $\mu = 1/7$ at low fields and temperatures for creep of individual flux lines
- $\mu = 3/2$ at higher fields and temperatures for collective creep of small flux bundles
- $\mu = 7/2$ at even higher fields and temperatures for collective creep of large flux bundles

By setting $\mu = -1$, we get the creep dependence for low temperature superconductors in Kim-Anderson model (i.e. simple logarithmic decay).

According to the collective flux creep model the normalized creep rate is given by:

$$S = \frac{1}{M}\frac{dM}{dln(t)} = \frac{kT}{U_0 + \mu kTlnt/t_0} \tag{1.18}$$

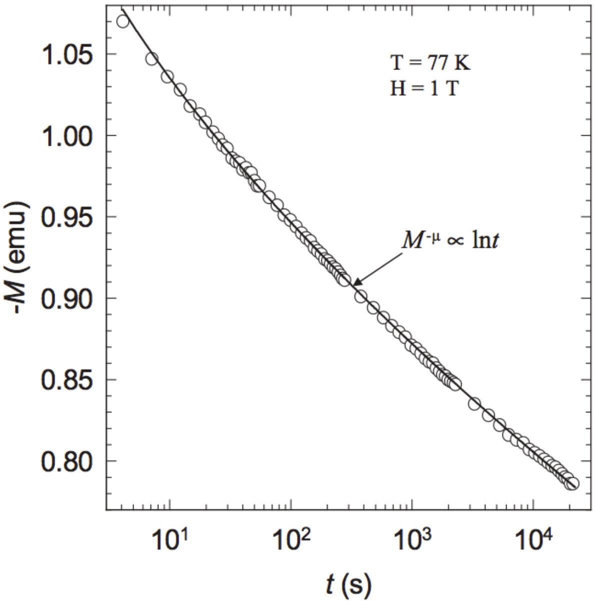

Figure 1.20– Time dependence of magnetization for a bulk YBCO sample. The fit shows that $\mu \approx 0.8$ indicating collective creep of large flux bundles. Taken from [10].

A typical magnetisation decay curve for an YBCO sample at 77 K and 1 T is shown in Figure 1.20. The estimated magnetisation decay rate is 8% per time decade. This relaxation can be a significant problem in applications requiring steady, time invariant magnetic fields.

The relaxation rate can be reduced by introducing stronger pinning centres. Columnar defects, perpendicular to the current direction (i.e. parallel to the flux lines) were shown to be particularly effective pining centres. They can be introduced by high energy heavy ion, proton or neutron irradiation [19]. It was shown to increase both the critical current and significantly reduce the creep rate as shown in Figure 1.21a.

Another, simpler alternative is to make the induced currents sub-critical. This can be achieved by lowering the temperature of the sample after the critical state was achieved. Figure 1.21b shows the magnetisation decay of samples magnetised at 77 and 65 K. The relaxation is drastically reduced after the sample temperature was reduced from 77 to 65 K.

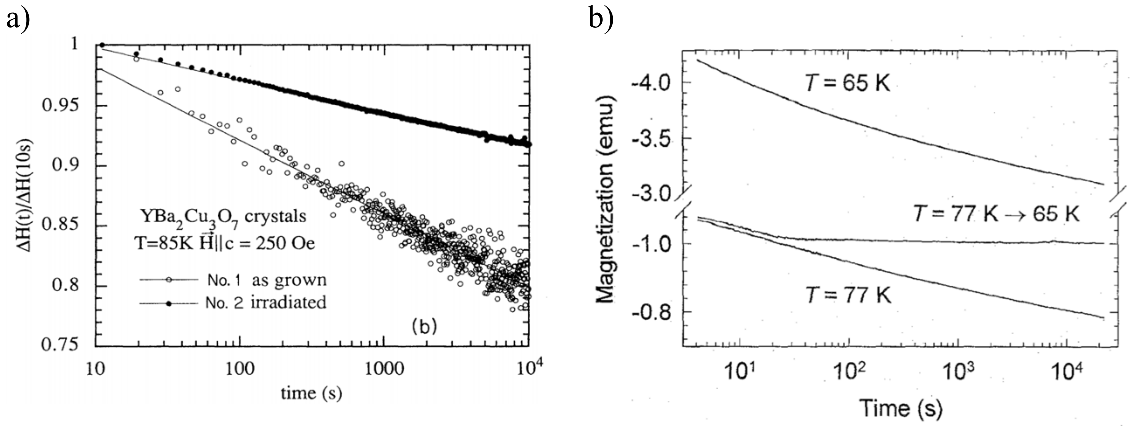

Figure 1.21– a) Magnetic relaxation of bulk YBCO sample at 85 K, before and after irradiation by 5.3 GeV Pb ions, taken from [19]; b) magnetisation of a bulk YBCO sample vs. time at 65 and 77 K. The relaxation could be drastically reduced by cooling the sample from 77 K to 65 K after magnetisation. From [48].

1.4.5.2 Crossed-field demagnetisation

The crossed-field demagnetisation is not yet completely understood in the case of applied devices of finite geometry, as in the general case the magnetic field is not perpendicular to the current and electric field is not necessarily parallel to the current. Other effects such as force free configurations and flux cutting may also be relevant.

However, some progress in calculation of crossed-field scenario can be made by making some simplifications, as in the case of infinitely long strip, where the initial magnetisation current and the current induced by the crossed field are both along the axis of the strip. Samples in this configuration were both modelled in FEM and experimentally measured by Vanderbemden et al. [49]. By modelling the configuration as depicted in Figure 1.22, he successfully replicated the qualitative behaviour seen in the experiments, however, the actual demagnetisation rates measured were much lower than modelled.

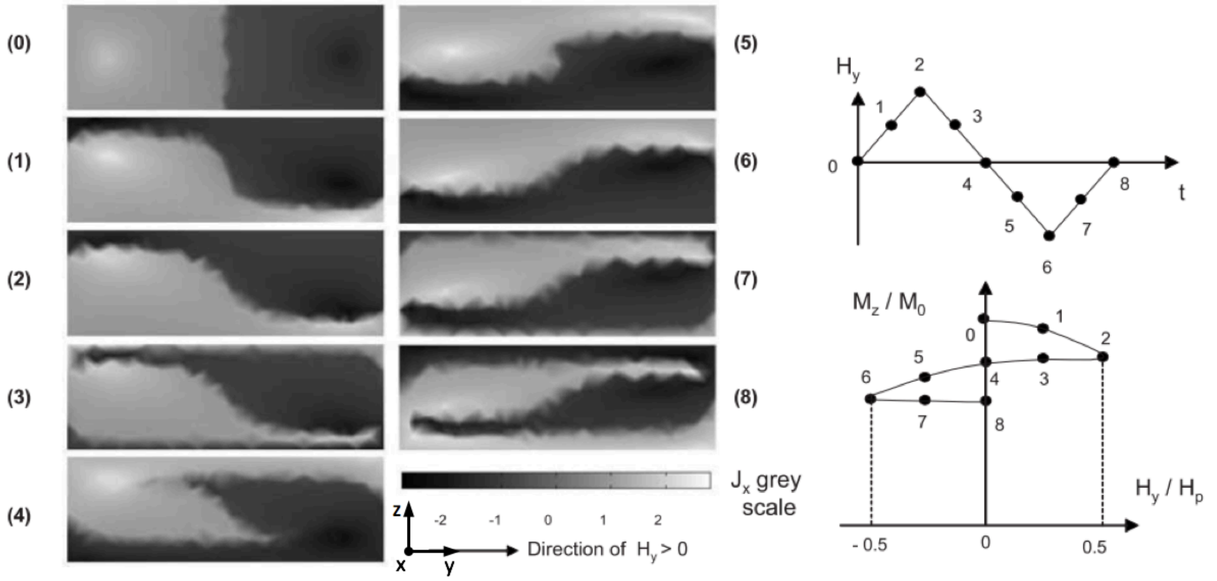

Figure 1.22– Modelled data of the current density distribution $J_x(y,z)$ within the cross section of the sample during one cycle of the transverse magnetic field of amplitude $0.5H_p$. A field-dependent $J_c(B)$ is assumed. Bottom: scale of current density J_x expressed in 10^3 A/cm^2. The arrow indicates the direction of a positive transverse field. Right: schematic diagram showing the times at which the current density distributions are determined. Taken from [49].

The reasons for discrepancy between the model and the measurement could be due to the end effects, where the current induced by the crossed-field must flow through the *c*-axis (*z* direction in the above figure) of the bulk, which has a critical current at least an order of magnitude smaller than along the *a-b* crystallographic plane [50] (*x-y* plane in Figure 1.22). Most importantly, the decay rate seems to follow a power-law dependence $B_z \sim N^{-\alpha}$ and does not saturate at a constant value at large *N* (number of cycles), however the decay rate does slow down with time.

More recent measurements on stacks of HTS tape by Baghdadi et al. [51] show significantly lower demagnetisation rate than previously reported for bulk (RE)BCO, which is an advantage for applications where a perpendicular AC magnetic field is expected, such as motors. Further work by Campbell et al. [52] show that the magnetisation decay constant falls almost linearly with the amount of tapes in the stack, but the models fail to explain the rapid decay during first few cycles. However, the experimental setups differ significantly from the modelled geometry. In particular, there are difficulties in modelling the extreme aspect ratio of the actual tapes > 10,000 while maintaining manageable computation times. Also, infinitely long tapes have to be assumed, whist those measured are usually close to being square. Importantly, the FEM models don't show saturation of magnetisation to a constant value after many cycles, even when the applied crossed field is much smaller than penetration field, which was a feature of the theory by Brandt et al. [53] for a single long strip and based on the Bean model. More experimental data is lacking, especially in the exact conditions experienced in a motor, i.e. high frequency of the AC field and temperatures below 77 K.

1.5 (RE)BCO coated conductor and comparison to bulk (RE)BCO

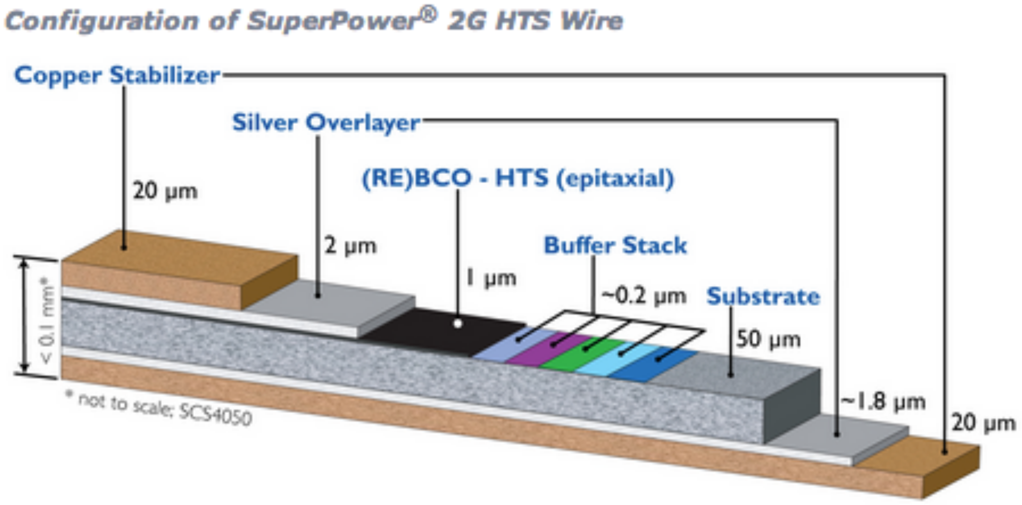

Figure 1.23– Architecture of 2nd generation HTS conductor manufactured by SuperPower. Notice the active material contributes to only ~1-2% of the volume. Taken from [54].

Commercially available (RE)BCO is mainly manufactured either as bulk (see Figure 1.14a) or as a thin film on a metallic substrate (also known as 2nd generation (2G) HTS coated conductor). The architecture of a 2G conductor, manufactured by one of the commercial companies (SuperPower) is shown in Figure 1.23. The two different form factors are favoured by different applications. Bulk (RE)BCO is mainly used in magnetic levitation applications and as potential compact sources of magnetic field for motors/generators, while the coated conductors are intended for current transport applications. However, the is no reason why the (RE)BCO tape cannot carry a persistent current within the plane of a superconductor. Hahn et al. [55] was the first to demonstrate a stack of superconducting annuli (see Figure 1.24) cut from a 40 mm wide tape trapping 2.3 T at 4.2 K.

Subsequently, Patel et al. have trapped 7.34 T at 4.2 K between two stacks made of 120 layers of 12x12 mm tape by field cooling [56] and up to 2 T at 10 K above a single stack with 145 layers using pulse magnetization [57]. As shown in Figure 1.24b, the pulsed field performance at low temperatures is significantly better than that of a commercial YBCO bulk of similar size, even though, the stack of tapes contains only ~2-6% volume of the superconducting material, vs. near 100% in an YBCO bulk. The critical current density of the tape used was ~200 A per cm width at 77 K and self-field, however (RE)BCO tape samples with I_c values exceeding 1000 A cm^{-1} have been reported [58]. This shows that the potential of stacks for trapping magnetic field is enormous.

Over the past years the number of companies manufacturing (RE)BCO coated conductors has increased, driving the costs down as well as improving performance [59]. The following sections provide a side-by-side comparison of bulk vs. stack of tapes for suitability as trapped field magnets. As the concept of stack of tapes is relatively new, the areas that need further investigation and can form the future research direction, will be outlined.

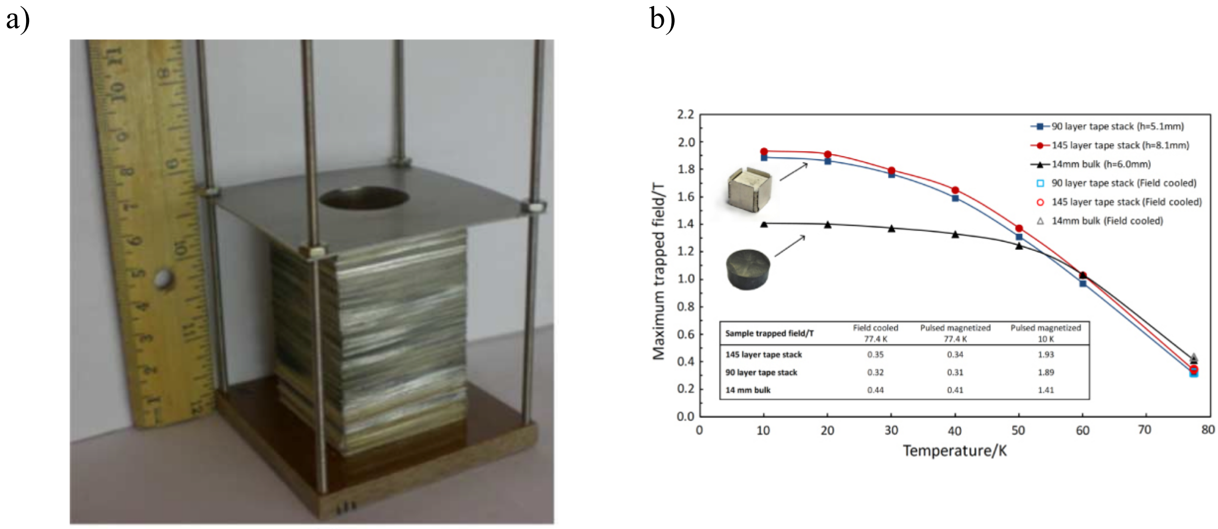

Sample trapped field/T	Field cooled 77.4 K	Pulsed magnetized 77.4 K	Pulsed magnetized 10 K
145 layer tape stack	0.35	0.34	1.93
90 layer tape stack	0.32	0.31	1.89
14 mm bulk	0.44	0.41	1.41

Figure 1.24– a) A stack of superconducting tapes for potential compact NMR magnets. Taken from [55], b) comparison of field trapped by PFM in similarly sized commercial bulk (RE)BCO and stacked HTS tape. Taken from [57].

1.5.1 Bulk manufacture

The conventional way of manufacturing bulk (RE)BCO is by top seeded melt growth [60] or top seeded infiltration and melt growth [61]. In either case the texture is introduced by a small

(RE)BCO seed with the rare-earth material chosen such that the peritectic temperature is higher than that of the (RE)BCO that is being grown. $SmBa_2Cu_3O_{7-\delta}$ or $NdBa_2Cu_3O_{7-\delta}$ are often chosen as the seed material for YBCO.

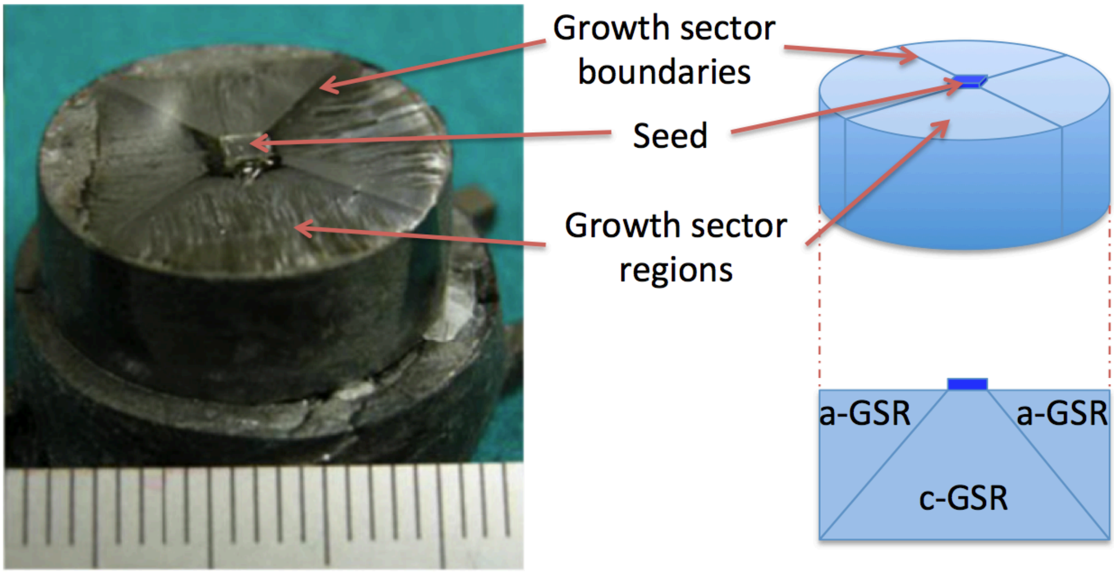

Figure 1.25– Picture of GdBCO (left, taken from [62]) with schematic picture of the growth sector boundaries (GSB) and growth sector regions (GSR). The four lines on the top of the bulk are the interfaces between <100> type growth sectors, bottom right figure shows GSB formed by <100> and <001> GSRs.

Due to the processing methods, (RE)BCO bulks inevitably have non-uniform superconducting properties. Figure 1.25 shows the growth sector regions and boundaries in an GdBCO sample. It is found that J_c is higher at the growth sector boundaries due to enhanced pinning, also the texture deteriorates going away from the seed. These inhomogeneities are detrimental in the trapped field performance, especially when pulse field magnetisation is used. It was shown [63,64] that localised heat is generated during pulse magnetisation at growth sector regions, where J_c is lower. This results is distortion of the trapped field profile, as well as an overall reduction in the trapped field. This also neglects other macroscopic defects within the bulks such as cracks and pores formed during the manufacture process [65].

The deterioration of the texture away from the seed also puts a limit for the size of the bulk as the material far away from the seed, does not contribute to the trapped field significantly. Nevertheless, bulks as large as 10-15 cm have been successfully fabricated [66]. There has been a lot of research into using multi-seeding of bulk (RE)BCO, however, the current transfer between domains grown by the two seeds remains poor due to low quality of the interface. In the case of bulk (RE)BCO, making larger samples does not necessarily lead to higher trapped fields (at low temperatures, see Figure 1.27) due to poor mechanical properties of the brittle material. Moreover, production of bulk (RE)BCO is a batch process, making it less efficient. Final manufacture step can take weeks as it involves diffusion of oxygen into large samples to attain the necessary oxygen stoichiometry for optimum superconducting properties.

1.5.2 Coated conductors manufacture

The structure of 2G (second generation) HTS conductor manufactured by SuperPower is shown in Figure 1.23. The substrate used is Hastelloy (a Ni based superalloy). After electro-polishing of the Hastelloy, a stack of buffer layers is deposited by ion beam assisted deposition (IBAD). The deposited buffer layers have a biaxial texture that acts as a template for growing (RE)BCO. Next, (RE)BCO is deposited epitaxially using metal organic vapour deposition (MOCVD) or pulsed laser deposition (PLD). The thickness of the superconducting layer is usually limited to several microns as the texture degrades with increasing thickness. A silver over-layer is deposited using sputtering to provide electrical contact, stabilisation and limited chemical protection. Optionally, an additional copper stabilisation layer can be deposited via electrodeposition. Several variations of the process exist, with each commercial company having a slightly different process. One such alternative method includes introducing texture directly by the substrate. Ni or Ni-W alloys are used for making Rolling Assisted Bi-axially Textured Substrate (RABiTS). The texture is introduced to the substrate by thermomechanical processing and it is transferred to (RE)BCO layer via intermediate buffer layers.

The thin film deposition techniques allow making of very good quality and uniform (RE)BCO coatings, that result in high J_c, with typical values in the range of 2-4×10^6 A/cm^2, in comparison to (RE)BCO bulks with a typical J_c of around 1×10^5 A/cm^2 at 77 K in self field. However, the comparison is not straight forward as for tapes the J_c is limited by the weakest segment in the tape tested, while in the bulks, the J_c is usually determined from a small sample cut from the bulk, even though in reality, overall J_c may be lower due to macroscopic inhomogeneities and defects described in the previous section. The important parameter for trapped flux applications is the engineering critical current density J_e, which takes into account the total volume of the conductor. And in the case of SC tape, the actual volume of the superconductor is only 1-6% of the conductor depending on substrate, silver and copper (if any) layer thicknesses. Thickness of the (RE)BCO layer is limited to several microns, and the substrate of at least ~20-30 µm is required. For this reason, the engineering critical current density of bulk (RE)BCO is still typically higher.

Contrary to bulk (RE)BCO, manufacture of tape can be a continuous (reel-to-reel) process, which is highly scalable. However, at the moment, one of the limiting factors for trapped field applications is the small tape width. Most manufacturers have standardised on 12 mm wide tape. The widest tape available commercially is 46 mm wide, the performance of which is not yet on par with narrower 12 mm wide tape. However multiple companies are developing process for 100 mm width tape for scale-up purposes, most notably STI [67]. On the other hand, the size of the stack is not limited in the length or thickness directions and the individual tape layers are flexible, allowing interesting geometries and trapped field profiles.

1.5.3 Mechanical properties

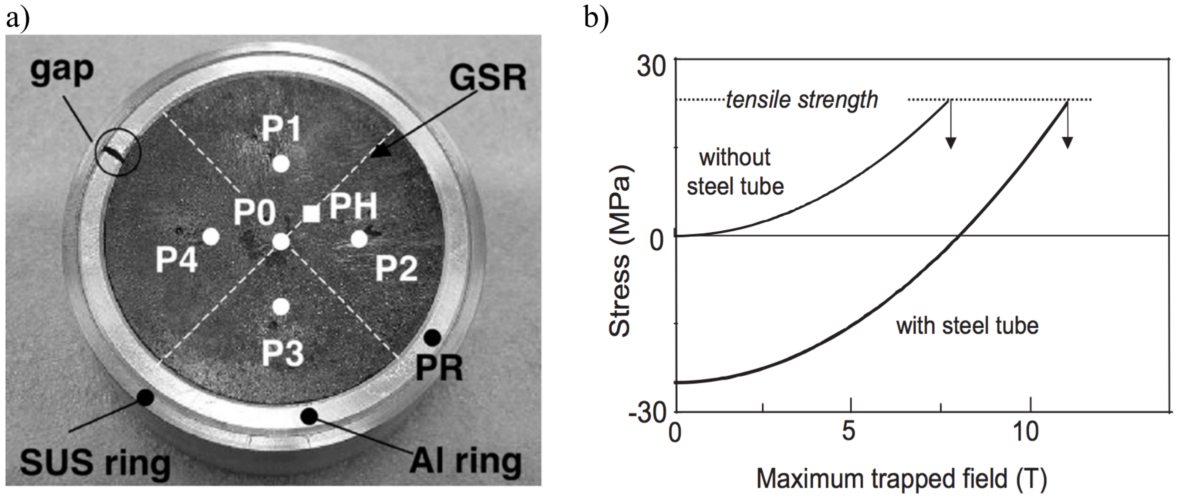

Figure 1.26– a) A SmBaCuO bulk fitted into stainless steel ring for reinforcement as well as Al ring to conduct away heat during pulse magnetisation, taken from [68]. b) Illustration of how compressive stress allows to reach higher trapped fields [10].

(RE)BCO bulk is a brittle ceramic with rather low fracture strength, in addition, the cracks and pores present within the sample lower the fracture strength by acting as stress concentration sites. Typical fracture toughness of an YBCO bulk is in the range of 1.4-2.2 MPa√m and the tensile strength can be as low as 25 MPa [10]. The poor mechanical properties become a problem at high trapped fields, when the magnetic tensile stress exceeds the tensile strength. The maximum tensile stress is at the centre of the sample and in the remanent state, it is given by [69]:

$$\sigma = 0.354\frac{B_0^2}{\mu_0} \tag{1.19}$$

In the above expression, the tensile stress σ is in Pa and the trapped flux density B_0 is in Tesla. Poisson ratio of 0.3 is assumed. From equation (1.19), we can determine that the trapped field is limited to ~9 T. The stresses experienced during magnetisation are even larger, especially if the external field used exceeds B_0, which is not know a priori. A simple way to counter the tensile stress is by introduction of compressive stress by a metal ring around the sample as shown in Figure 1.26a. It was found that impregnating the bulk YBCO with resin improved the tensile stress of a sample from 12 to 18 MPa. As the resin fills open cracks and voids in the sample, it increases the fracture toughness. Fracture stress was further increased to 29 MPa by wrapping the sample in carbon fibre and impregnating by epoxy resin [70]. The record 17.6 T field was achieved in sample pre-stressed and reinforced using a shrink-fit steel band [37].

Thermal cycling was also found to be a problem as the repetitive strain causes incremental growth of the cracks, lowering failure stress. Leender et al. [71] measured a decrease in fracture toughness by 20% as well as increase in crack density after 50 thermal cycles from room temperature to 77 K and back again.

On the other hand, the mechanical properties of HTS tape are largely dominated by the metallic substrate which contributes to up to 90% volume of the tape if no additional copper stabilisation

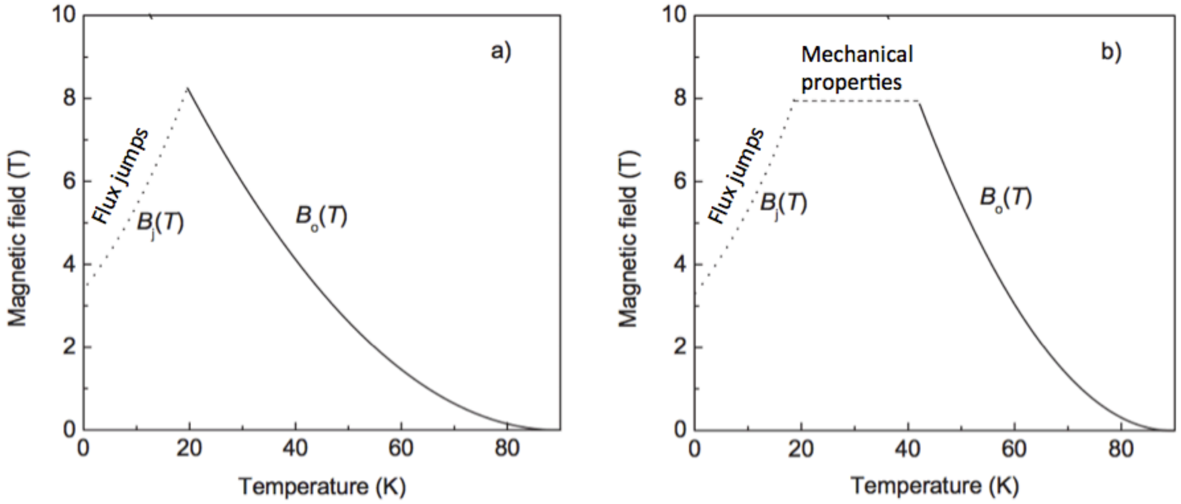

Figure 1.27– Limitations of maximum trapped field for bulk (RE)BCO at different temperature ranges and pinning strength. a) weak pinning: limitations due to $J_c(T, B)$, sample size and thermal instabilities at temperatures below 20 K, b) strong pinning: limitations due to $J_c(T, B)$, sample size at high temperatures, mechanical properties in range ~20-40 K and thermal instabilities below 20 K. Taken from [10].

is applied. The yield stress of Hastelloy C-276 is about 670 MPa at 77 K, which means that the tape can withstand about 90%, 0.9×670 = 603 MPa without mechanical degradation. Further data shows that the critical current is not affected almost right until the yield stress, even if the stress is cycled [72]. By using equation (1.19), we obtain the upper limit for trapped field (in terms of mechanical strength) as ~45 T, clearly indicating that mechanical strength is not the limiting factor for the tapes.

1.5.4 Thermal properties

As can be seen from Table 1.1, the thermal conductivity of YBCO is rather low compared to most metals. Low thermal conductivity is desirable in applications like current leads, however it can also lead to thermomagnetic instabilities - flux jumps at low temperatures, lowering the trapped field bellow the value expected from the critical current dependence on temperature. Figure 1.27 shows the limiting factors for maximum trapped field in bulk (RE)BCO. The flux jumps occur due to localised heating due to movement of individual flux lines, but the local temperature increase (if not conducted away) can cause flux avalanches that lower the overall trapped field.

On the other hand, in the SC tape, (RE)BCO is covered with a layer of high thermal conductivity silver and possibly copper that can quickly homogenize temperature stifling flux jumps. Moreover, the comparatively thick substrate layer acts as a heatsink. This is illustrated by Patel et al. [56] showing almost linear increase in trapped field down to 4 K (see Figure 1.28). Thermal properties are even more important for pulse magnetisation, as outlined in section 1.4.4.

Table 1.1 – Selected properties of Hastelloy C-276 substrate, silver over-layer and bulk YBCO at 10 – 77.4 K where there is a known temperature dependence. Data from [56].

Parameter	Hastelloy	Silver over-layer	Bulk YBCO
Density (kg m^{-3})	8890	10490	5900
Thermal conductivity (W m^{-1} K^{-1})	3-7.5	≈500-1500	6-20 ab-plane 1-4 c-axis
Heat capacity (J kg^{-1} K^{-1})	2-200	2-155	≈1-200
Tensile strength (MPa)	670-760 (yield)	≈60 (yield)	≈30 (fracture)

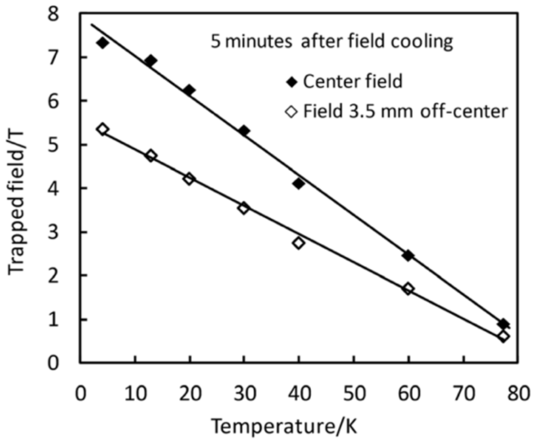

Figure 1.28– Trapped field between two 120-layer tape stacks using field cooling method at various temperatures. The increase in field as temperature decreases is approximately linear, reaching 7.34 T at 4.2 K. Taken from [56].

1.5.5 Trapped flux density

The trapped field is not only a function of material quality (the critical current density) and the geometric size of the sample as shown in equation (1.15), but mechanical properties, additional reinforcement, thermal management and the method of magnetisation. Therefore, magnetic fields trapped by different researchers is not always easily comparable. The following tables lists some of the highest fields attained for bulk (RE)BCO (Table 1.2) and (RE)BCO coated conductors (Table 1.3).

Table 1.2 – List of highest trapped field using field cooling and pulse magnetisation for **bulk** (RE)BCO.

Material	Magnetisation	Trapped field	Sample Size	Notes
Gd123	FC at 26 K	17.6 T between two disks	Two disks each 24.2 mm diameter and 15 mm thick	Stainless steel reinforcement [37].
Y123	FC at 29 K	17.24 T between two disks	Two disks each 26.5 mm diameter and 15 mm thick	Carbon fibre and resin reinforcement [69]
Gd123	PFM, 30 K	5.2 T at the surface of a bulk	Disk of 45 mm diameter and 15mm thick.	Stainless steel reinforcement [41].

In the case of bulk YBCO, the trapped field seems to be limited by the mechanical properties and flux jumps as described in the previous sections. It can be seen from Figure 1.29, that even though 17 T was achieved without fully saturating the bulk, the trapped field profile is not conical as predicted by the bean model. Hence, higher fields can be achieved by improving mechanical properties or providing adequate bracing post-fabrication. Further improvements of mechanical properties are difficult due to intrinsic brittleness of the ceramic (RE)BCO materials.

On the other hand, stacks of SC tape currently seem to be limited only by the size and engineering critical current density. The results by Patel et al., shown in Figure 1.28, can be extrapolated using equation (1.15) for larger width (going from 12 mm to 40 mm) and higher critical current densities (up to 1000 A/cm). Even though it is an extreme oversimplification, as the Bean model is assumed and J_c dependence on magnetic field is neglected, it suggests that trapped fields of over 20 T can be achieved.

Table 1.3 – List of highest trapped field using field cooling and pulse magnetisation for **tape** (RE)BCO.

Material	Magnetisation	Trapped field	Sample Size	Notes
Gd123	FC at 4.3 K	13.4 T between two stacks	Two stacks 12 mm square of 200 layers each (7 mm high)	See section 6.2
Gd123	FC at 4.2 K	7.9 T between two stacks	Two stacks 10 mm square of 130 layers each	[73]
Y123	FC at 4.2 K	7.34 T between two stacks	Two stacks 12 mm square of 120 layers each (6.9 mm high)	[56]
Gd123	PFM, 10 K	2.1 T at the surface of a stack	One stack 12 mm square of 200 layers each (7 mm high)	See section 6.3

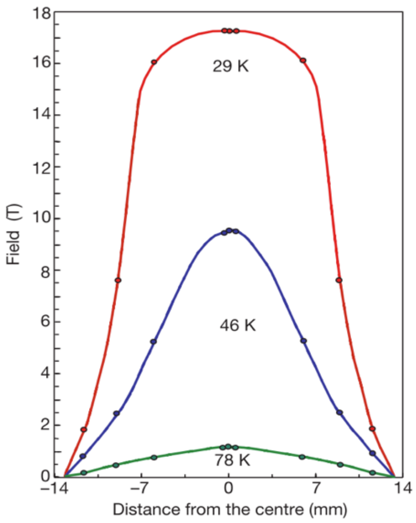

Figure 1.29– Profile of field trapped between two 26.5mm diameter YBCO disks. Sample is not saturated at 29 K, as the field profile is not conical as predicted by Bean model. Figure taken from [69].

1.6 Improvement of trapped field performance using composite structures

1.6.1 Improving thermal properties

The temperature rise during pulse magnetization could be reduced if the evolved heat is removed quickly or the thermal capacity of the material is increased. At the very least, the bulk could be cooled back down to equilibrium temperature faster to reduce the flux creep rate. However, due to the poor thermal properties of YBCO (thermal conductivity in *ab*-plane is 20 and along *c*-axis 4 W m^{-2} K^{-1} at 40 K [74]), increasing the cooling rate is not a trivial task. This can be achieved by using composite superconducting bulks that incorporate high thermal conductivity and high heat capacity materials. Metals are a good choice, however, eddy current heating during the magnetic pulse can pose a problem.

FEM modelling by Patel et al. [75] has shown that increasing the effective thermal conductivity of the YBCO can lead to significant improvements in trapped field (see Figure 1.30) in the case where the bulk is cooled from below, as in the most practical applications.

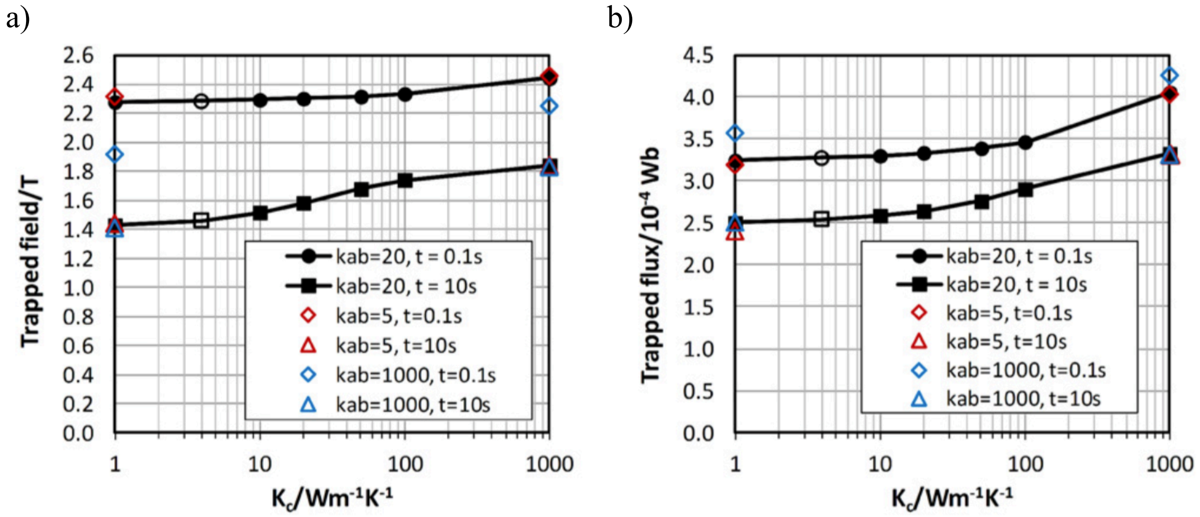

Figure 1.30– Modelling data showing that increase of thermal conductivity along crystallographic *c*-axis of YBCO can lead to significant improvements in trapped field a) and flux b). Black open symbols represent the actual values of thermal conductivity along *c*-axis. Trapped flux and field values given for 0.1 s and 10 s after pulsed field magnetisation. Taken from [75].

An increase in effective thermal conductivity can be achieved by incorporating high thermal conductivity structures (Figure 1.31a) directly inside the bulk. In my earlier work [76], copper wires were inserted into the bulk to effectively sink the heat generated during pulse magnetization into the laminated copper cold-head below. Filling the perforations with copper, resulted in a modest 1.6% increase in trapped flux (compared to a bulk and cold-head alone). Nevertheless, the performance is substantially increased when considering the trapped field after a single pulse. A 15% increase in trapped field was observed after the first pulse at 35 K (Figure 1.31b), which suggests that such composite samples can be fully magnetized faster and with a lower number of pulses. The increase in performance is expected to be higher if better thermal contact between the copper and YBCO could be achieved.

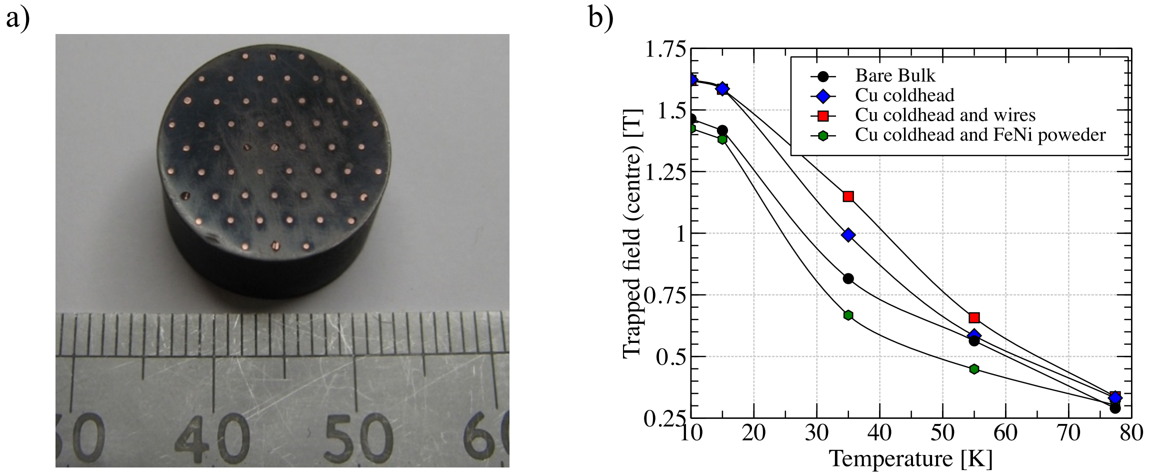

Figure 1.31– a) perforated YBCO bulk with copper wires filling the perforations to increase the effective thermal conductivity along the *c* crystallographic direction (along wires). b) Trapped field after the first pulse at each temperature of the modified MPSC sequence. From my earlier work [76].

1.6.2 Superconductor/ferromagnetic composite structures

In the previous sections, the importance of composite structures for thermal management during pulse magnetisation was discussed. There have also been several studies on bulk (RE)BCO/soft ferromagnetic composites [77,78] showing that the trapped field at the surface can be increased by the addition of soft ferromagnetic material when using field cooling magnetisation. Lousber et al. filled holes in a purposefully perforated YBCO bulk (Figure 1.33) with ferritic stainless steel (AISI 410) with saturation magnetisation of about 1.1 T and an initial permeability of 30. It was found that the maximum trapped field at the surface of the sample increased from 303 to 406 mT at 77 K, when the sample was magnetised by zero field cooling. Previously, I have carried out a similar study using an equivalent YBCO bulk and

Fe/Ni powder as the ferromagnetic material [79]. It was found that the magnetic material was actually detrimental to the trapped field using pulsed field magnetisation (see Figure 1.31b). This was attributed to rapid flux density increase within the material around the holes during the pulse, making the heating problem worse. Nevertheless, it was shown in a study by Patel et al. [57] that including ferromagnetic layers within a stack of SC tape, trapped field performance was slightly increased (Figure 1.32), however it is not clear in this case whether the magnetic properties or added thermal mass has led to the increase in trapped field.

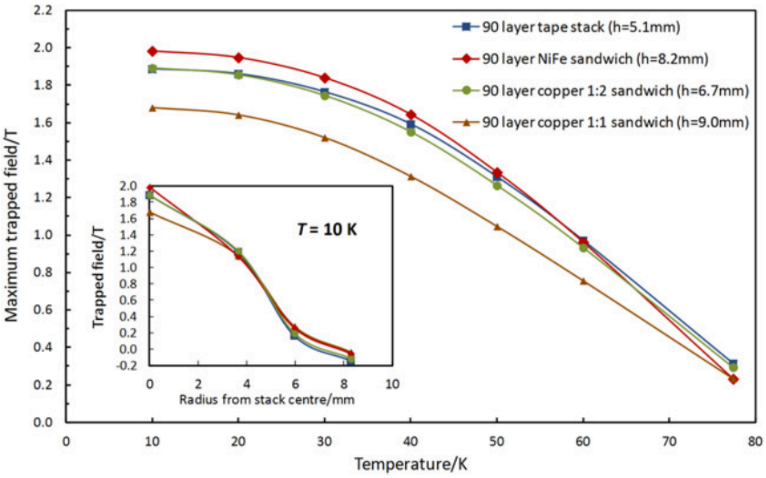

Figure 1.32– Peak trapped field measured 0.8 mm above tape sandwiches after pulse field magnetization with decreasing temperature. The NiFe sandwich had ferromagnetic NiFe layer whereas the copper sandwiches had a copper layer for every tape layer ('1:1') or every 2 tape layers ('1:2'). Taken from [57].

From the above we see that the effect of ferromagnetic additions depends on the geometry and the magnetisation method, and for pulse magnetisation, thermal effects play an important role. Computer simulations with further experimental work may clarify whether magnetic or thermal effects are dominant during PFM, and what are the optimum geometries and loading fractions of the ferromagnetic material for both PFM and field cooling.

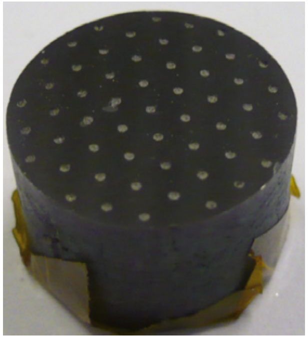

Figure 1.33– Perforated YBCO sample impregnated with ferromagnetic powder. From [77].

1.7 Applications using trapped field cryomagnets

Stacks of (RE)BCO tape target the same applications as bulk (RE)BCO trapped field magnets. The applications can be split into several large categories:

1. Motors and generators;
2. Trapped flux devices;
3. Levitation devices
4. MRI and NMR

The trapped field in stacks of (RE)BCO tape far exceeds what is possible by conventional ferromagnets and advantages listed in section 1.5 may give them an edge over bulk (RE)BCO. Most of the work published so far is concerned with optimisation of stacks for rotating machinery, however, the suitability (RE)BCO tape, and trapped field magnets in general, for other applications will be briefly discussed in the following subsections.

1.7.1 Motors and generators

The use of superconductors in motors and generators allow for:

- higher energy efficiency;
- higher torque and power density.

The efficiency of modern conventional electric motors is well above 90%, thus energy efficiency argument is only relevant only for large, MW scale machines to justify the increased complexity and costs. On the other hand, the reduced weight and size is very attractive for mobile applications. There are numerous successful superconducting prototypes in operation aimed at ship propulsion [80] and more recently, superconducting motors are being considered for next generation electric aircraft [81,82].

Superconducting generators are being considered for the next generation of high power wind turbines where substantial weight reduction would result in lower costs in terms of reduced installation costs (especially for off-shore wind generation) and potentially lower running costs as no maintenance intensive gearbox is necessary in many superconducting wind generator designs, like in the 10 MW power SeaTitan® from AMSC [83].

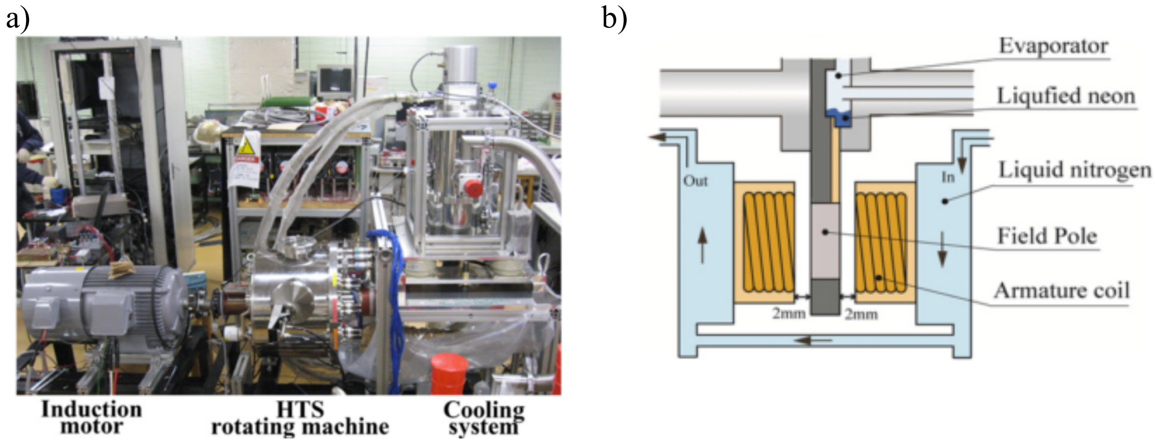

Figure 1.34– a) An overview of a prototype motor utilising (RE)BCO bulks as field poles on the rotor; b) schematic of the LN_2 cooled armature and magnetisation coils and liquid neon cooled (RE)BCO bulks acting as the field poles. Taken from [84].

(RE)BCO stacks of tape are mainly considered for permanent magnet AC synchronous motors, where the stacks replace the conventional permanent magnets on the rotor (Figure 1.34a). This way, much higher magnetic loading may be achieved, increasing the motor power, which is given by:

$$P \approx \left(\frac{\pi}{2}\right) BAD^2L\omega \tag{1.20}$$

Where B is the average magnetic loading, A - electric loading, D, L - rotor diameter and length and ω is the rotor angular speed. From equation (1.20) we see that the power scales linearly with the average magnetic loading. Superconducting motors are identified as the enabling technology that will allow power densities in excess of 10 kW/kg compared to conventional, normal conducting motors that are limited to 1-5 kW/kg.

(RE)BCO tape stacks address some of the problems of bulk (RE)BCO in motor designs, such as mechanical strength, uniformity of superconducting properties (section 1.5) and lower crossed field demagnetisation rate in service (see 1.4.5.2). Some of the major hurdles for prototype construction include rotor cooling and magnetisation (charging) of the trapped field magnets. Pulsed field magnetisation in the preferred option as it is most practical to implement (see 1.4.4). However, this start-up procedure must be performed each time the machine is warmed up. Other designs such as hysteresis or reluctance motors do not require a special start-up procedure, however they generally have a lower power density. A review of literature for motor prototypes utilising trapped field magnets was published by D. Zhou [85].

1.7.2 Trapped flux devices

The extremely high magnetic flux densities that can be achieved using trapped field magnets has resulted in a myriad of interesting applications, however none have yet been successfully commercialized due to the complexity of cooling and magnetizing ("charging") of these devices. Nevertheless, with the increase in availability of lightweight and efficient cryocoolers, these applications may just find their way into the market. These include devices such as superconducting dent pullers and magnetic workpiece clamps for manufacturing [17].

More recent research into magnetic drug delivery [86,87] shown how trapped field magnets can be used to guide and keep the drug at a specific site where it is needed. This increases the efficacy of the drug, while lowering its toxicity. The drug must be coupled to a magnetic particle, then the force on a particle with susceptibility χ (for small χ) and volume V_p is given by:

$$F_m = \chi V_p [B_0 \cdot \nabla B_0]/\mu_0 \tag{1.21}$$

where B_0 is the applied magnetic field. The force is proportional to both the field magnitude and its gradient. Unlike conventional ferromagnets, where the magnetic field produced is rather uniform over the surface of the magnet, in trapped field magnets, the field profile has a steep cone-like shape as shown in (Figure 1.15) and consequently has a high field gradient, without any additional field profile shaping. Moreover, it was demonstrated that the trapped field magnet can be made portable after magnetization, simplifying the procedure significantly [43,88].

Magnetic separation, which is based on the same principle as magnetic drug delivery is successfully used to separate ferromagnetic, paramagnetic or diamagnetic particles within a fluid. LTS, which can operate in a persistent mode, are commonly used to generate the magnetic field. The use of HTS wire/tape would increase the capital costs significantly for large scale systems, but would lower cooling/maintenance costs. Also, a number of small scale prototypes were constructed using trapped field magnets and seem to be ideally suited due to their compact size and modest cooling requirements [89,90].

In the opposite end from trapping flux, as type-II superconductors can effectively resist changes in field inside the material, they can be used for shielding a volume of space from external magnetic field. This is of importance for devices requiring extremely low background magnetic field such as SQUIDs (superconducting quantum interference devices). Superconducting materials, usually made in the form of a hollow cylinder can offer much better performance at low temperatures than high susceptibility ferromagnetic materials like mu-metal. Most HTS materials have been investigated, including (RE)BCO in bulk and tape form [91,92], and MgB_2 for low temperatures [93]. Fields inside such a shield can be many orders of magnitude lower than an externally applied field (see Figure 1.35).

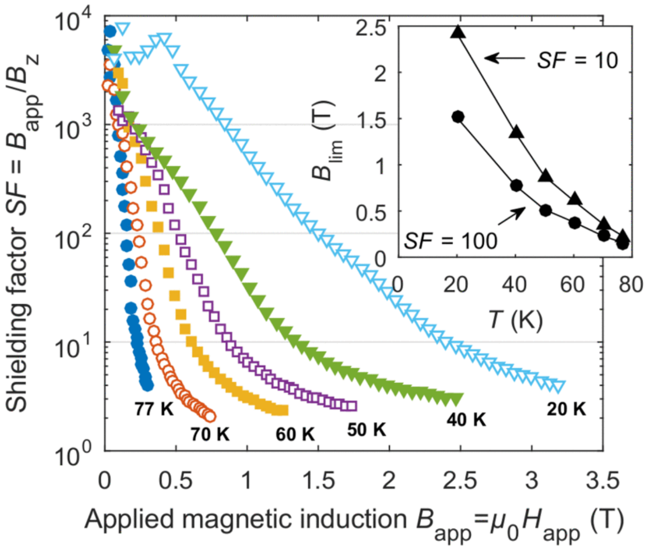

Figure 1.35– Shielding factor of an YBCO tube as a function of applied field for different temperatures. The data show that the measured field inside the magnetic shield up to 4 orders of magnitude lower than the applied field. Taken from [91].

1.7.3 Levitation devices

(RE)BCO bulk superconductors can be used for achieving stable levitation, which is otherwise impossible with any configuration of ferromagnets without additional active stabilization (see Earnshaw’s theorem [94]). The most commonly used configuration is a permanent ferromagnet levitated above a stationary superconductor. Keeping the superconductor stationary makes the cooling arrangement simpler. The stable levitation allows for low energy loss and wear-free rotation without the need for any lubrication. For such reasons, there is interest in using bulk (RE)BCO as high speed, non-contact magnetic bearings for flywheel energy storage (Figure 1.36) or high speed motor applications [95,96]. By using HTS bearings, the idling losses can be reduced from 1-5% of stored energy per hour (typical of mechanical and electromechanial bearings) to below 0.1% even when cooling power is considered [96]. The characteristic stiffness (change in force per unit of displacement) is relatively low, however, it makes the rotor dynamics more stable.

(RE)BCO bulks were also used to levitate people-carrying trains above permanent magnet tracks for prototypes in China, Brazil and Germany [97–99]. However, for large scale applications, a more scalable approach of pre-magnetized trapped field magnets moving above a conductive guideway is considered. Eddy currents induced in the guideway would provide the necessary lift. However, levitation is possible only once a sufficient speed is achieved, necessitating a mechanical support at start-up [100].

High levitation forces are also possible by replacing bulk (RE)BCO with (RE)BCO tape stacks, which has the advantage of many different geometries [101–103]. However, it is worth noting that unlike (RE)BCO bulks, tape stacks cannot sustain a persistent current in the direction between layers (thickness of the structure), therefore it is best suited for bearings where levitation force is only required in one translational degree of freedom.

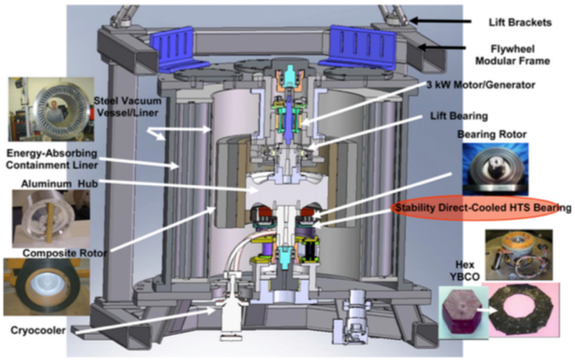

Figure 1.36– Overview of design for an energy storage flywheel from Boeing utilising (RE)BCO bulks for contactless bearings, taken from [104].

1.7.4 MRI and NMR

Both Magnetic Resonance Imaging, MRI, and Nuclear Magnetic Resonance, NMR, place stringent constraints on the quality of the field source – both spatial uniformity and temporal stability. Flux creep can be reduced as described in section 1.4.5.1, but the magnetic field above a trapped field magnet is far from uniform. However, Nakamura et al. has successfully used stack of $EuBa_2Cu_3O_y$ bulk annuli as a 4.74 T field source for MRI with a 23 mm diameter warm bore, using it to image a mouse foetus (Figure 1.37) with a 50 μm^3 size voxel resolution [105].

Similarly, a stack of 46mm wide (RE)BCO tape from American Superconductor was used to make a 25 mm bore magnet for NMR applications [106] (see Figure 1.24). A field of 3.05 T was trapped at 4.2 K, corresponding to a resonance frequency of 130 MHz.

The above shows, that superconducting trapped field magnets are considered even for applications with most demanding requirements for field quality.

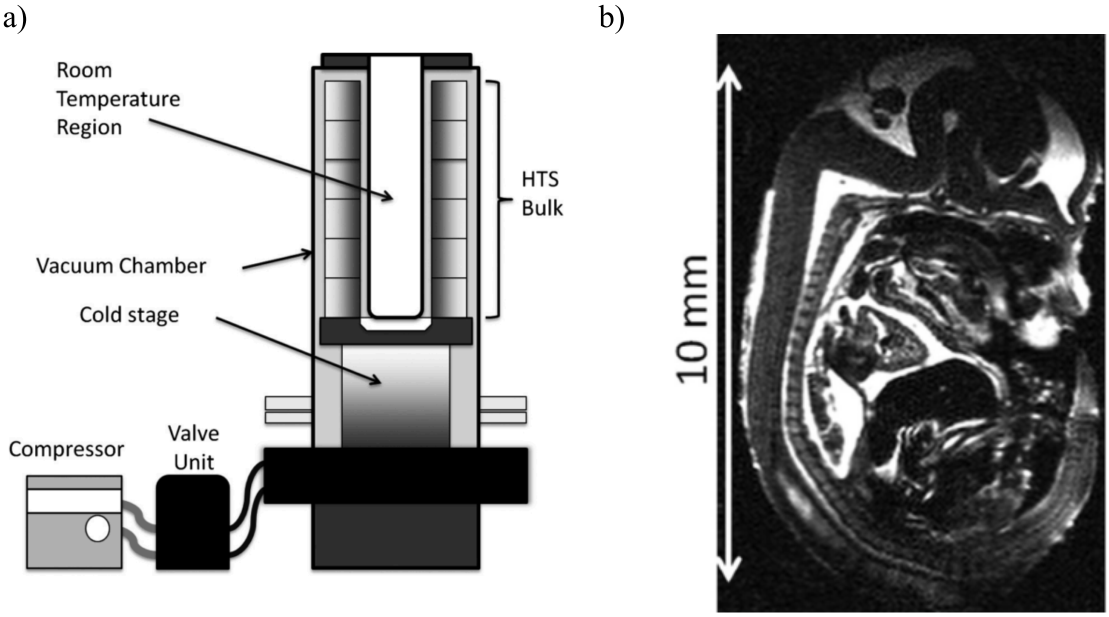

Figure 1.37– a) Cryostat for the superconducting bulk magnet. The stacked bulk magnets are attached on a cold stage cooled with a pulse tube refrigerator. The OD and room temperature bore (ID) of the cryostat are 88 and 23 mm respectively; b) Cross-sectional image of a mouse foetus, captured using the (RE)BCO bulk based MRI machine. Taken from [105].

1.8 Thesis

2G HTS coated conductor in stacked configurations present a new and promising alternative to bulk superconductors for permanent magnet applications. Whilst the volume fraction of the superconducting material within coated conductor is less than 6 percent, the metallic fraction in the coated conductor may help to overcome the fundamental mechanical brittleness problem that limits the performance of the bulk (RE)BCO, whilst the higher critical current density within the superconducting portion of the HTS tape partially compensates for the low volume fraction of the SC material. The metallic substrate and stabilisation layers also provide additional thermal stability. Moreover, the layered structure and metallic substrate allow for easy tailoring of properties and flexible geometry.

Considering these important differences between bulk (RE)BCO and (RE)BCO coated conductor stacks, I postulate that trapped field magnets made from stacked coated conductor can deliver similar if not better magnetic field performance with the advantage of:

- much better mechanical properties, giving reliable performance at >10 T;
- higher thermal conductivity (important for pulsed field magnetisation and field cooling at low temperatures);
- better uniformity of superconducting properties leading to predictable behaviour that can be modelled to high precision;
- no fundamental limit to the size of trapped field magnets – potentially higher trapped fields;
- layered structure helps to reduce crossed-field demagnetisation rate.

Chapter 2 Main experimental techniques

2.1 Sample preparation

Commercial 2G HTS tape samples from SuperPower, SuperOx and Fujikura were tested. All samples were provided in the form of a 12 mm wide tape (except Fujikura, 10 mm wide tape). All companies provide a variety of options for the architecture (thickness of the Hastelloy® substrate, silver over-layer and copper stabilisation). The tapes have a range of critical current values as well, therefore, the exact details of the tape structure and critical current will be detailed in the sections corresponding to the specific samples used.

Due to small thickness of the HTS tapes used, they can be cut with stationary scissors, which did not cause any detectable degradation of the tape layers. For the formation of the stacks, the tape was measured from the reel, cut into individual layers of desired aspect ratio and stacked maintaining the orientation of successive layers in the stack identical.

2.2 Critical current measurements

As discussed in Chapter 1, the main characteristic of a superconductor is the critical current and its dependence on temperature, magnetic field and its direction $J_c(T,B,\theta)$. The critical current measurement at the desired conditions is performed using a typical 4-point terminal measurements. Making sure that the current terminals are far away from the voltage measurement site ensures:

- complete current transfer from the copper and silver stabilisation (sheath material) to the superconductor;
- prevention of heating of the superconductor at the measurement site due to contact resistance at the current terminals.

The voltage, V at a level of 1 µV was measured over length $l = 1$ cm to satisfy an electric field criterion $E = 1$ µV cm^{-1}, given the magnetic field and temperature is maintained uniform across the voltage tap spacing.

For critical current measurements performed at ASCG, the current was sourced using HP 6680A power supply, whilst the sample voltage was measured using Keithley 182 nanovoltmeter. The current was ramped linearly at a rate of 4-8 A/s depending on expected critical current and the sample voltage was measured at a rate of 4 samples/s (limitation of Keithley 182). The current ramp is terminated once a pre-set sample voltage threshold is met. The measurement was controlled and logged using bespoke software. The resulting data is then fitted to a power law of the form:

$$V = El = E_0 \left(\frac{I}{I_c}\right)^n l \tag{2.1}$$

Where V is the measured voltage, l is the voltage tap spacing. The critical current I_c and the n-value are determined from the fit of equation (2.1) to the experimental data, using a voltage or electric field criterion. The choice of criterion E_0 is arbitrary, however, an electric field criterion of 1 µV/cm is often used (see Figure 2.1). Correct determination of n-value is not straight forward, and some experiments use an electric field range of 0-1 µV/cm for determining the n-value, as at higher electric fields the dissipation quickly raises the sample temperature, affecting

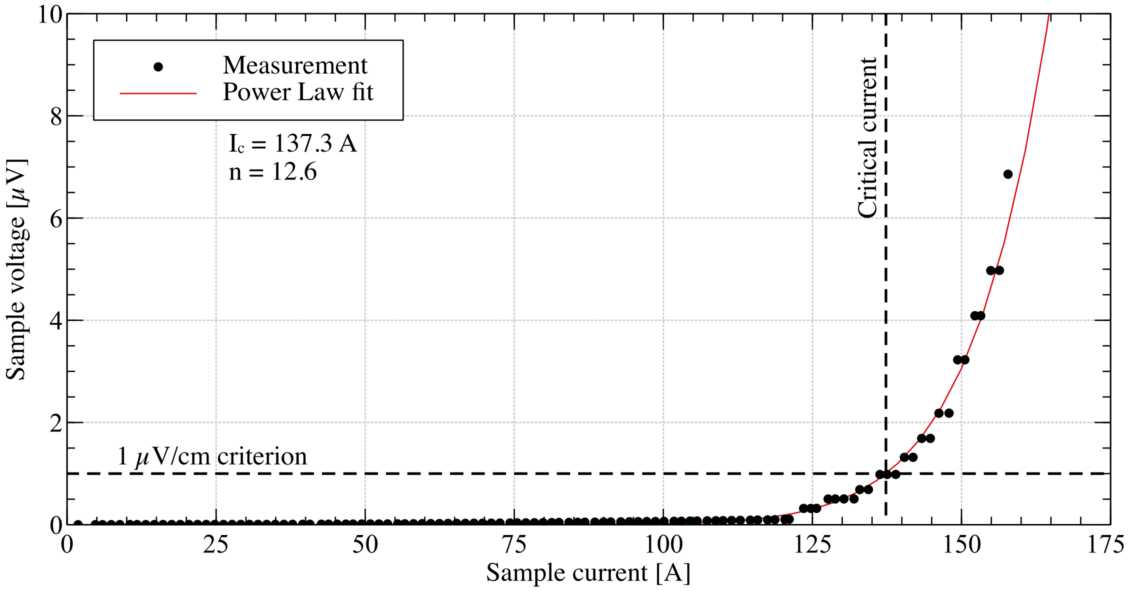

Figure 2.1– Example of a measured I-V curve of a (RE)BCO coated conductor. Sample voltage measured over a 1 cm distance. Experimental data and a power law fit is shown. The critical current and n-value is determined from the fit parameters of the power law.

the measurement. Maintaining constant sample temperature at higher electric fields and currents is not trivial even if the sample is located in a liquid cryogen due to boiling effects. When measuring in magnetic field, a Walker Scientific HV-4H electromagnet with 2-inch diameter field poles was used. The field achievable depends on the field pole spacing and was limited to 0.5 T for goniometric measurements (section 2.2.2) and 1.5 T for measurements in helium vapour flow (section 2.2.3). It is worth noting that the effect of self-field in current transport measurements is a concern for small applied fields, when the self-field is comparable to the applied field. Simulations show that the self-field on the tape (averaged across the cross-section of the tape) can reach 20 mT at currents of ~200 A. However, it is possible to extract true $J_c(B,\theta)$ for use in computer models by iterative changing of the estimated $J_c(B,\theta)$ values (from measured $I_c(B,\theta)$/area) until the measured critical current matches the modelled values using the estimated $J_c(B,\theta)$. The algorithm is described in detail in [107].

2.2.1 Measurements at 77 K in liquid nitrogen

Measurements at 77 K in self-field or low field with fixed orientation were made using the setup shown in Figure 2.2. The voltage taps can be made using spring-loaded pins that allow measurements without potentially damaging the HTS layer during soldering. This also ensures the voltage contact spacing is same for comparative measurements.

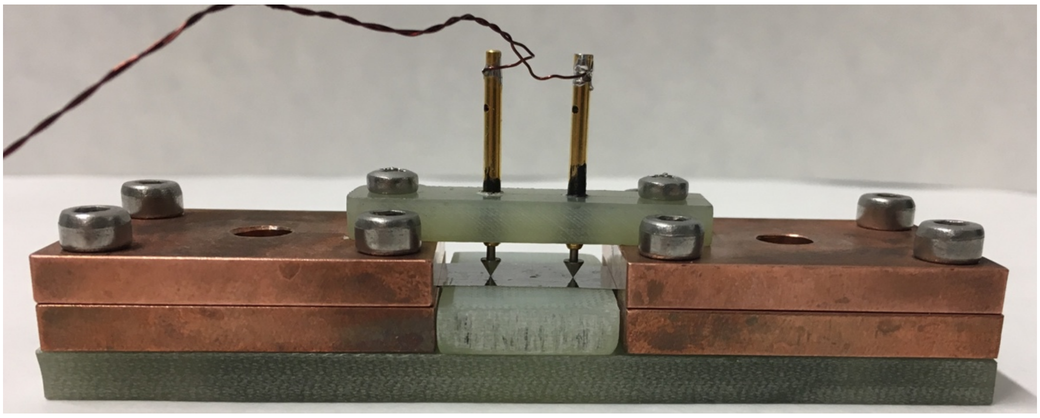

Figure 2.2– Critical current testing setup for measurements at 77 K in self-field or low field with fixed orientation. The current leads are attached to the copper blocks. The voltage taps are made using spring loaded pins.

2.2.2 Goniometric critical current measurements

The measurements of critical current dependence on the magnetic field and its direction were performed using a critical current goniometer developed in the group [108] (see Figure 2.3). The measurement equipment was detailed in section 2.2 describing the general critical current measurements. Goniometric measurements were performed at 77 K in liquid nitrogen and a magnetic flux density range of 0 to 0.5 T (limited by the electromagnet). All orientations of the magnetic field with respect to the sample can be explored via changing the rotational θ and tilt angles ϕ (see Figure 2.3).

The sample voltage was measured across 1 cm and an electric field criterion of 1 μV/cm was used to determine the critical current, although values of up to 5 μV/cm were measured to make power law fits to the *I*-*V* curves in order to determine the *n*-value.

Measurements of critical current were limited to below 200 A due to limitation of the current leads. Therefore, the width of some samples was reduced when measuring in low magnetic fields. The measured I_c values were then extrapolated to those expected for full width samples by direct comparison of values obtained for both half-width and full width samples at 0.5 T and self-field.

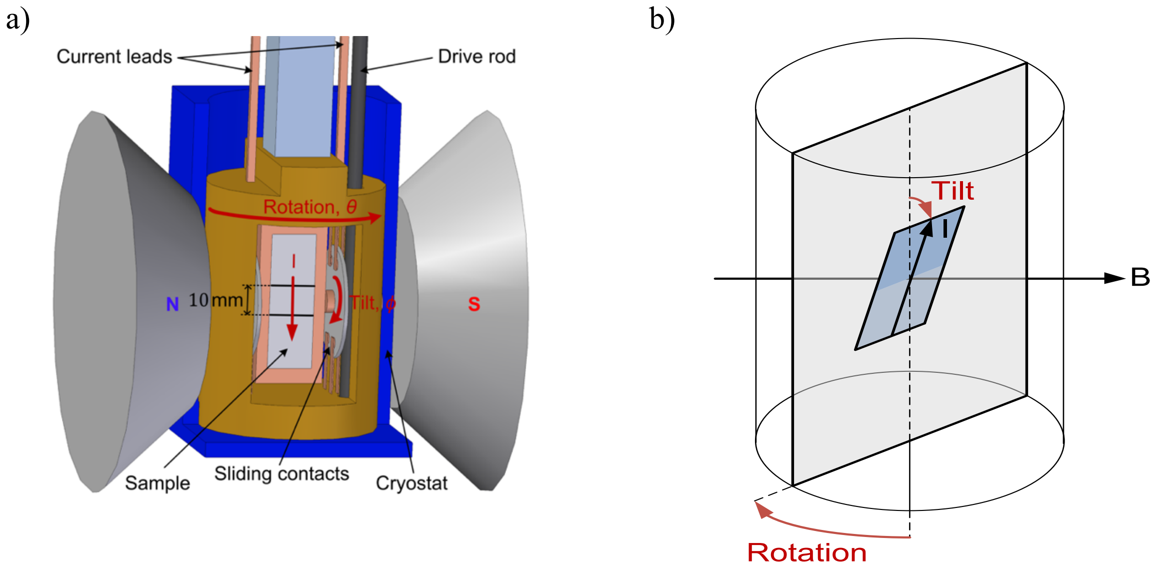

Figure 2.3– a) Schematic representation of the experimental setup a) and the geometry of the applied field with respect to rotation and tilt angles b). From [108].

However, this setup is only suitable for use at liquid nitrogen temperatures, and due to the large dimensions of the sample rotation mechanism, the magnetic field is very limited. The next section describes the development of a new system capable of measuring I_c at lower temperatures, higher magnetic fields and currents.

2.2.3 He vapour cooled critical current testing system

The current a given superconductor can carry depends on a multitude of variables including temperature, magnitude of the magnetic field and its direction. These data are important when designing and optimizing conductor materials for applications, and can serve as inputs for computer models [109,110] used to validate new designs of superconducting devices.

Critical current, I_c, is often measured for a sample immersed in a cryogenic liquid such as liquid nitrogen (77.4 K) or liquid helium (4.2 K). Close contact with the cooling medium provides cooling for non-superconductive parts of the testing rig, i.e. current leads and sample contacts. However, for intermediate temperatures, choices of cooling system are limited. Cryocoolers are increasingly popular, but their cooling power is still modest, cool-down to testing temperature can take hours and a substantial capital investment is required, making them unfeasible for smaller institutions. On the other hand, flow cryostat facilities tend to be bulky and require a magnet to be integrated into the system, increasing the cost [111,112].

I propose a new, low-cost system for critical current testing in a wide range of temperatures from 10 to 65 K and magnetic fields of up to 1.5 T [113], which in this case was limited by the electromagnet used. Due to the low achievable base temperature, the system is suitable for critical current measurements of materials such as MgB_2, rare-earth cuprates and iron-based superconductors. Samples of up to 16 cm in length can be measured. The system allows for testing of a variety of materials in a cost-effective manner. The design and construction of the critical current measurement system is outlined in section 2.2.3.1, and initial data collected with the system are presented in section 2.2.3.6.

2.2.3.1 Design of the critical current measurement system

The design of a critical current measurement system must take into account a number of design considerations and constraints, including cryogenic insulation and temperature control, very large current handling capability, applied magnetic field and forces on the sample and the system components due to said field. The cryogenic environment and the presence of large magnetic fields also dictates the choice of materials and components.

A schematic outline of the system is provided in Figure 2.4a. The simplicity of the concept allows the system to be modular and easy to maintain. A vacuum walled sample tube is placed on the liquid helium transfer dewar, without tampering with the safety features and pressure release valves of the dewar. A heater inside the dewar is used to evaporate the helium (evaporation heater) that controls the gas flow rate of helium vapor, whilst another heater in the neck of the dewar is used to adjust the temperature of the vapor (gas heater), and hence control the sample temperature. The gas heater is controlled via a three-term proportional-integral-derivative control loop (PID loop) to set the sample temperature. Having two heaters allows the helium flow rate and sample temperature to be set independently. The resulting helium boil-off can, in principle, be collected for re-liquefaction.

The magnetic field was applied externally by an electromagnet, but any other source of magnetic field can be used, e.g. a permanent magnet. In each case, fields approaching 2 T can be achieved, even without the use of superconducting magnets.

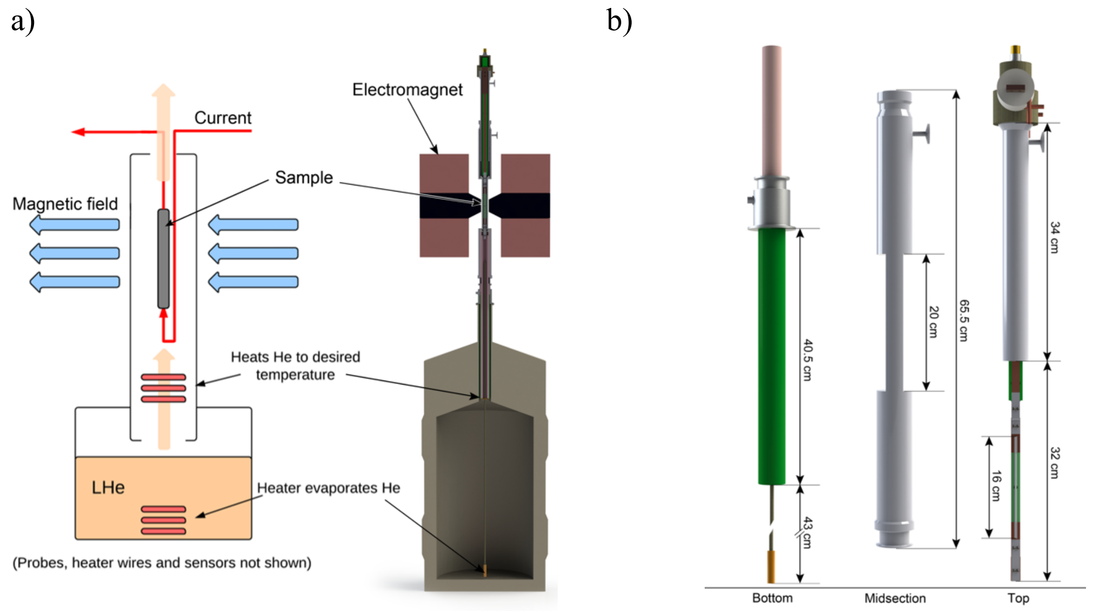

Figure 2.4– a) A schematic sketch of the critical current measurement system. Probes, heater wires and sensors are not shown. Blue arrows indicate the applied magnetic field, while LHe denotes liquid helium. b) The illustration shows the three separate parts forming the critical current testing facility, starting from the bottom-most part on the left, which inserts directly into a regular helium transfer dewar. The sample is placed on the topmost part, which slides into the midsection.

Lastly, as soon as the desired temperature is stabilized and the magnetic field applied, current is ramped through the sample until the critical current criterion is met. The procedure is repeated at multiple temperatures and magnetic field values in a sequential manner to characterize the sample with minimum liquid helium usage. At this point the system can be warmed up and another sample mounted.

2.2.3.2 Construction and materials used

The design of the system is modular. The system is composed of three discrete components as illustrated in Figure 2.4b. The bottom part inserts into the dewar and contains two heaters, whose purpose is discussed in section 2.2.3.3.

The midsection is primarily structural. The narrow section is only 25 mm wide, allowing for the spacing of the electromagnet poles to be small, increasing the magnetic flux density. The whole component is vacuum-walled and contains guides for the topmost part, which holds the sample.

The topmost part holds the sample board and all the sensors and measurement wires. Its vertical position can be adjusted, so that the sample can be centred between the electromagnet poles. Furthermore, the topmost part can be rotated about its axis to orient the sample in the magnetic field. Hence, conductor anisotropy of I_c in magnetic field can be measured.

The low temperatures and high magnetic fields put constraints on the materials used in the system. Therefore, the vacuum walled parts were made of non-magnetic stainless steel 316 with outer walls being thicker for structural rigidity (2 mm and 1 mm wall thickness for the midsection and topmost parts respectively), while the inner walls were made thinner to minimize thermal mass (less than 0.5 mm in each case). Care was taken to choose non-magnetic parts for all components near the magnetic field. The sample may experience significant forces during measurement, hence the central sample support in the topmost part was chosen to be glass-fiber/epoxy composite G10 from Tufnol due to its high strength, excellent stiffness, low thermal conductivity and excellent electrical insulation characteristics. Other parts that require non-conductive material like the cap on the topmost part were also manufactured out of Tufnol composite, but with cotton fibres for to easier machinability.

2.2.3.3 Cooling system and thermal insulation

The temperature is actively controlled via two heaters, made of coiled resistive Kanthal wire. Heater 1, referred to as the evaporator, controls the flow rate of helium gas in the system and thus the minimum achievable temperature. Figure 2.5a illustrates the temperatures achieved for given helium consumption. The temperature is asymptotic to 10 K, which is set by the thermal insulation of the cryostat and the heat leak through the current leads to the sample. The helium consumption is relatively small for temperatures above 15 K, considering that a typical critical current measurement takes less than 2 minutes, and the temperature can be stabilized in less than 5 minutes if the temperature set-point is changed by less than 20 K. Given the increasing helium price [28] it is important to keep the helium usage as low as possible.

In most cases it is convenient to decouple the helium gas flow rate and sample temperature, to obtain variable cooling power at a constant temperature. Therefore, the gas heater, located in the neck of the dewar, is used to adjust the temperature of the helium gas to the required value. The gas heater is in a PID loop with sample temperature as the input, which helps to eliminate temperature drift as the system cools or during a current ramp.

Current to the sample is supplied via superconducting (RE)BCO coated conductor leads, however they are coupled to the outside by large copper terminals, required due to currents of up to 900 A. These terminals present a thermal leak into the system. Moreover, the junction

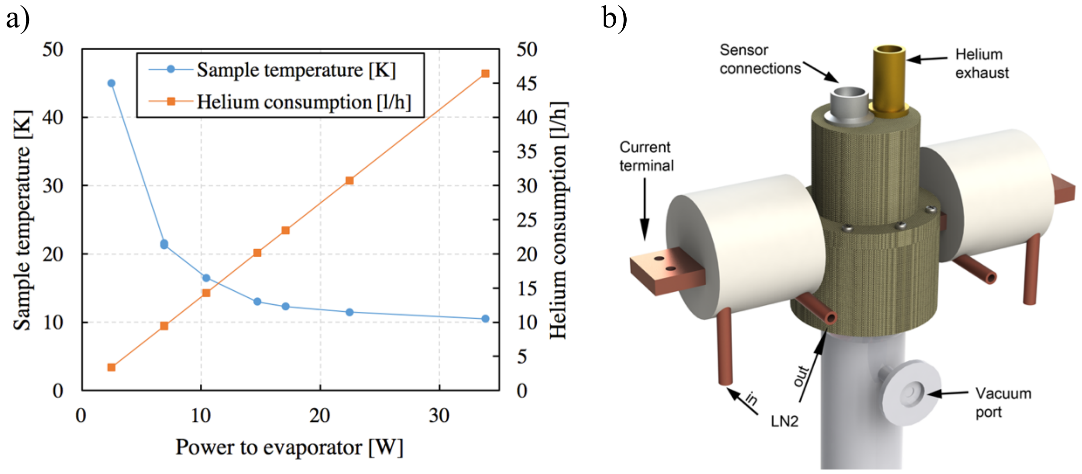

Figure 2.5– a) the minimum sample temperature and helium consumption rate for a given power supplied to the evaporation heater; b) illustration showing the copper terminals supplying the current to the sample. The terminals are pre-cooled via liquid nitrogen passed through copper tubing soldered to the current terminals. The copper tubing is encased in polystyrene insulation.

between the superconducting current leads and the copper terminals must be kept below the critical temperature of the current leads by an acceptable margin.

For these reasons, the copper current terminals are pre-cooled by liquid nitrogen. Figure 2.5b shows the copper tubing coiled around and soldered to the current terminals. The copper tubing is encased in polystyrene insulation, to further minimize the heat leak. Liquid nitrogen is passed through the copper tubing. The tubing on the two copper terminals can be connected in series via a non-conducting link. The precooling helps to dissipate the heat generated in the copper during a current ramp and anchor the temperature of the top of the superconductive current leads close to ~77 K.

One of the key features of the cryostat is the narrow section where the sample is contained, allowing the poles of the electromagnet to be separated by only 25 mm. The sample space is 16 mm wide leaving a thermal gradient of up to 280 K over 4.5 mm. For this reason, the thermal insulation of the cryostat is of paramount importance. The cryostat is composed of two cylindrical parts labelled as the midsection and topmost parts in Figure 2.4b, each of which are vacuum walled. The two parts slide into each other and are linked by an Ultra-Torr compression

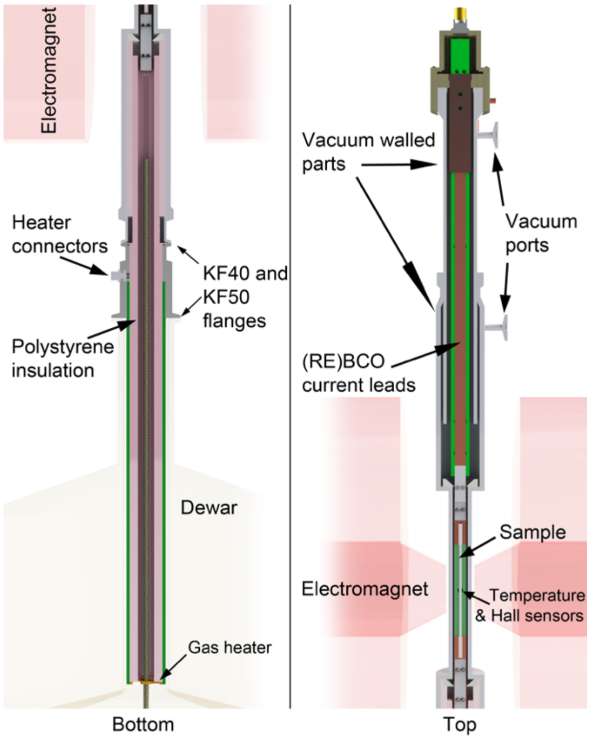

Figure 2.6– Illustration of various parts of the cryostat. The image is split into two parts, the left image showing the bottom half and the right showing the top part of the cryostat. Parts made of glass fibre reinforced resin G10 shown in green.

fitting from Swagelok®. This allows the vertical sample position as well as orientation to be changed, while overlapping vacuum insulated sections maintain good thermal insulation. The vacuum walls are evacuated prior to each experiment and sealed by a vacuum valve. Even better performance is expected if the cryostat is pumped continuously during the experiment. The link between the cryostat and the dewar is insulated by overlapping sections of expanded polystyrene as illustrated in Figure 2.6.

To estimate the thermal loses and identify possible ways to reduce helium consumption, four cryogenic temperature sensors were placed in different parts of the system, allowing heat losses to be estimated in different segments of the system from the thermal gradients. The measurements were made once the system reached thermal equilibrium for estimates of static heat loss. It is worth noting that temperature gradients across the system are much lower during actual sample testing, as a higher helium flow rate is used than the minimum needed to reach the target temperature. Instead, the second (gas) heater is used to maintain the desired temperature. Also segment 4 in Figure 2.7 does not contribute to the sample temperature as it is upstream of the sample, and a high temperature gradient is expected as the top of segment 4 is weakly clamped to 77 K by the LN_2 cooled copper terminals.

Initial tests showed substantial heat losses in segment 2, exceeding 180 W at a He flow rate of 1.6 g/s. The losses were successfully reduced to 17 W by placing the gas heater lower down in segment 1, and installing overlapping polyurethane foam insulation on the inside, extending across the joint connecting the bottom and midsection parts of the system (see Figure 2.6).

At the lowest temperatures, heat losses are dominated by segment 3, which are due to radiation losses across the vacuum double wall (up to 10 W by approximating the segment as concentric cylinders and assuming an emissivity of 0.6 for unpolished stainless steel), radiation from the top of the system and conduction across the sample rod and current leads (<1 W), and residual pressure in the vacuum walled cryostat as it is not pumped during the experiment. Localized frost points were observed at low temperatures in segment 3, and contact bridges between vacuum walls were suspected due to imperfections in the manufactured part and the small separation of the walls, with the vacuum gap of less than 2 mm. These contact bridges are expected to contribute significantly to losses at low temperatures.

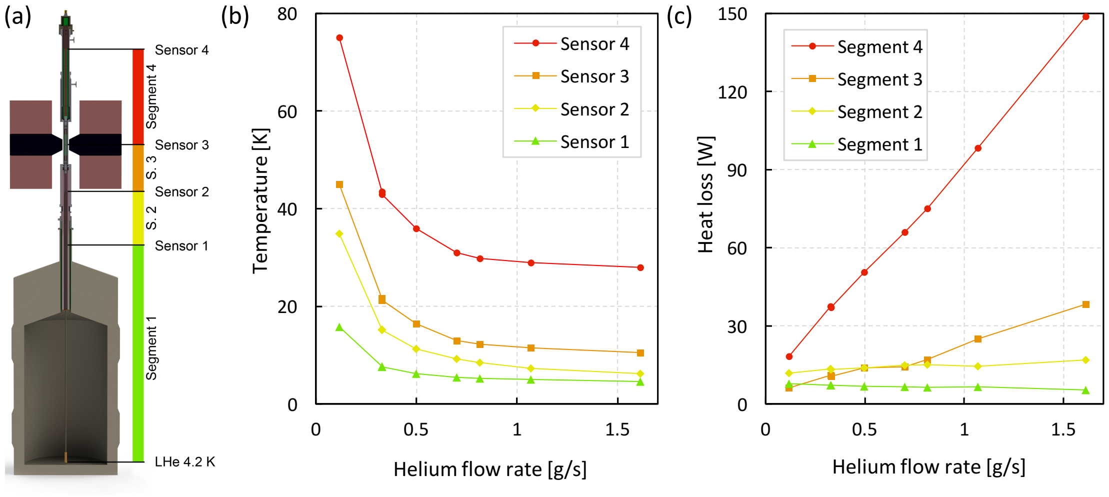

Figure 2.7– The temperatures (b) at different positions (a) along the system as a function of helium flow rate, as well as estimates of the heat loss in the segments between the measured temperature sensors (c).

2.2.3.4 Sample mounting and current leads

One of the major considerations when designing the system was achieving fast sample exchange, whilst retaining the possibility of re-measuring samples at a later date without re-soldering. The samples are soldered to a sample board only once, and the sample is kept on the sample board permanently. The sample board is affixed to the measuring probe via flexible silver joints as shown in Figure 2.8a. It is expected that the largest heat source in the system will be the sample contacts, hence to further decrease the contact resistance a strip of indium foil is inserted between the silver tabs and the sample.

Samples of up to 16 cm in length can be measured, ensuring that at the measuring point all of the current is in the superconductor even if the superconducting wire/tape has a high resistivity sheath material [114,115]. The voltage drop, temperature and magnetic field are measured in the centre of the sample board. The sample board has a hole for a carbon ceramic temperature sensor which is attached to the test probe as illustrated in Figure 2.8a. Apiezon N thermal grease is applied between the sample and the temperature sensor to ensure good thermal contact. Two perpendicular GaAs based Hall effect sensors HG-116C from Asahi Kasei are placed next to the temperature sensor, to measure the magnetic field strength and its orientation. The voltage drop across the superconductor is measured across 1 cm above the temperature sensor.

Current to the sample is supplied by superconducting current leads. Each current lead is composed of three stacked (RE)BCO tapes supplied by SuperPower: details are given in section

2.2.3.6. The operating temperature of the current leads is kept below 77 K. The temperature of the current leads is monitored near the terminations with a carbon ceramic temperature sensor and the current is cut automatically if for some reason it exceeds 77 K to prevent damage. Also, in case of a short term overcurrent, a 100 µm thick silver shunt is attached parallel to both current leads.

Superconducting current leads help to save space and reduce heat leak into the system, however, they also limit the upper operating temperature of the system. The current leads must be maintained superconducting during operation, unless very small currents are used. The silver shunt can carry a current of 10s of Amps without significant heating. This makes the system usable for measurements near T_c of high temperature superconductors (HTS) such as (RE)BCO as well.

2.2.3.5 Control and measurement system

A simplified block diagram of the control and measurement system is depicted in Figure 2.8b. The temperature is controlled via a PID loop implemented in software. Sample temperature (process variable) is measured via a National Instruments (NI) 6363 digital acquisition system

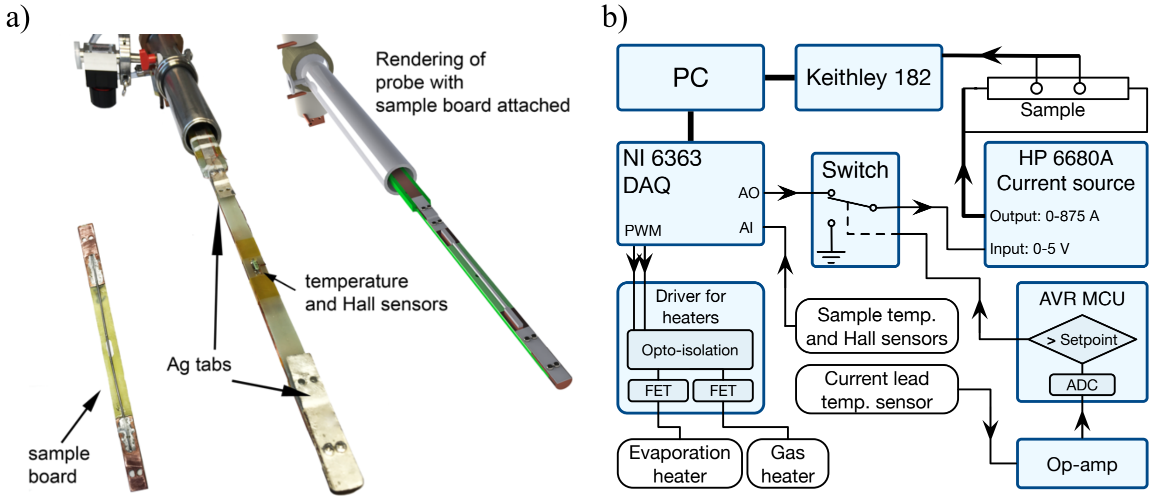

Figure 2.8– a) photographs of the sample board with a MgB_2 sample illustrating how it is attached to the measurement probe. The location of the temperature and Hall sensors is also indicated.; b) Simplified block diagram of the measurement and control equipment used. Acronyms used: AI/AO – analog input/output; PWM – pulse width modulated signal; FET – field effect transistor driving the heaters; AVR MCU – microcontroller with ADC (analog-to-digital converter) outputting a high signal when temperature of current leads exceeds a set point.

(DAQ). The gas heater power (control variable) is controlled by a pulse width modulated (PWM) signal generated by the DAQ which is fed into an opto-isolated driver circuit. The power of the evaporation heater is set independently.

Current to the sample is supplied by a Hewlett Packard (HP) 6680A current source controlled via an analog input by the National Instruments DAQ. The actual current supplied to the sample is read back directly from the power supply via GPIB interface. The current can be cut quickly if the temperature of the current leads becomes too high. This is done by monitoring the temperature sensor located on the current leads. The temperature sensor voltage is first amplified by an instrumentation amplifier then read by a microprocessor. If the temperature exceeds a set point of ~77 K, the microprocessor outputs a high signal to an analog switch IC, which grounds the input of the current source. Implementing the protection in separate hardware adds redundancy and avoids communication delays that are present between the DAQ and PC.

The magnetic field is applied using a Walker Scientific HV-4H electromagnet with 2-inch diameter field poles. The magnetic field and its direction is measured with Hall probes on the sample probe using the NI 6363 DAQ. The voltage drop across the superconducting sample is measured using a Keithley 182 sensitive digital voltmeter. The experiment was controlled using bespoke software.

2.2.3.6 Measurement system validation

For a system test run, the critical current of a 2G HTS (RE)BCO tape from SuperPower was tested, with the same specification as the one used for the current leads in the system. The sample was tested at a magnetic flux density of 1 T with magnetic field parallel and perpendicular to the tape surface in a temperature range from 40 K to 60 K. An MgB_2 wire was also tested at 1 T in a temperature range from 20 to 40 K.

The (RE)BCO sample measured was produced by SuperPower with specification SCS12050-AP. The tape has a width of 12 mm, 50 µm Hastelloy substrate, 2 µm silver over-layer and 20 µm copper stabilizer. At 77 K and self-field the tape has a minimum I_c of 309 A, while the average is 340 A, as stated by the manufacturer. Given the large critical currents expected at a field of 1 T (I_c for the full width sample exceeds 1000 A at 45 K), the tape width was reduced to 4 mm for testing. The critical current was also measured at 77 K in liquid nitrogen.

The MgB_2 sample was produced by Columbus Superconductors, specification 700RM13609. The wire is 1.52 mm in diameter and has a Monel sheath. The conductor contains 37 MgB_2 filaments in a Ni matrix. Reference data from the manufacturer for a wire of this specification are shown in Figure 2.9.

The sample voltage was measured across 1 cm of the superconductor and a criterion of 1 µV/cm was used to determine the critical current. The current ramp rate of 8–10 A/s was used for critical currents larger than 100 A, and as low as 5 A/s for lower currents. Sample voltage and current measurements were taken at a rate of 4 samples/second.

The critical current of the (RE)BCO coated conductor was measured at 1 T with the direction of the magnetic field parallel and perpendicular to the plane of the tape, and perpendicular to the current direction. The results are shown in Figure 2.9. Critical currents in the temperature range of 40–60 K were measured using the system described in section 2.2.3.1, whereas the measurements at 77 K were performed in liquid nitrogen. Measurements from the MgB_2 sample are also included, along with reference data from the manufacturer for wire of the same specification. The measurements match the reference data well. Some deviations from the reference data are expected as the supplied reference data are not for the same batch.

Due to the low thermal mass of the system, the time required to stabilize at a new temperature was below 1 min for temperature steps as large as 10 K. The overall cooling time to 60 K from room temperature was about 8 min once the probe was attached to the helium dewar. Cooling

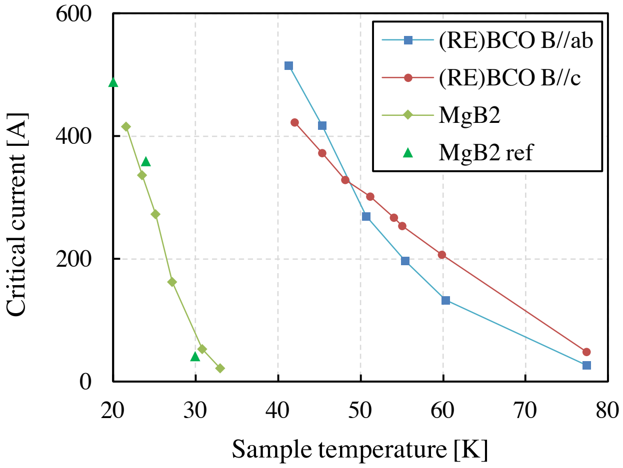

Figure 2.9– Critical current data measured with the system described in this work. 4 mm wide sample of (RE)BCO tape was tested at a field of 1 T parallel and perpendicular to the width of the tape (near *a-b* lattice plane). Measurements at 77 K were made in liquid nitrogen. MgB_2 sample was also tested at a field of 1 T and displayed in the graph together with reference data obtained from manufacturer (MgB2 ref series).

in a gaseous medium provides some flexibility of sample geometry, however it also presents some challenges. During the superconducting-normal transition, heat is generated in the sample, and due to the steep I-V curve, the sample temperature may suddenly change, which is hard to adjust for quickly. This is partially helped by increasing the helium gas flow (but maintaining the same temperature) which effectively increases the cooling power in case of a sample temperature change, however this also increases the helium consumption. Due to these effects it may be difficult to determine accurate n-values, but the I_c value is more accurate due to the n-value being large in most cases. Possible system improvements to allow n-value estimation are outlined in section 2.2.3.7. Nevertheless, temperature stability better than 0.2 K is maintained during the current ramp before the onset of the transition.

2.2.3.7 Further improvements

Further planned improvements to the system include faster sample voltage acquisition, allowing n-value measurements in the range of E = 0.1–1 μV/cm where sample heating is negligible, as in [116]. Currently the acquisition rate is limited to 4 samples/second: readings are transferred from the Keithley 182 in real time over GPIB, to allow the current ramp to be terminated under software control when a threshold voltage is reached. This rate can be increased to 15 samples/second by buffering samples before readout, triggering the end of the current ramp using the pre-amplified analogue output of the Keithley 182. This would also allow the ramp to be ended more quickly at the pre-set threshold voltage, reducing over-heating of the sample, which is particularly useful for measuring poorly-stabilized samples.

There is scope to further reduce heat losses by continuously pumping the vacuum spaces. Some helium is also lost during insertion of the probe into the dewar that could in principle be used for pre-cooling the system. Nevertheless, full characterization of a single sample can be achieved with 5–10 l of liquid helium, depending on the temperature range and number of data points gathered. For example, characterization of the MgB_2 sample at 1 T used 5–6 l of liquid helium, with a significant fraction of this expended during the initial insertion of the probe into the dewar.

Currently the sample orientation with respect to the magnetic field is changed manually, but this could be automated using an approach similar to the one described in [108].

2.3 Hall-probe measurements

A picture of the Hall probe measurement system used is given in Figure 2.10. Once the coil is energised, sample with the 3-axis scanning stage is inserted into the coil. The sample is then cooled by liquid nitrogen. After sample is cooled down, the coil current is slowly ramped down and the scan is commenced after a set time (at least 2 minutes) to allow for rapid relaxation of the trapped field just after magnetisation. This in effect results in field cooling of samples in fields of up to ~120 mT (limited by the coil). Scan height can be freely adjusted and is usually in the range of 0.3-1.0 mm. The Hall effect sensor used was Arepoc HHP-VA with an active area of 50 × 50 μm.

Single tapes are scanned via securing them with vacuum grease to the sample stage and non-bonded stacks of SC tapes are scanned in a stainless steel (non-magnetic) sample holder as shown in Figure 4.2. After subtraction of offset voltage (and any background field) and adjusting for calibration of the Hall probe, the trapped field profile can be plotted using conventional tools. Further analysis to find the current distribution was carried out as described in section 2.3.1.

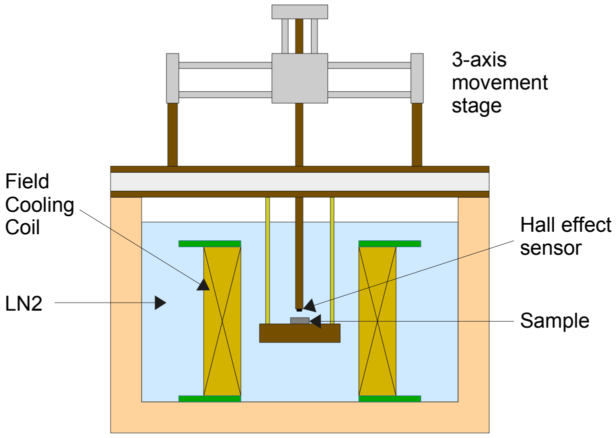

Figure 2.10–Hall probe scanning setup. Sample is scanned immersed in liquid nitrogen. Sample is magnetised using either zero field cooling or field cooling.

2.3.1 Current density reconstruction

Commercial tape is usually characterised by the rated critical current I_c at 77 K, self field. Moreover, the I_c value is usually given only at several locations along the length, or as value describing overall behaviour of a longer section. Longitudinal defects in the tape would not result in a significant degradation of transport current, but would significantly degrade the field trapped in the layer.

Hall probe scans can indicate whether there is a defect and the overall performance of the tape, however, the nature of the defect may be difficult to elucidate, and the exact value of the current within the tape can't easily be calculated without simplifying assumptions, and only in a sample that does not contain major defects. In the context of stacks of SC tape, knowing the distribution of the current also aids in determining whether any defects were introduced by handling of the tape, e.g. cutting of the tape into segments, etc.

Here I implement a method described in [117,118] to map the current within a SC tape from a Hall probe scan. The method assumes the current is confined into infinitesimally thin plane, and it is as follows:

we calculate the *z* component (parallel to normal direction of the HTS tape) of the flux density at the surface using the flux density at height h above the sample:

$$\widehat{B_{z0}}(k_x, k_y) = e^{kh}\widehat{B_z}(k_x, k_y) \tag{2.2}$$

where $\widehat{B_z}$ is the Fourier transform of B_z, k is the magnitude of the wavevector. The side-effect of equation (2.2) is that high spatial frequency noise (large k values) get amplified preferentially. To avoid this, we apply a Hanning window filter to the flux density in the frequency domain. The filter is defined as:

$$w(k) = \begin{cases} \left[1 + \cos\left(\dfrac{k}{k_{cut-off}}\pi\right)\right]/2 & \text{for } k \le k_{cut-off} \\ 0 & \text{for } k > k_{cut-off} \end{cases} \tag{2.3}$$

where $k_{\text{cut-off}} = 2\pi/\lambda_{\text{cut-off}}$ and $\lambda_{\text{cut-off}}$ sets the spatial resolution of the reconstruction.

As the high spatial frequency noise is introduced in proportion to the scan height, it is often not the *x* or *y* step that limits the resolution, but the scan height, *z*, and hence the filter cut-off $\lambda_{\text{cut-off}}$. For this reason, it is essential to keep the scan height as small as possible, however sample flatness can become an issue. The Fourier transforms of the current density are then given by:

$$\widehat{J_x}(k_x, k_y) = -i\frac{2}{\mu_0}\frac{k_y}{k}w(k)\widehat{B_{z0}}(k_x, k_y) \tag{2.4}$$

$$\widehat{J_y}(k_x, k_y) = i\frac{2}{\mu_0}\frac{k_x}{k}w(k)\widehat{B_{z0}}(k_x, k_y) \tag{2.5}$$

And finally, the current distribution is then given by the inverse Fourier transform of $\widehat{J_x}$ and $\widehat{J_y}$. Figure 2.11 shows an example of current reconstruction in a field-cooled layer of HTS tape before and after deliberate introduction of defects. Even small defects are clearly visible in the reconstructed current density, as well as in the trapped field profile. The algorithm was implemented in Matlab and the code is given in the Appendix A.

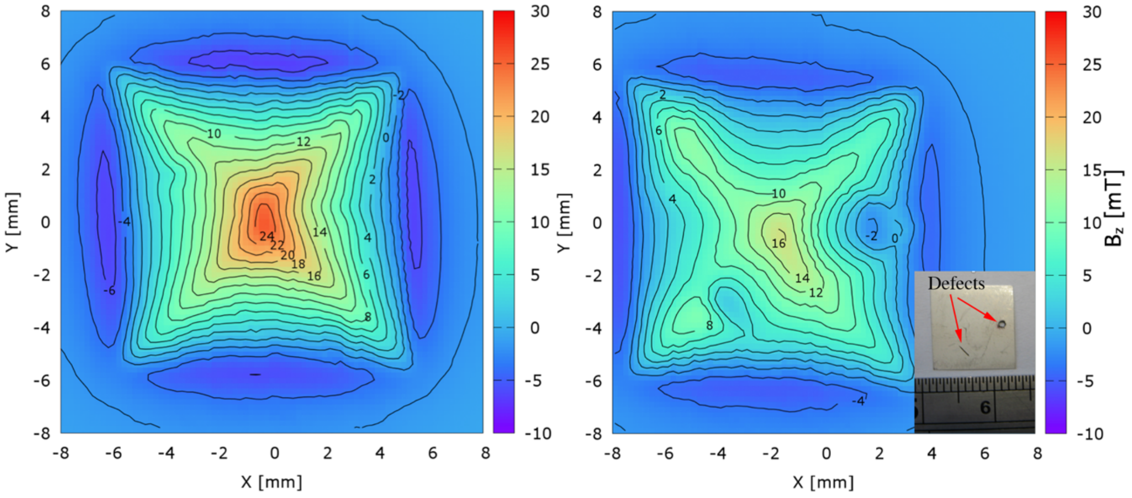

12 mm square, undamaged 12 mm square, with defects

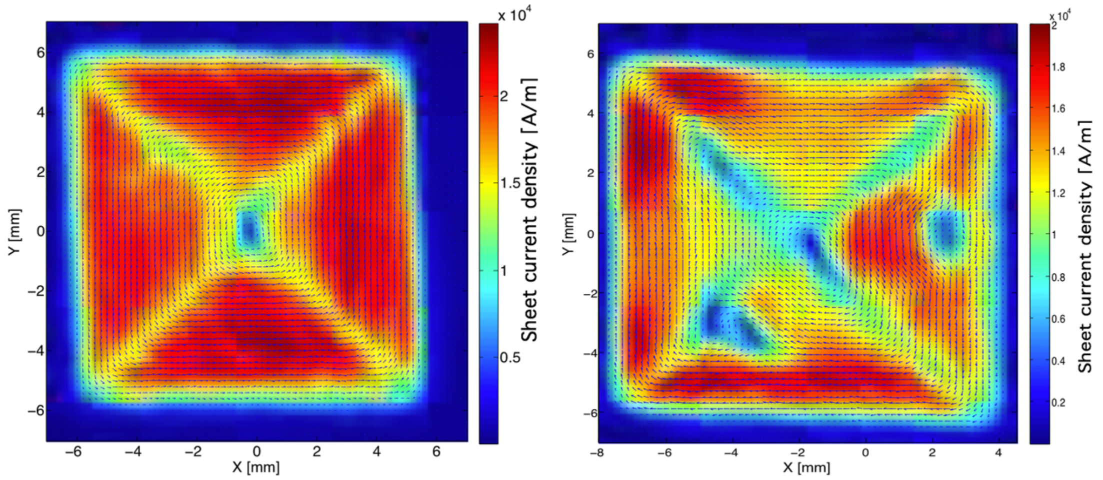

Figure 2.11– Contour plots of trapped field profile (top row) of undamaged and deliberately damaged tape. Measurement taken 0.3 mm above sample surface. Bottom row shows the corresponding current distribution in these samples. Small arrows show the direction of the local current density. The inset shows the damaged sample with a diagonal scratch (bottom left) and a perforation (right).

2.4 Pulsed field measurements

Pulsed magnetisation was performed using the experimental setup developed at the Applied Superconductivity and Cryoscience Group, University of Cambridge [119]. The system is capable of up to 8 T, 28 ms pulses (see Figure 2.12b). The pulses are applied by a copper solenoid, cooled using liquid nitrogen and powered by a bespoke capacitor bank from Metis Instruments.

The sample sits in a 5 cm diameter bore. During an experiment, the sample space is sealed, filled with helium gas and maintained at 1 atmosphere pressure for heat transfer between the coldhead of the cryocooler (connected to the wall of the sample space) to the sample. The temperature can be set between 10 K and room temperature and is controlled via an Oxford Instruments ITC 502 controller. The diagram of the apparatus is shown in Figure 2.12a. The temperature of the sample is measured using a carbon ceramic (CCS/C2) temperature sensor from TMi cryogenic, which is in contact with the sample. A linear Hall effect sensor array

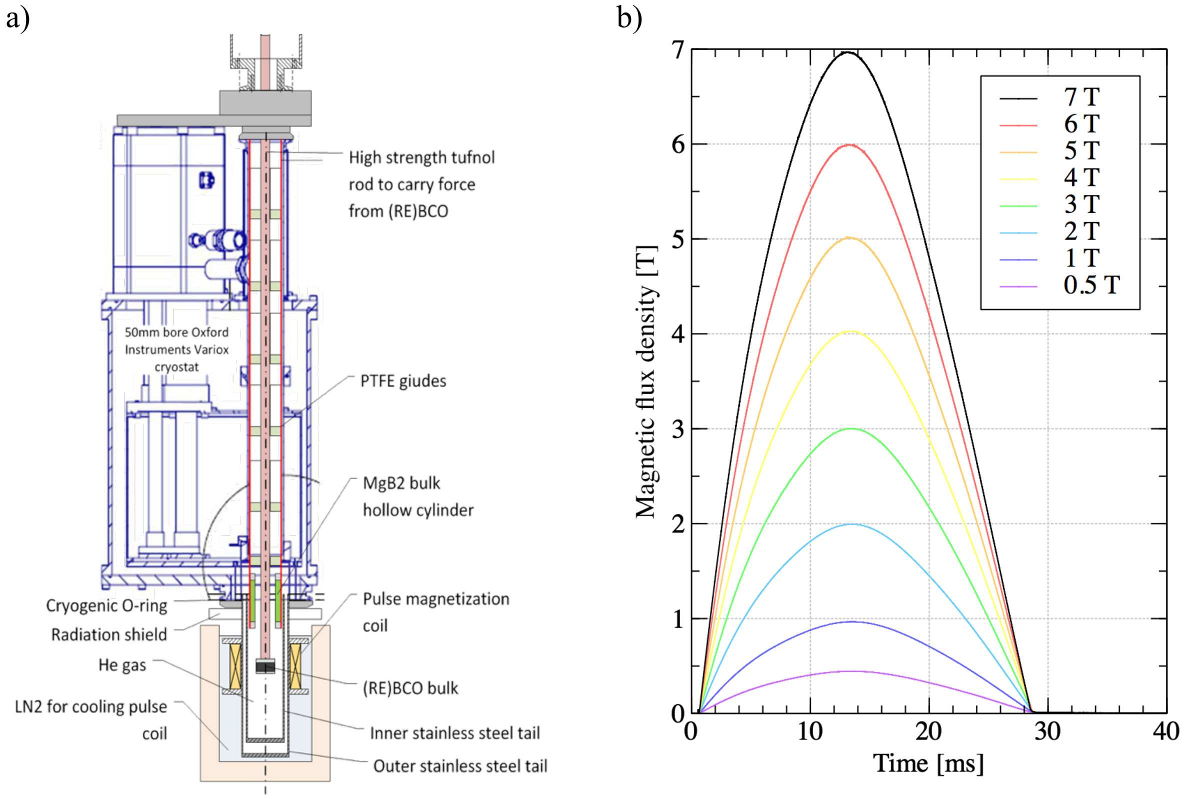

Figure 2.12– Schematic diagram of the pulse magnetisation system a) and measured magnetic field pulse shape and duration in the pulse magnetisation system b).

measures the magnetic flux density 0.5 mm above the sample surface. Magnetic flux density above the centre of the sample is measured during the pulse and a complete profile of trapped magnetic field is measured immediately after an applied pulse and then 30 s after. Using the field measurements from Hall probes and assuming rotational (round samples) or 4-fold (square stacks) symmetry of the field profile around the axis of the sample, the magnetic flux above the sample surface was estimated using numerical integration.

2.5 Field cooling measurements

2.5.1 Low field measurements at ASCG in Cambridge

Field cooling was performed at 77 K in liquid nitrogen. The magnetic field was applied using a Walker Scientific HV-4H electromagnet. The magnetic field was ramped down from 1 T at a rate of 0.1 T/s. After field cooling, the sample was removed from the electromagnet whilst keeping it in liquid nitrogen to ensure that the measurement is not affected by the proximity of ferromagnetic electromagnet poles. The field was recorded 2 minutes after the end of field cooling to ensure flux creep, which is most rapid just after magnetization, does not affect the results significantly. The field was measured 1 mm above the surface of the stack, centred in the middle. Hall effect sensor used was Arepoc HHP-MP.

2.5.2 High field measurements in ILHMFLT, Wroclaw

High field measurements were performed during visits and in collaboration with the International Laboratory of High Magnetic Fields and Low Temperatures in Wroclaw, Poland. Measurements were performed with the help of Dr Krzysztof Filar and Professor Victor I. Nizhankovski.

The Field cooling experiments were performed in a 15 T Oxford Instruments superconducting magnet with a 25 mm diameter bore. A custom sample holder (see Figure 2.13) was attached to the brass support containing a heater for temperature control. The field was measured in between two tape stacks, which were separated by 2 mm, in the central position (Arepoc LHP-MP) and off centre (HG-116C from AKM). Temperature was measured by a carbon ceramic temperature sensor (TMi cryogenics), placed directly on the aluminium sample holder and fixed by GE varnish.

The field cooling procedure involved heating the sample to above 100 K to ensure that the sample is no longer superconductive and applying magnetic field (larger than the expected trapped field). The sample was then cooled to the desired temperature, and the external magnetic field was ramped down to zero at a rate in the range of from 150 to 300 mT/min. The trapped field measurements were then taken 5 min after the end of the field cooling procedure (end of field ramp).

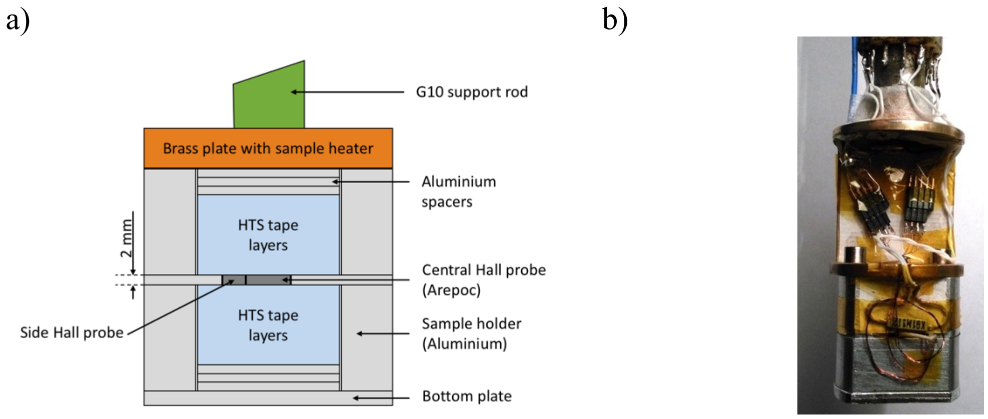

Figure 2.13– Schematic diagram a) and a photograph b) of the sample holder used for field cooling experiments.

2.6 Finite element method (FEM) modelling framework

The FEM software COMSOL Multiphysics was used to create models and run simulations. All the models were based on the *H* formulation implemented using the PDE module (partial differential equation module of COMSOL) or later natively introduced *H* formulation in the COMSOL's AC/DC module. For pulsed field magnetisation models, the thermal physics module was also coupled to simulate the thermal dynamics. 3D, 2D axis-symmetric and 2D infinite geometries were used where appropriate (as described in the individual results sections). The basis of the 3D model using the *H* formulation was constructed as described by Zhang et al. [120]. A Cartesian coordinate system was used, hence magnetic field **H** has components H_x, H_y and H_z as does the current density **J** and electric field **E**. To account for the variation of critical current density with temperature, *T*, and magnetic flux density, **B**, a direct interpolation of measured critical current data was used $J_c(T, \mathbf{B})$ when available, like what is shown in Figure 2.14.

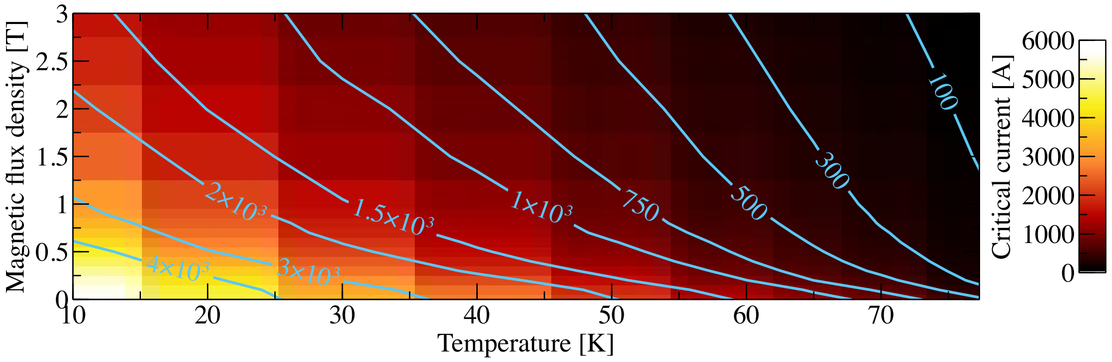

Figure 2.14– Critical current surface, for a range of temperature and magnetic field values. Data taken from [121].

If such data was not available, the Kim model [14] was used instead:

$$J_c(T,\mathbf{B}) = \ a\left[1-\left(\frac{T}{T_c}\right)^2\right]^{\frac{3}{2}} \frac{B_0}{|\mathbf{B}|+B_0} \tag{2.6}$$

The non-linear relationship between current and voltage in superconductors can be characterised by the *E*-*J* power law [122]:

$$E_i = E_0 \frac{J_i}{|\mathbf{J}|}\left(\frac{|\mathbf{J}|}{J_c(T,\mathbf{B})}\right)^n \tag{2.7}$$

This gives an effective resistivity:

$$\rho_i = E_0 \frac{1}{|\mathbf{J}|}\left(\frac{|\mathbf{J}|}{J_c(T,\mathbf{B})}\right)^n \tag{2.8}$$

where *n* is the power law exponent, and is also temperature and field dependant, as can be seen in section 5.2.1. *n*-values in the range of 10-30 are common [123]. It is worth noting, that high values of *n* tend to make simulations less stable or not converge to a solution at all. A modified version of the *E*-*J* power law, improving the convergence is discussed in section 2.6.2.

Unlike in actual YBCO, the effective resistivity is taken to be isotropic, nonetheless this approximation is appropriate as the induced currents are in *x*-*y* plane of the sample (the isotropic *a*-*b* plane in YBCO).

The current density, **J**, is given by Ampere's law. Assuming no displacement currents:

$$\mathbf{J} = \ \nabla\times\mathbf{H} \tag{2.9}$$

Then, using Faraday's law:

$$\nabla \times \mathbf{E} = \mu_0 \mu_r \frac{\partial \mathbf{H}}{\partial t} \tag{2.10}$$

Finally, by substituting (2.8) and (2.9) into (2.10) we can formulate the problem as a partial differential equation that has the magnetic field, **H**, as the independent variable:

$$\mu_0 \mu_r \frac{\partial \mathbf{H}}{\partial t} + \nabla \times (\rho \nabla \times \mathbf{H}) = 0 \tag{2.11}$$

Equation (2.11) can be recast into a form acceptable to COMSOL Multiphysics and solved for a given set of boundary conditions. The model was modified to take into account heat generation. This was achieved by introducing temperature dependent thermal properties of the materials being modelled as well as anisotropic thermal conductivity of the YBCO bulk. Temperature distribution is governed by the heat equation:

$$\rho C_p \frac{\delta T}{\delta t} - \nabla \cdot (k \nabla T) = Q_V \tag{2.12}$$

Where ρ is the density, C_p is the heat capacity at constant pressure, k is the thermal conductivity and Q_V is the volumetric heat flux generated due to dissipation of electric energy in the superconductor, and is given by:

$$Q_V = \mathbf{E} \cdot \mathbf{J} \tag{2.13}$$

2.6.1 Boundary conditions and initial values

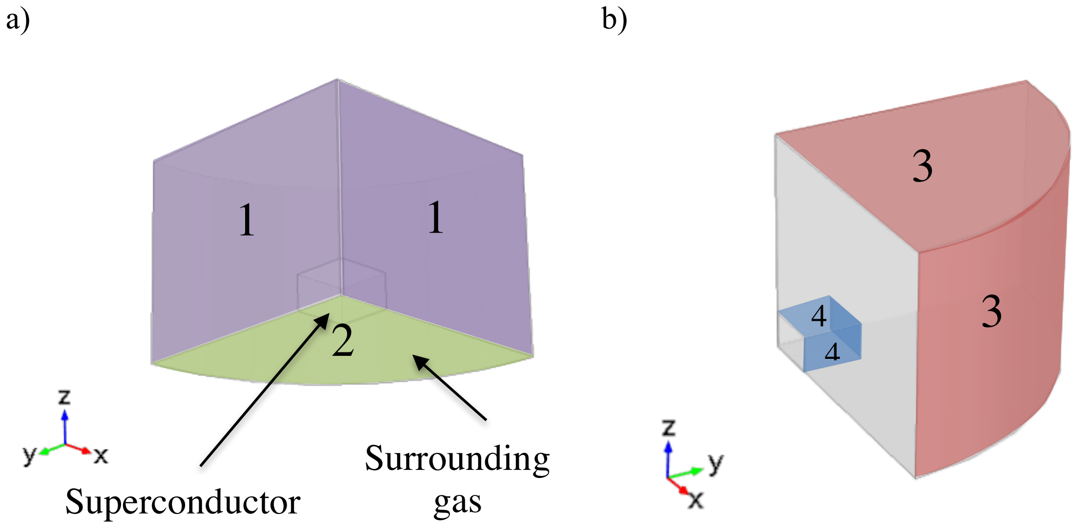

Figure 2.15– Different boundary conditions are indicated by different colours and numbered.

Models with complicated geometries and long simulated timeframes require a substantial amount of computation time. Models that optimise more than one parameter can take anywhere from a few hours to several days to complete. In order to reduce the computation time, symmetries present in the model can be exploited, however appropriate boundary conditions must be applied. As an example, the boundary conditions used to model an octant of a rectangular superconductor (Figure 2.15) are listed below in accordance with the numbers in the figure.

1. To model only 1/4 of the problem, continuity must be ensured between the two cut-faces.
2. For this plane to be a symmetry plane, a Dirichlet boundary condition must be satisfied:

$$\begin{aligned} H_x &= 0 \\ H_y &= 0 \end{aligned} \tag{2.14}$$

3. The applied field is set up as a Dirichlet boundary condition on external boundaries of the outer domain, see equation (2.15). $f(t)$ depicts the time variation of the applied field (see Figure 2.16), whilst B_a sets the magnitude of the applied field.

$$\begin{aligned} H_x &= 0 \\ H_y &= 0 \\ H_z &= (B_a/\mu_0)\cdot f(t) \end{aligned} \tag{2.15}$$

4. To simulate the cooling effect of helium (used as a heat transfer gas in the experimental setup), a boundary heat source was applied on the external surfaces of the coldhead. The behaviour is summarised in equation (2.16).

$$P = \begin{cases} 0 & T < T_0 \\ Q_c(T - T_0) & T_0 \le T \le (T_0 + 15) \\ 15Q_c & T > (T_0 + 15) \end{cases} \tag{2.16}$$

The cooling power is set to be linearly proportional to the difference between the surface temperature T and the equilibrium temperature T_0. The cooling power saturates at 30 W when the difference exceeds 15 K. This behaviour is representative of the cryocooler used in the experimental setup described in section 2.4.

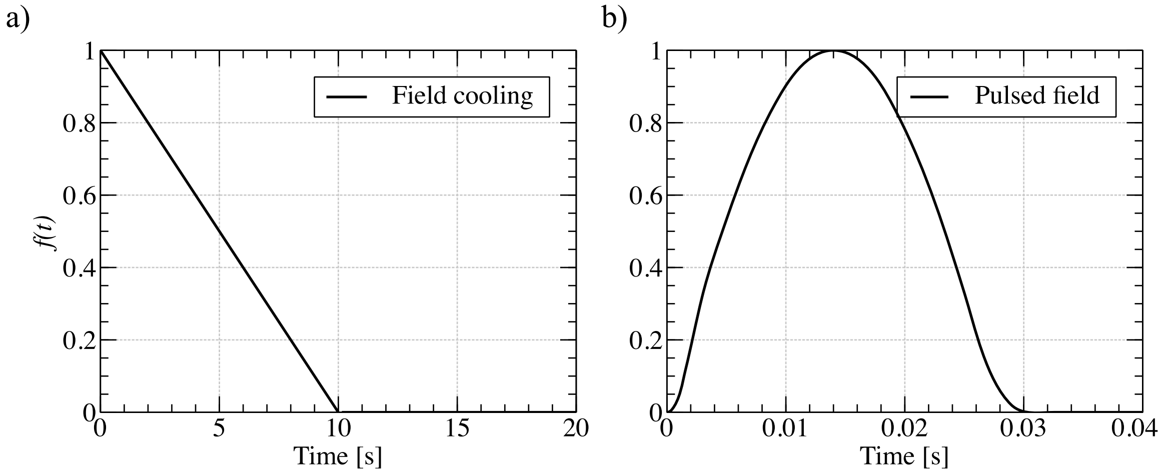

Figure 2.16– Time variation of applied field for field-cooling a) and pulsed magnetisation b).

2.6.2 Modified *E-J* power law

E-J or *I-V* power law has been successfully used to model superconductors in many occasions [110]. However, it is highly non-linear, leading to computational difficulties. During pulsed field magnetisation, currents higher than the critical current can be induced, and in this region, the electric field quickly diverges to infinity. To make the simulations more stable, a limit to electric field can be implemented, which also is closer to reality, as the resistivity of the material can't be higher than that of the normal state.

One simple way to deal with the divergence of the electric field is to incorporate normal state resistivity, e.g. just by making it so, that the resistivity of the material becomes that of the normal state once, the resistivity that is determined by the *E-J* law exceeds it. This is illustrated in Figure 2.17 by the arrow next to the dashed line. This can be implemented in COMSOL with a helper boolean variable:

$$state = E_0\left(\frac{J}{J_c}\right)^n > \rho_{FL} * J \tag{2.17}$$

where ρ_{FL} is the resistivity of the superconductor in the flux liquid state and was taken to be 3.5×10^{-6} Ω m from [124]. *state* variable determines in which region the sample is in, i.e. if state equals 1 (true) then the sample is in the normal regime and linear resistivity is applied and if state = 0 (false), *E-J* law is applied as such:

$$E = E_0\left(\frac{J}{J_c}\right)^n (1 - state) + \rho_{FL} * J * state \tag{2.18}$$

This method has a drawback, that the derivative of electric field with respect to the current is not continuous which can lead non-convergence issues during solving, especially for large time steps. The smoothing of this transition can be achieved by adding the two contributions to the overall resistance "in parallel" as described by Duron et. al. [124], and shown in equation

$$E = J\left[\left(E_0\frac{J^{n-1}}{J_c^n}+\rho_0\right)^{-1}+\frac{1}{\rho_{FL}}\right]^{-1} \tag{2.19}$$

Where $\rho_0 = 3.5 \times 10^{-14}$ Ω m is the residual resistivity to prevent division by zero, but does not affect numerical results. However, the ρ_{FL} must be known before fitting the E-J law, or alternatively, data, well above J_c must be collected to fit the ρ_{FL} as well. Because if the (2.19) is applied after the simple power-law was fitted and J_c and n-values obtained (as usually the case for data provided by HTS tape manufacturers), then the equation (2.19) would then result in softer transition than intended as shown in Figure 2.17 using blue line. In that case, the first method, even though not as numerically robust, may give more accurate results, if currents substantially higher than J_c are involved ($J > 1.5J_c$).

However, when considering coated conductors which have conductive substrate and stabilisation, the linear resistive region is reached at even lower overcurrent, and the resulting resistivity is lower. This is due to current sharing between the superconductor, substrate and stabilisation. A thin strip (1.25 mm wide) of copper stabilised (RE)BCO tape described in detail 2.2.3.6 was characterised to currents of $2I_c$ in liquid nitrogen and the results are shown in Figure 2.18. The Figure 2.18a indicates that the sample has a linear resistivity from about 1.3-1.4 of I_c. By considering the cross-section of the sample, the resistivity value obtained was

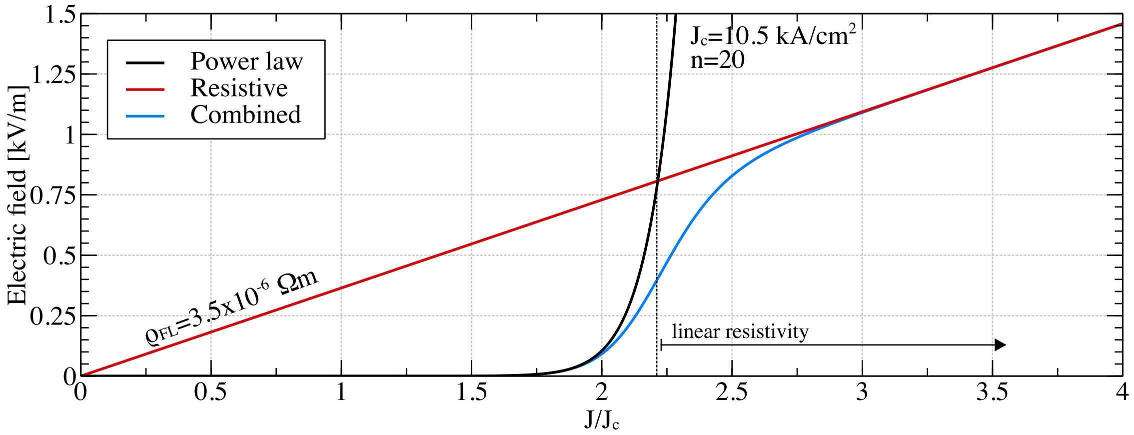

Figure 2.17– Modified E-J law showing linear resistivity for large overcritical currents.

1.77×10^{-8} Ω m which is very close to the value expected for the composite of Hastelloy, silver and copper at 77 K. The log linear plot of the same data shows the current range where the power law is valid (due to large span of electric field magnitudes, the precision of the measurement is only 0.1 µV). The critical current of the sample was found to be 26.6 A with an *n*-value of 26.9. As before, during magnetisation experiments, the current rarely exceed $1.3J_c$ during magnetisation simulations in this work. However, it may be relevant for higher magnetic field pulses with higher ramp rates d*B*/d*t*. Also, for tape without copper stabilisation, the crossover to linear regime is expected to occur at higher J/J_c due to higher resistivity of the tape. To conclude, implementation of the resistive portion of the *E-J* curve helps the numerical convergence, but the simulation results are not altered significantly.

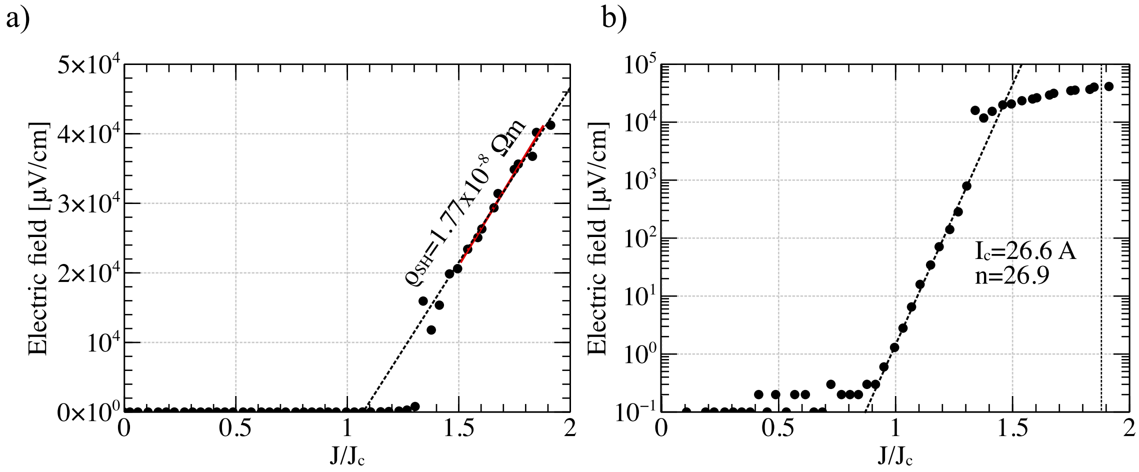

Figure 2.18– Electric field as a function of J/J_c for a (RE)BCO tape showing a cross-over to linear resistivity at ~$1.35J_c$, the resistivity matches that of the substrate/stabilisation composite. Graph b) shows the same data on a logarithmic scale indicating the critical current and the *n*-value.

2.6.3 Parameters used in the simulations

Constants used in the equations in the previous section and thermal properties used are summarised in Table 2.1. Most of the sample parameters are: temperature and/or magnetic field dependant. In cases where other values are used, it will be indicated in the appropriate chapters.

Table 2.1 – Simulation parameters and material data.

Parameter	Description	Value
T_c	Critical temperature of YBCO	92 K
T_0	Equilibrium temperature of sample	Simulation dependant
B_0	Flux density constant in equation	1.3 T
a	Constant in equation (2.6)	Matched to sample performance
E_0	Electric field constant in eq. (2.7)	1×10^{-4} V m^{-1}
n	n-value in equation (2.7)	Sample, temp. and field dependant
B_a	Applied pulsed field amplitude, eq. (2.15)	Simulation dependant
Q_c	Cooling power, eq. (2.16)	2 W K^{-1}
ρ_{YBCO}	Density of YBCO	5.9×10^{3} Kg m^{-3}
ρ_{Cu}	Density of copper	8.96×10^{3} Kg m^{-3}
$k_{ab}(T)$	Thermal conductivity of YBCO in ab-plane	[74] (20 W m^{-1} K^{-1} at 40 K)
$k_c(T)$	Thermal conductivity of YBCO along c-axis	[74] (4 W m^{-1} K^{-1} at 40 K)
$C(T)$	Thermal capacity of YBCO	[74] (132 J kg^{-1} K^{-1} at 40 K)
$k_{Cu}(T)$	Thermal conductivity of copper, RRR=30	[125] (930 W m^{-1}K^{-1} at 40 K)
$C_{Cu}(T)$	Thermal capacity of copper	[125] (57 J kg^{-1} K^{-1} at 40 K)
$\sigma_{Cu}(T)$	Electrical conductivity of copper, RRR=30	[125] (1.44×10^{9} S m^{-1} at 40 K)
$\rho_{Hast.}$	Density of Hastelloy	[126] 8.89×10^{3} Kg m^{-3}
$k_{Hast.}(T)$	Thermal conductivity of Hastelloy	[126] (6.42 W m^{-1} K^{-1} at 40 K)
$C_{Hast.}(T)$	Thermal capacity of Hastelloy	[126] (40 J kg^{-1} K^{-1} at 40 K)
$\sigma_{Hast.}(T)$	Electrical conductivity of Hastelloy	[126] (8.12×10^{5} S m^{-1} at 40 K)
ρ_{Ag}	Density of silver	[127] 10.49×10^{3} Kg m^{-3}
$k_{Ag}(T)$	Thermal conductivity of silver	[127] (800 W m^{-1} K^{-1} at 40 K)
$C_{Ag}(T)$	Thermal capacity of silver	[127] (78 J kg^{-1} K^{-1} at 40 K)
$\sigma_{Ag}(T)$	Electrical conductivity of silver	[127] (1.67×10^{9} S m^{-1} at 40 K)
ρ_{PbSn}	Density of PbSn solder	[125] 8.40×10^{3} Kg m^{-3}
$k_{PbSn}(T)$	Thermal conductivity of PbSn solder	[125] (36.1 W m^{-1} K^{-1} at 40 K)
$C_{PbSn}(T)$	Thermal capacity of PbSn solder	[125] (19.8 J kg^{-1} K^{-1} at 40 K)
$\sigma_{PbSn}(T)$	Electrical conductivity of PbSn solder	[125] (7.73×10^{7} S m^{-1} at 40 K)
$\rho_{Styc.}$	Density of Stycast 2850 FT	2.4×10^{3} Kg m^{-3}
$k_{Styc.}(T)$	Thermal conductivity of Stycast 2850 FT	[128] (0.6 W m^{-1} K^{-1} at 40 K extrp.)
$C_{Styc.}(T)$	Thermal capacity of Stycast 2850 FT	[128] (61 J kg^{-1} K^{-1} at 40 K)

Chapter 3 Additional thermal stabilisation for effective heat removal during PFM

As detailed in section 1.4.4, there is significant heat generation involved during pulsed field magnetisation, which in turn limits the trapped field to well below the maximum trapped field that can be achieved by field cooling. It is therefore beneficial to reduce the maximum temperature rise and quickly lower the temperature back to the target temperature to reduce flux creep subsequent to magnetisation. Given the low thermal conductivity of (RE)BCO and very short timescale of the pulsed field (10-100 ms), the process is almost adiabatic, however some improvements can be made by embedding thermally conductive materials within (RE)BCO bulk superconductors as discussed in a previous publication (see Figure 1.31, [76]). However, it is likely that this embedded copper only affects the material in the immediate vicinity to it, and not the bulk of the material. The situation, however is different for stacks of HTS coated conductors, as the thin (RE)BCO layer is in intimate contact with silver and copper stabilizers, which have high thermal conductivity and can effectively redistribute thermal energy, as described in previous publication [129]. The thermally conductive layers, can in principle be coupled to a larger heat-sink to lower the maximum temperature during pulsed field magnetization. It is expected that the thermal contact between the (RE)BCO stack and any heat-sink is of considerable importance. To improve this, (RE)BCO tapes can be soldered directly to the heat-sink, which is especially convenient given that solder coated tape is available directly from coated conductor manufacturers. Soldering the tape layers together gives the additional advantage of making the tape layers a self-supporting object and gives some additional protection form environmental degradation. Section 3.1.2, investigates the soldering procedure of the stack layers to determine if the elevated temperatures required have a damaging effect on the superconducting properties of the tape. Subsequently, FEM modelling was performed to determine possible improvements by using a thermally conductive sleeve around a tape stack. The idea was tested using a 20-layer sample before and after soldering it to a copper coldhead.

3.1 Soldering of HTS tape stacks

To test the feasibility of soldering the HTS stacks using solder, a stack of 5 HTS tape layers was soldered and the trapped field profile was measured before and after the soldering procedure. Moreover, two samples of a single layer of solder coated tape were given the same heat treatment as for the stack of 5 layers. The critical current was measured before and after the heat treatment to determine if there was any degradation.

3.1.1 HTS tape used

The superconducting tape used in the experiments was developed and supplied by SuperOx. In addition to the conventional IBAD architecture, the tape used for soldering experiments was coated with 5 μm of Cu and 10 μm of Pb-Sn eutectic solder (melting point 183 °C) as illustrated in Figure 3.1. The tape supplied was 12 mm wide and had a critical current rating of at least 400 A at self-field and 77 K. The solder coated tape was cut to 12 mm squares and assembled into a stack of required size. All tape layers were kept in the same orientation, i.e. the (RE)BCO coated side was kept pointing upwards and the tape edges that were cut were also aligned in a single direction.

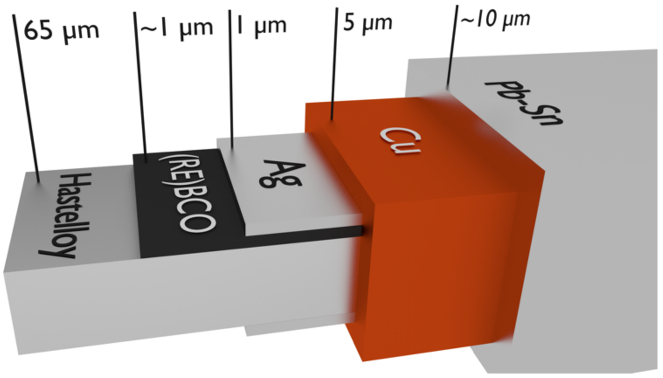

Figure 3.1– Simplified schematic representation of the layers in HTS tape used in this work (buffer stack omitted).

3.1.2 Soldering procedure and its effects on superconducting properties

The stack was compressed using a setup shown in Figure 3.2a and two heat treatments were carried out with peak temperatures in the range of 200-210 ºC, chosen to be slightly higher than the melting point of the Pb-Sn solder used. A compressive force of about 5 N was applied to expel excess solder from the stack, increasing the engineering critical current density of the stack. This setup was successfully used to solder stacks up to 12 mm × 120 mm in size [130]. Heat treatments were carried out in air and two different temperature profiles were tried (see Figure 3.2b). Heat treatment HT1 was performed by placing the compression setup in a box furnace with a preprogramed temperature profile. More details of the results obtained from this heat treatment, can be found in [131]. It was found that the heat treatment resulted in a slight degradation of superconducting properties, the trapped field in a 5-layer stack after soldering was reduced by 9.3±4.7%. The trapped field profile showed a uniform decrease in trapped field, rather than indicating any localized defect formation. It is also worth noting that after the heat treatment, the height of the stacks decreased by up to 12%. Indicating that over half, 56% of the Pb-Sn solder initially present was expelled from between the layers. Following initial success, two more 100-layer stacks were manufactured for further testing using pulsed field magnetization and field cooling described in Chapter 6.

In order to minimize degradation of the superconducting properties during soldering, an alternative soldering procedure was performed trying to minimize time spent at elevated temperatures. Heat treatment HT2 in Figure 3.2b) was performed by placing the compression

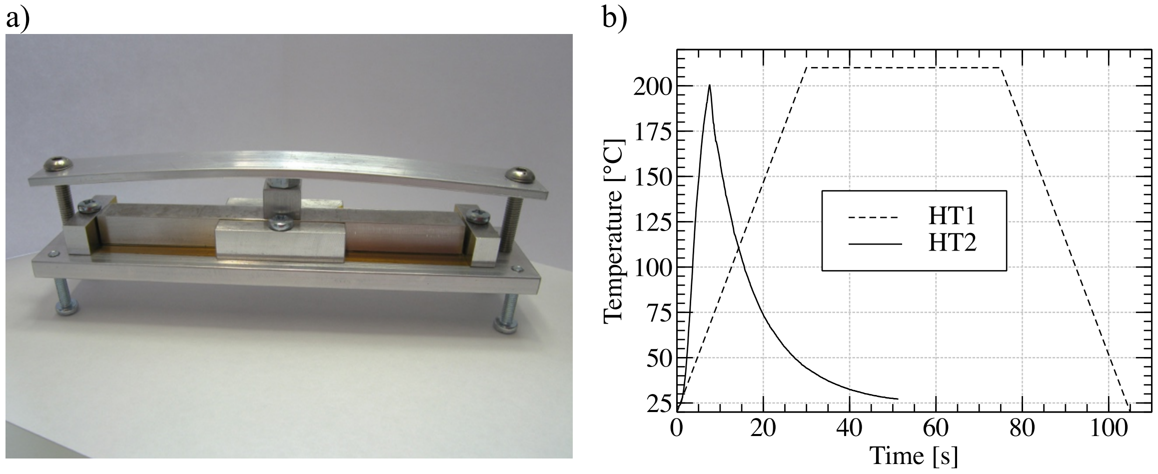

Figure 3.2– a) setup for compressing the tape layers, with the top Al bar used to apply compressive stress; b) temperature profiles for two different heat treatments tried.

rig on a hotplate, as the temperature of the hotplate was ramped as quickly as possible, after the tape reached a temperature of ~200 ºC the sample was removed from the hotplate and allowed to air-cool. The temperature of the sample was recorded by a thermocouple inserted directly into the aluminium block that the tape is resting on. The Hall probe magnetometry did not show any (within experimental error) degradation in the maximum trapped field after the soldering procedure (see Figure 3.3).

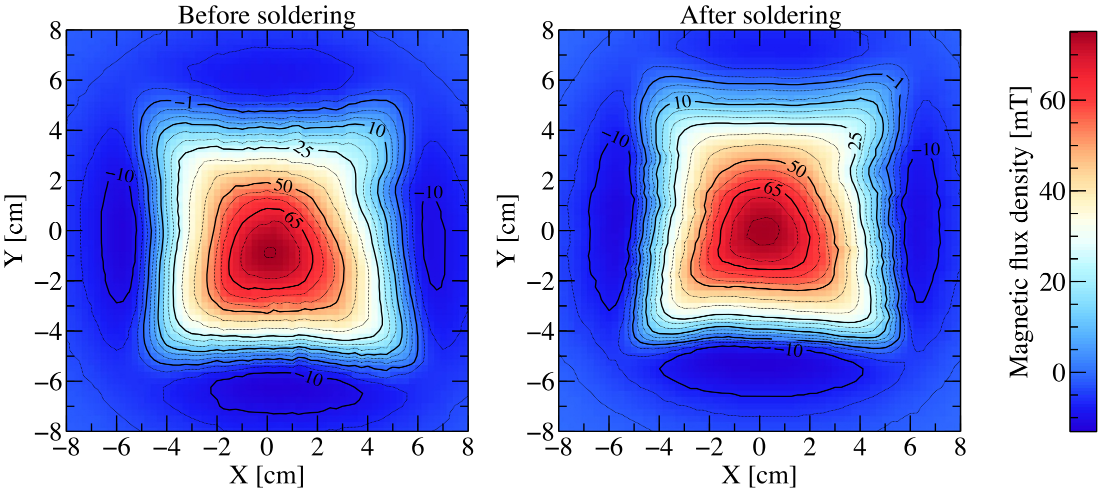

Figure 3.3– Trapped field profiles after field cooling of a 5-layer stack before and after soldering. The field is measured 0.9 mm above the sample surface.

Given substantial uncertainty of the Hall scan measurement ~5% due to scan height determination, critical current measurements of a single layer of tape before and after heat treatment equivalent to HT2 were performed. The critical current measurement setup was detailed in section 2.2. Given that the measurement does not require soldering of the tape to current leads and the voltage taps are provided by pogo-pins, the measurement should have minimal uncertainty. The results show a decrease from 457.2 A (*n*-value 33.6) to 454.9 A (*n*-value 34.7). This constitutes a reduction of only 0.5±0.1%. This is consistent with other recent data on thermal degradation of commercial superconducting tape [132].

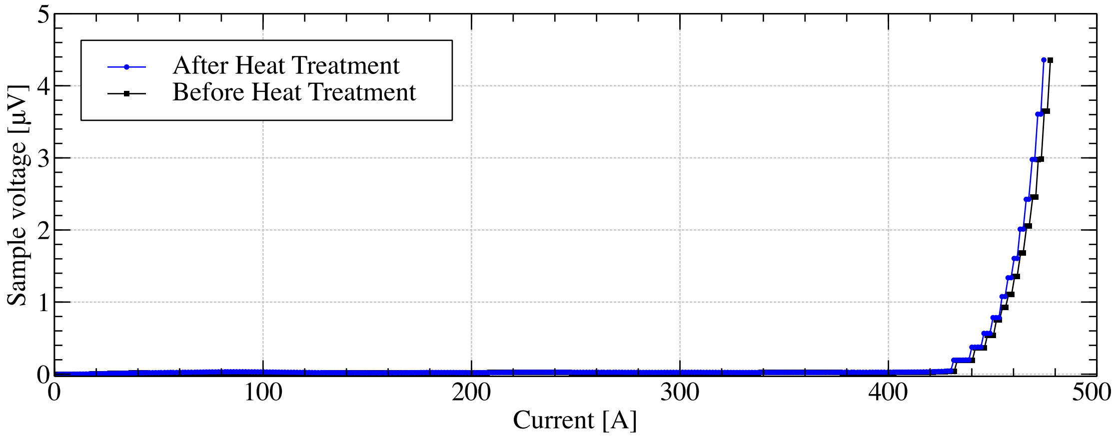

Figure 3.4– Critical current before and after heat-treatment of the HTS tape equivalent to the soldering procedure, showing degradation of 0.5±0.1% in critical current.

Each layer is coated with the solder, which ensures a good bond between each layer. Conversely, if epoxy resin is used, one relies on resin penetration between each layer, which can be difficult to ensure once the stack is already assembled and compressed. The pre-applied solder also ensures that the spacing between layers is more uniform. Figure 3.5a shows a side view of the soldered stack showing a layered structure with uniform spacing.

Bonding strength is still to be determined via mechanical testing, however preliminary testing via the T-peel technique shows indications that the strength is not limited by the solder but the Hastelloy-silver interface on the backside of the HTS tape as shown in Figure 3.5b.

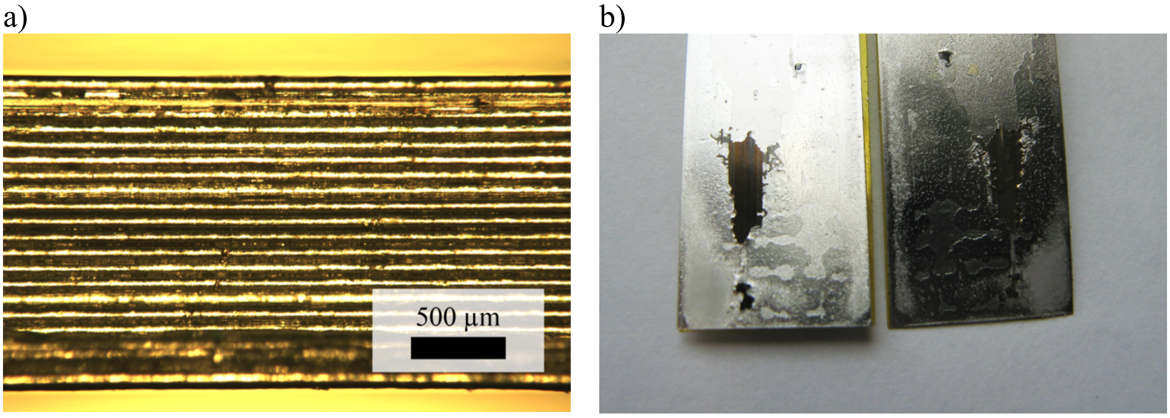

Figure 3.5– a) Side view of the soldered stack showing very uniform arrangement; b) First qualitative mechanical tests indicate that the backside (left), opposite to (RE)BCO, may be the limiting factor for delamination strength.

3.2 Results for 20-layer stack

A 20-layer stack was soldered to a copper sleeve depicted in Figure 3.6a according to the procedure outlined in the previous section 3.1. It was decided to add thermal mass around the exterior of the stack, as opposed to the beneath the stack, due to much higher thermal conductivity along the tape layers than in the direction between the layers. The thermal conductivity in between the layers is limited by the low thermal conductivity of Hastelloy substrate (see Table 1.1), whilst along the layers the thermal conductivity is enhanced by the highly conductive silver over-layer and copper stabilisation. Moreover, the heating is most pronounced at the periphery of the sample, where the flux enters and leaves the sample. For the tape tested, the thermal conductivity, determined from thicknesses of the individual Hastelloy, (RE)BCO, silver, copper and solder layers is ~7 W/(m K) across the layers and ~210 W/(m K) along the layers at 30 K. We can then calculate the thermal diffusivity along the two directions and make a back of the envelope estimation the “diffusion distance” l, i.e. the distance at which the temperature profile may be affected after the pulse (~28 ms):

$$l = \sqrt{\frac{k}{\rho \, C_p} t} \tag{3.1}$$

where k, ρ, C_p, t are thermal conductivity, density, heat capacity and time accordingly. The heat diffusion distances come out as ~1 mm across the layers and ~5 mm along the layers of the HTS tape. This suggests that, for a stack of 12 mm width, a significant portion of the stack will be affected by the presence of a thermal mass on the periphery, however a thermal mass below, would only affect stacks less than several mm thick.

The copper surround was made with a deliberate gap in the perimeter to limit eddy current heating within the copper. The interior of the sleeve was made slightly larger than the size of square tape layers (12.5 mm vs. 12 mm) and the thickness of the sleeve was 1.5 mm. Thermal contact between tape layers and the copper sleeve is ensured by solder or resin as discussed below. The height of the sleeve was kept at 8 mm, whilst the height of the 20-layer stack was only 1.65 mm. The performance of the stack soldered to the sleeve was compared to the same set of layers before soldering and without the copper sleeve. Single pulse magnetisation was performed at 30 and 15 K, as thermal heating is most significant at low temperatures.

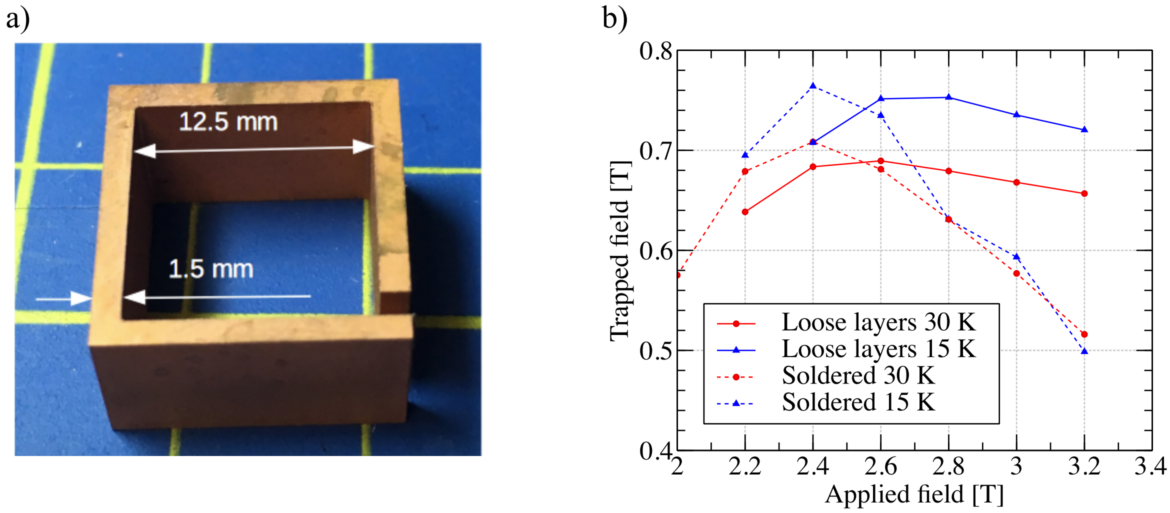

Figure 3.6– a) copper sleeve used in experiments for heat-sinking; b) Single pulse magnetisation results for staked layers of tape (before soldering) at 30 and 15 K and comparison to the same sample after soldering them together to a copper sleeve depicted in a)

Figure 3.4b shows the results and unfortunately, the trapped field is not enhanced significantly. However, the shift in applied field for trapping maximum field values towards lower fields and much lower trapped field at high applied fields seems to indicate that some benefit from heat extraction from the periphery of the sample is present at low applied field, but the opposite is true at high applied fields. This is likely due to eddy current heating within the sleeve itself. 3D simulation of the copper sleeve in isolation indicates that the temperature rise during the pulse is significant, but lower than that of the stack itself (see Figure 3.5a solid lines). Thus, some improvement in trapped field is expected. However, given the stack is electrically conducting, the current can go around the copper sleeve via the HTS tape and solder. To fully analyse the heating in the copper sleeve, a 3D model incorporating the superconducting stack is required to replicate the geometry of the problem. While this is achievable, computational time for a 3D model incorporating superconductivity and heat transfer is high. In order to reduce computing time, a simplified 3D model, using the average electrical conductivity of the stack in its resistive state was used to estimate the heating power generated in the sleeve. This heating power and its variation during the pulse duration was then used in the 2D axis-symmetric model. The temperature rise in the sleeve for this case is shown Figure 3.7a with dashed lines. The figure illustrates that the copper sleeve can't be considered in isolation and that eddy current heating becomes a problem that must be addressed.

As a solution, two approaches were considered:

- further segmentation of the coldhead, e.g. into 4 separate segments attached to the four sides of the stack (see Figure 3.5b);
- using electrically insulating bonding material between the stack and the copper sleeve (Stycast 2850 FT resin).

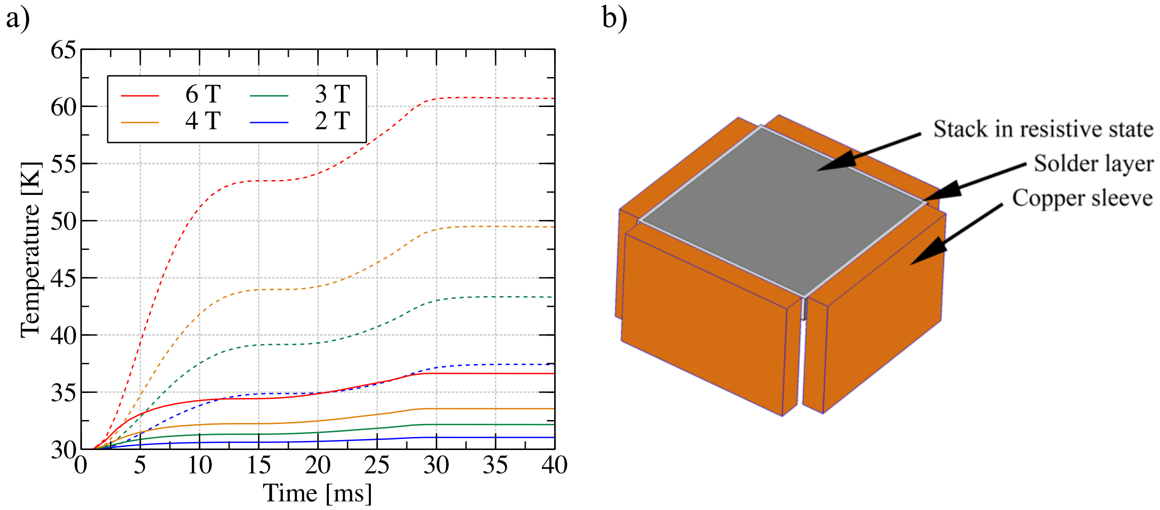

Figure 3.7– a) simulated temperature rise in the copper sleeve exposed to magnetic field pulses of different magnitudes at 30 K without (solid lines) and with (dashed lines) the HTS tape stack in the sleeve; b) further subdivision of the copper sleeve to reduce eddy current heating.

Modelling results showing how the different configurations considered affect the trapped field after single pulse magnetisation are summarised in Figure 3.8. The simulation results for the bare stack (without a coldhead) match the measurements shown Figure 3.4b well. Similarly, the trapped field is not increased after introduction of a copper sleeve if the eddy current heating is considered. Although the trapped field dependence on applied field does not show the same features, due to approximations employed for calculating the case where the stack and the copper sleeve are electrically connected. Nevertheless, the model shows that improvement is not likely if eddy current heating in the sleeve is not reduced.

On the other hand, series “w sleeve/no eddys” shows the trapped field if the heating in the copper sheath could be neglected altogether. An improvement of up to 33% can be expected. If heating in an electrically isolated copper sheath is considered, the improvement is not reduced greatly, but to achieve electrical insulation, an electrically insulating fixture, like Stycast resin is used. Such resin has significantly lower thermal conductivity than solder and increases the thermal resistance between the stack and the copper sleeve. The model shows that the improvement drops to 9% only, even considering that Stycast layer surrounding the stack is just 0.25 mm thick. Therefore, a further subdivision of the copper sleeve, while maintaining soldered contact between the stack and the sleeve, shows highest promise with potential improvement of up to 24%.

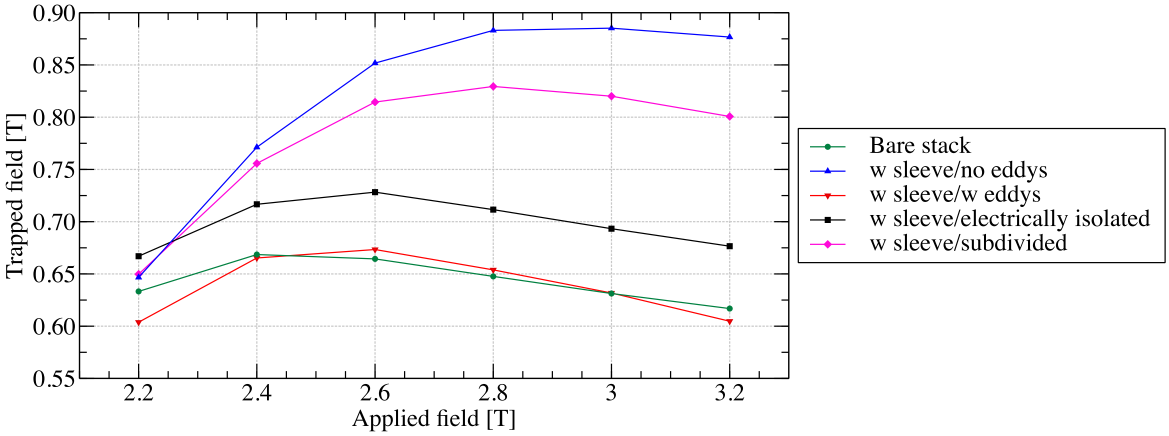

Figure 3.8– Modelling results showing the potential improvement by using a thermally conductive copper sleeve in various configurations.

The already soldered sample was modified to subdivide the copper sleeve into 4 separate parts and was re-tested. The results for both single pulse and multi-pulse magnetisation at 30 K are summarised in Figure 3.9. As predicted by the modelling, the modified sleeve performed much better, which is especially evident at applied fields over 3 T. The copper sleeve improved the

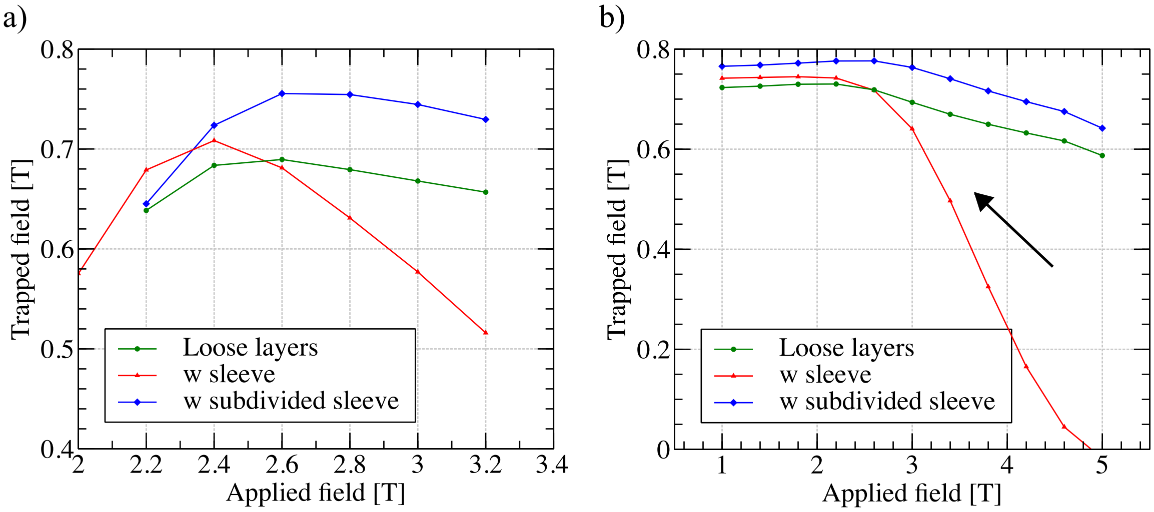

Figure 3.9– Measured trapped field for loose layers, sample soldered to the copper sleeve in Figure 3.6a and the same after subdivision of the sleeve into 4 segments after a) single pulse magnetisation and b) multi-pulse magnetisation, the arrow indicates that the pulses were applied in the order of decreasing amplitude.

performance by 10% compared to the loose layers. This is lower than modelled, again, most likely due to the assumptions in the model discussed above. A similar improvement of 8% was also observed for the maximum trapped field using multi-pulse IMRA. It is interesting to note that the copper sleeve without subdivisions was heated to such extent that the tape stack was unable to trap any field at an applied field of 5 T, however it still provided improvement over loose layers, due to added thermal mass at low applied fields.

3.3 Conclusions

The thermally conductive sleeve was successfully used to increase the trapped field after PFM. The results were not as high as initially anticipated from simulations due to simplifications made in the modelling, however, the improvement in trapped field by 10% was achieved by using non-superconductive, thermally conductive copper sleeve.

Due to the metallic nature of the stacked tape, the layers of the tape can be soldered directly to thermally conductive structures to remove heat. Furthermore, due to much higher thermal conductivity of the HTS tape as compared to the (RE)BCO bulk, the thermal diffusivity is much higher, allowing some heat redistribution even during the duration of the applied magnetic pulse, however, this effect is expected to be greater when using magnetic pulses of longer duration, as discussed later in section 4.8.

However, the metallic nature of the HTS tape also mean that eddy currents induced during the magnetic pulse cause more heating as the tape itself can bridge the eddy current between subdivided segments of the electrically conductive additions. Hence, care should be taken to avoid eddy current heating. Modelling has shown that using Stycast to electrically insulate the sleeve from the stack, drastically reduces the positive effect due to low thermal conductivity of the resin. For this reason, additional subdivision of the copper sleeve was tried instead. The Eddy currents are expected in the silver and copper stabilisation as well, but due to very small thicknesses, it only contributes less than 1% to heat generated within the (RE)BCO itself [129]. It is worth noting that using copper to enhance trapped field may not be suitable for rotating machines, due to component of AC magnetic field experienced by the trapped field magnet (discussed in section 1.4.5.2), which would introduce heating during operation (not only magnetisation) and would contribute to cryogenic load. However, other materials such as sapphire (Al_2O_3) have exceptional thermal conductivity in the temperature range 20-40 K ~1000 W/(m K) [133] while being electrically insulating. Sapphire, however presents issues for making good thermal contact, and has relatively low thermal capacity.

Lastly, the sample tested in this study was relatively small, however the heating, and thus the associated problems, are more significant for large samples. Hence the potential improvements are expected to be higher for larger samples.

Chapter 4 Optimization of pulsed field sequence for pulsed field magnetisation

It is well known that for pulsed field magnetisation (PFM), applying of multiple pulses can lead to higher trapped fields and flux within the sample as opposed to a single pulse (see section 1.4.4), even if the single pulse magnitude is optimised. However, the number of variables to optimise the magnetisation sequence increases, as instead of just optimising the magnitude of applied field, one needs to consider the number of pulses to apply, the starting field to begin the sequence with and also the change in subsequent pulsed field magnitudes. This leads to a large number of strategies to explore. In this work, we chose to investigate sequences with monotonically decreasing applied field magnitude at constant temperature, the so called IMRA sequence (iterative magnetisation with reducing amplitudes), to determine the effect of starting field and step in applied field magnitude on the final trapped field and flux after the end of the sequence. Pulse magnetisation was performed at 30 K and 60 K to investigate the effect of temperature. This work was done in collaboration with Shengnan Zou and Dr Francesco Grilli from Karlsruhe Institute of Technology, Germany. I have done experimental work, whist the FEM modelling was done by the collaborators. Part of this work is presented in a publication [134].

4.1 Samples and experimental setup

Superconducting tape used for this work was produced by SuperPower Inc. to specification SP12050 AP, i.e. $(Y,Gd)_{1+x}Ba_2Cu_3O_{7-\delta}$ with 7.5% of Zr added. The stated $I_{c,min}$ was 240 A, at 77 K and self-field, over the whole length of the tape. However, segments tested showed much higher I_c, as shown in section 5.1.2. The tape was 12 mm wide with a 50 µm thick Hastelloy substrate and a 2 µm thickness silver overlayer. The overall thickness of the tape was ~55 µm. The tape was cut to 12×12 mm square pieces to make a stack. A 20-layer stack was assembled into a non-magnetic stainless steel sample holder illustrated in Figure 4.1. The stack was compressed inside the pulse magnetisation system described in 2.4.

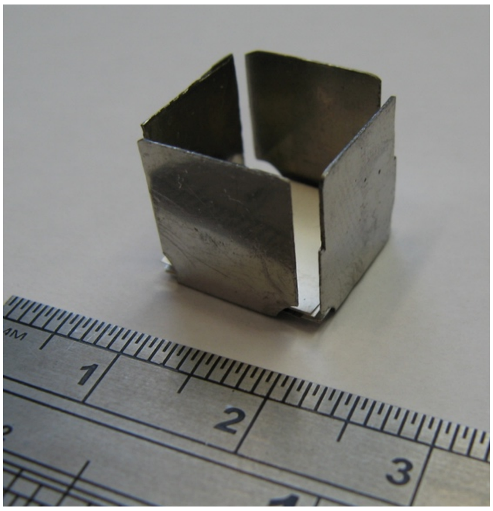

Figure 4.1– Sample holder for stacks of tape, made of non-magnetic stainless steel 316, wall thickness is 0.32 mm

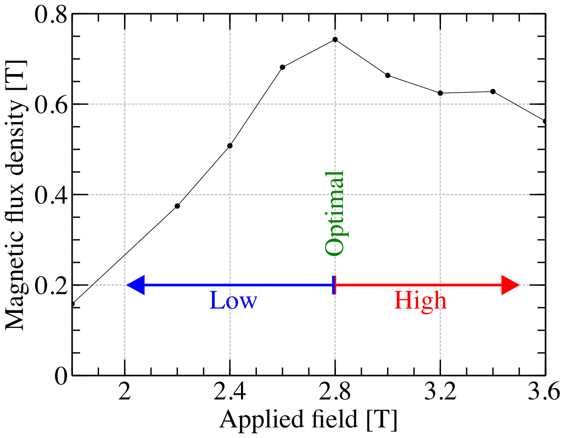

Figure 4.2– Single pulse magnetisation results, defining terms low (sub-optimal), high and optimal field for further discussion.

Each pulse magnetisation sequence was delivered after the desired temperature was reached. After the sequence the sample temperature was raised to 95 K, above the critical temperature, before starting a new sequence to eliminate any “memory” of the previous magnetisation state. This was achieved with a Kanthal resistive wire heater around the sample holder, allowing to try multiple magnetisation sequences without warming up the whole system. Sample was not removed from the system at any point to eliminate errors due to sample positioning and several attempts of a single magnetisation sequence were performed in separate days to confirm reproducibility.

4.2 Single pulse magnetisation

To aid discussion on different pulse sequences for multi-pulse magnetisation it is worth having an example data for single-pulse magnetisation, as it gives insight at what pulse magnitudes are too low to fully penetrate the sample, and what fields are too high and cause excessive heating. Figure 4.2 shows the data for single pulse magnetisation and defines pulse magnitude ranges as sub-optimal, optimal and high for further discussion.

4.3 Effect of the first pulse in the sequence

By considering the principles of the IMRA magnetization technique, the first pulses should be high in magnitude, so that the magnetic field penetrates and induces currents in the centre of the sample as subsequent pulses only increase the current density closer to the edges of the sample. However, exceeding some threshold field, or applying a field larger than necessary to penetrate to the centre of the sample, results in lower trapped field after that pulse as larger fields lead to more heat being produced. However, the field required to penetrate the sample is not known a priori in most cases. Thus, it is relevant to find out whether starting with higher than necessary pulsed field impacts the final field at the end of the pulsed field magnetisation sequence.

Figure 4.3 shows the trapped field and flux during the pulse sequence. Sequences with different start fields were investigated, namely 3, 5, 7 and 7.8 T and the field was decreased by 0.4 T for each successive pulse until 0.6 T was reached. The final field above the centre of the sample, as expected, varies only slightly for sequences starting with more than 5 T, indicating that that is enough to penetrate the sample. But interestingly, a pulse of 5 or 7 T is not sufficient

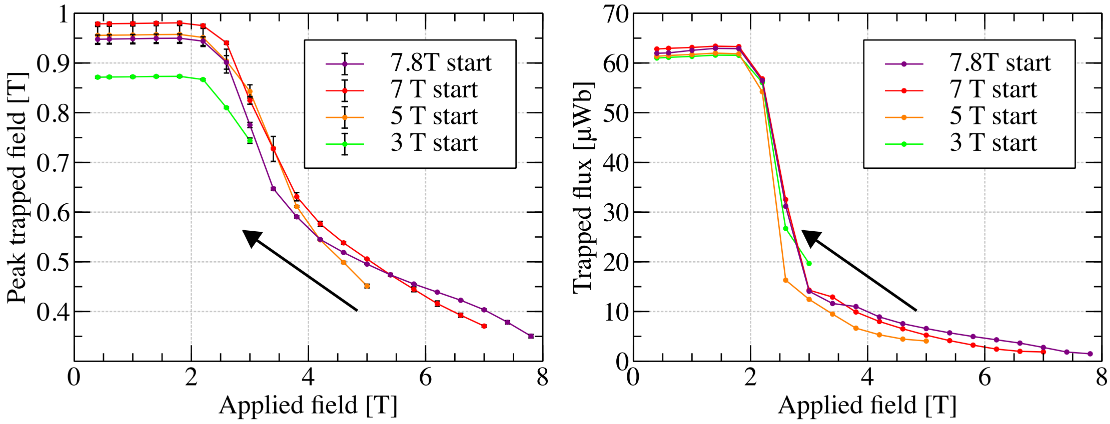

Figure 4.3– Magnetic flux density 0.8 mm above the centre of the stack after each sequence (left) and trapped flux 0.8 mm above the sample and integrated over the surface of the sample (right) for PFM sequences (at 30 K) with different initial starting field, but identical field decrement between successive pulses. The arrows indicate that applied pulse magnitude is progressively decreased in each sequence.

to override the previous “magnetic history” of the sample. We can see that the trapped field even after large 7 T pulse is different for sequences starting with 7 and 7.8 T. The trapped field increases most rapidly in the region between 4-2.5 T, where the trade-off between sample heating and applied field magnitude is most optimal.

Each sequence was repeated three times, and the standard deviation in the mean is represented by the error bars on the plot of peak trapped field. It is worth noting that, the trapped fields are perfectly reproducible when applied fields is > 4 T, however, we start to see some variability when applied field is below 4 T, which then also translates to variation in the final trapped field. This variation can be attributed to flux jumps during the pulse (discussed in section 4.5). With the limited dataset available, the final trapped field increased when the magnetisation was started at higher field, except for the 7.8 T sequence which breaks this trend, and resulted in a lower trapped field then the sequence started with a 5 T pulse.

The trapped flux integrated above the surface of the sample, varies much less than the peak trapped field for the different sequences, as it is dominated by the flux density at the edges of the sample (larger relative area), than the peak field at the centre. And the flux density at the periphery is enhanced only at relatively low magnitude < 3 T pulses. This is illustrated in the right-hand side of Figure 4.3, showing a very rapid increase in trapped flux at fields below 3 T.

4.4 Effect of applied field decrement between pulses

Similarly, sequences with the same initial applied field (7 T), but different increments between successive pulses (0.8 T, 0.4 T and 0.2 T) were tested. The results are summarised in Figure 4.4. Conclusions are similar to those in the previous section. The higher number of pulses generally results in higher final trapped field, but only up to a point, as the higher number of pulses also lead to flux jumps and variability between experimental runs employing the same sequence. With the higher number of applied pulses, each pulse optimises the current density at a particular distance from the periphery of the sample, leading to higher trapped field, however this results in high number of layers of alternating positive and negative current density as shown by simulations (see section 4.7). This arrangement is less stable and potentially can lead to collapse of the trapped field via a flux jump.

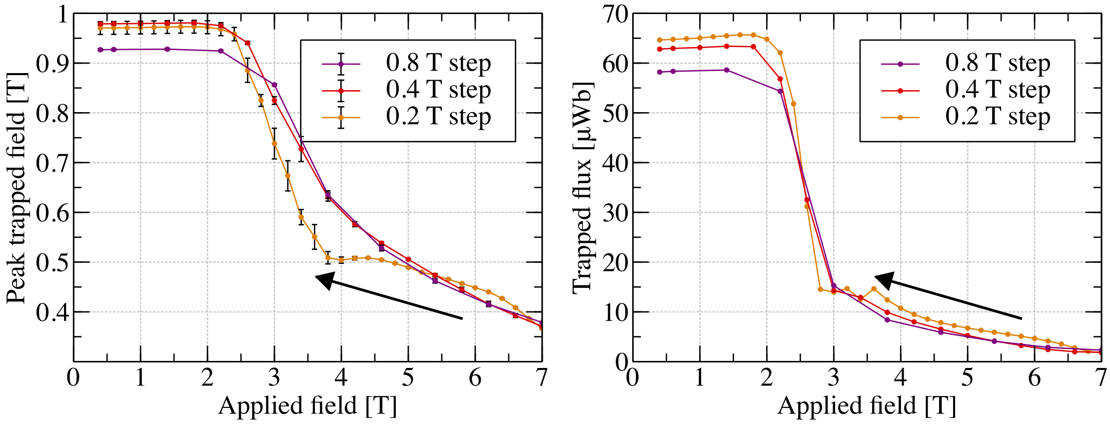

Figure 4.4– Magnetic flux density 0.8 mm above the centre of the stack after each sequence (left) and trapped flux 0.8 mm above the sample and integrated over the surface of the sample (right) for PFM sequences (at 30 K) with the same initial field, but different field decrement between successive pulses. The arrows indicate that applied pulse magnitude is progressively decreased in each sequence.

In this case, it can be seen that, there is significant variability of trapped field in the range below 4 T for sequence with 0.2 T steps. One difference is that, sequences with smaller field steps have more pulses in the low fields < 3 T, which is beneficial for enhancing trapped flux. However, it is worth noting that pulses below 2 T only acted to decrease the trapped field and flux, as the pulses are too low in magnitude and only act to heat up the sample slightly. Figure 4.5 shows the derivative of trapped flux and field with respect to applied field. It can be seen that the trapped field starts increasing first, followed by the increase in trapped flux, as the smaller applied fields increase the flux density in the periphery of the sample only.

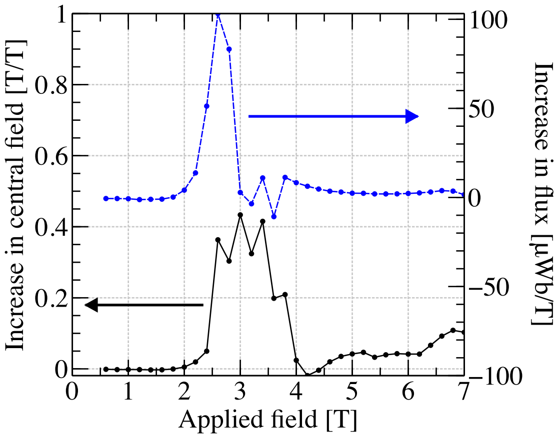

Figure 4.5– Derivative of trapped peak field and flux for a sequence with 0.2 T applied field steps, showing that the peak field increases first, and trapped flux significantly increases at slightly lower applied fields.

4.5 Effect of temperature

In the above sections the PFM was performed at 30 K. At this temperature, the heat capacity of most materials is low, and thermal flux avalanches due to thermal heating are common. And whilst flux jumps on the rising edge of the applied pulse can be beneficial as in the case outlined in section 1.4.4.2, the pulse shape in the experimental system used, has a steep falling edge as well, which results in flux jumps that reduce the trapped field magnitude. A rapid decrease in measured flux density at the centre of the sample (see Figure 4.6) was observed during the pulse at 30 K, but not at 60 K. The figure shows the measured magnetic flux density for exactly the same pulse sequence (namely, 5 T starting field and 0.4 T decrement, during the 3 T pulse) for the same sample, two identical runs at 30 K and one at 60 K. The flux jumps occurring at 30 K, happened at slightly different time during the pulse (outlined via arrows) and the trapped field just after the pulse turned out to be different, leading to the variability between the identical experimental runs, that was mentioned in the previous sections. On the other hand, no obvious flux jumps were observed at 60 K, as shown in Figure 4.6, where the magnetic flux density is a smooth curve. It is worth noting that the peak recorded field at 60 K appears larger due to fact that the critical current at 60 K is much lower than at 30 K, hence the sample shields

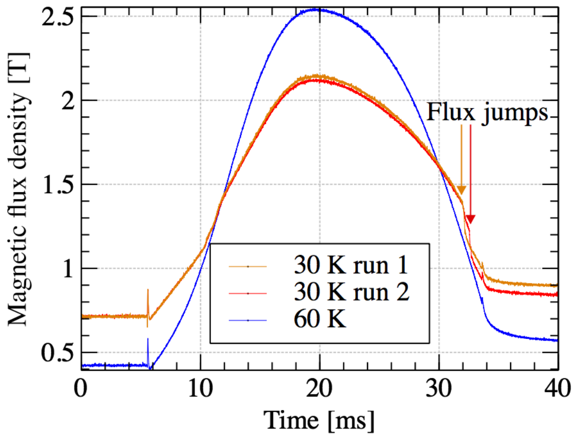

Figure 4.6– Magnetic flux density above the centre of the sample during a 3 T pulse in a sequence starting with 5 T and decrements of 0.4 T at 30 K and 60 K. Flux jumps at 30 K are shown with arrows.

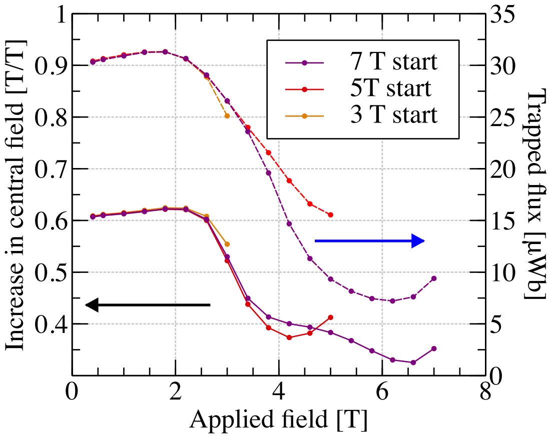

Figure 4.7– Magnetic flux density 0.8 mm above the centre of the stack after each sequence (left) and trapped flux 0.8 mm above the sample and integrated over the surface of the sample (right) for PFM sequences (at 60 K) with different initial starting field, but identical field decrement between successive pulses.

the applied field less effectively. Nevertheless, the applied field in each of the three curves, was indeed 3 T.

The high thermal stability at 60 K also means that the importance of optimising the pulse sequence is much less as shown in Figure 4.7. Each pulse results in much smaller temperature rise in the sample. All sequences, regardless the starting point, converge to the same peak field and flux above the sample.

4.6 Alternative sequences

Several other sequences were tried to confirm, that to obtain highest peak trapped field, the sequence benefits from smaller step sizes in the intermediate region 3.5-2.5 T (near optimal pulse magnitude for single pulse magnetisation), however that may lead to flux jumps, as is seen by irregular trapped field progression in the "Adaptive" sequence in Figure 4.8. The adaptive sequence has slightly higher trapped field than the regular 7/0.4 sequence, but the trapped flux is lower due to low number of pulses in the low field region of 2.5-2 T. Whilst the "Reverse" sequence, where the successive pulses are increasing in magnitude, reiterates the importance of first applying high pulsed field first to increase the central field, and then move towards the lower pulsed fields to add to the flux by enhancing trapped field at the periphery of the sample.

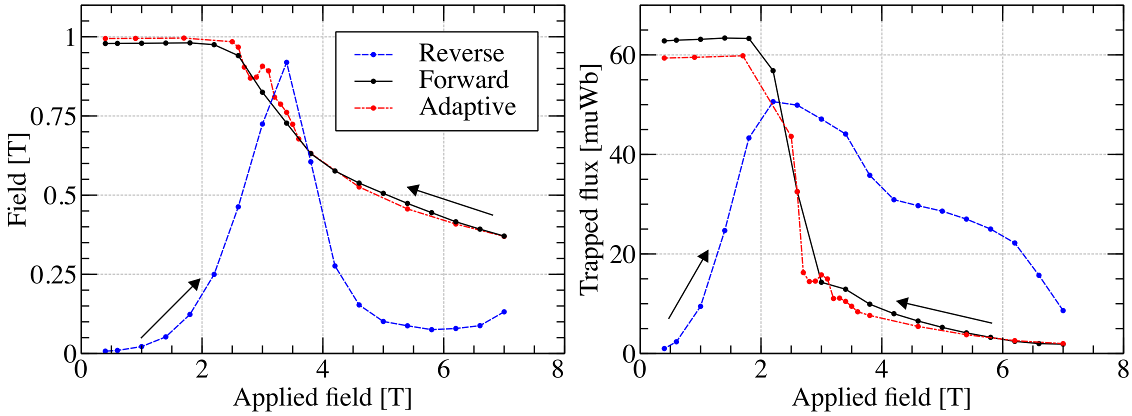

Figure 4.8– Trapped field and flux of regular 7/0.4 sequence at 30 K in comparison to the sequence with same applied fields but reverse order (see arrows) and a sequence with a small step only in the 3.5-2.5 T applied field range.

4.7 Comparison to modelling

FEM modelling of multi-pulse magnetisation was done by KIT during collaboration on optimisation of multi-pulse techniques resulting in publication [134]. The results will be briefly outlined to provide additional background.

The simulations were done using *H* formulation in COMSOL. The geometry was simplified to 2D-infinite, and only a quarter of the stack was simulated using symmetry considerations. Although, the modelled geometry was significantly simplified to reduce the computation time and investigate large number of sequences, the overall trends should be general, and they do indeed seem to mirror the conclusions from derived from experimental data. The sequences are denoted as *X/Y* where *X* is the starting field and *Y* is the decrement for subsequent pulses.

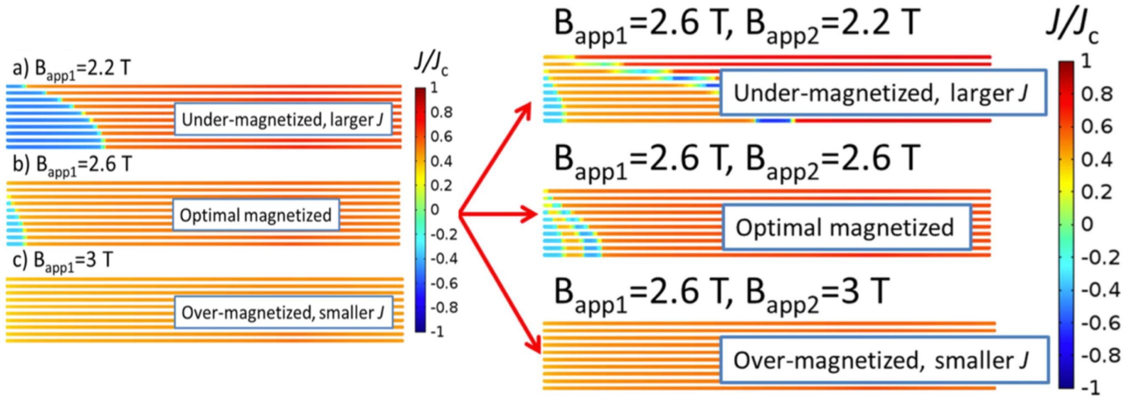

Figure 4.9–Normalised current distribution after first and second pulse. Only a quarter of the cross-section of the stack is shown. Thickness of the HTS layer is exaggerated for visualisation. Reproduced from [134].

In the analysis the first pulse is chosen to optimise the trapped field, although the centre of the sample still has current density in an opposite direction (see Figure 4.9), the trapped field is higher as the current density in the remainder of the sample is higher, as the pulse caused smaller temperature increase during the pulse. The choice of the second pulse follows the same lines, showing that it is best to apply a pulse of the same magnitude. However, after application of the of several pulses of the same magnitude, the improvement in trapped field starts to decrease, and a smaller pulse needs to be applied, to further improve the current density at the periphery of the sample. Similarly we can state that the best approach is to choose a sequence where the subsequent reductions in applied field are as small as possible.

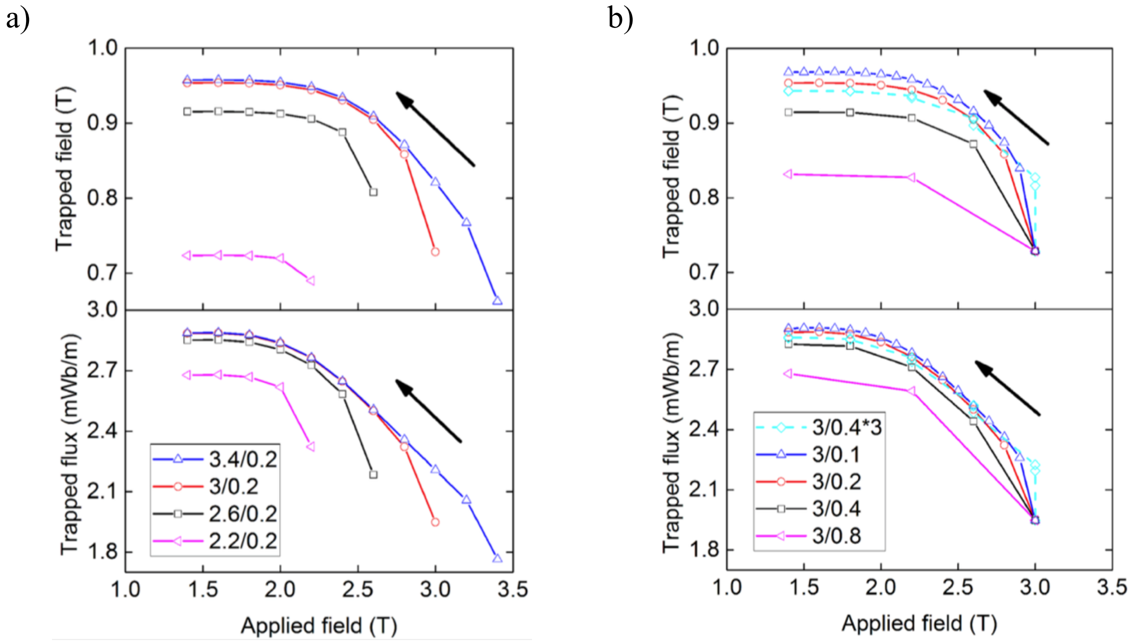

Figure 4.10–Trapped field and flux for sequences with different starting amplitudes a) and different amplitude intervals b). Reproduced from [134].

Similar applied field sequences, to those performed experimentally were tested, and the results are qualitatively identical (see Figure 4.10). The simulations show limited improvement in field if the sequence starts at a field above a certain threshold, and the making the decrement of applied field between successive pulses minimal helps to improve trapped field and flux.

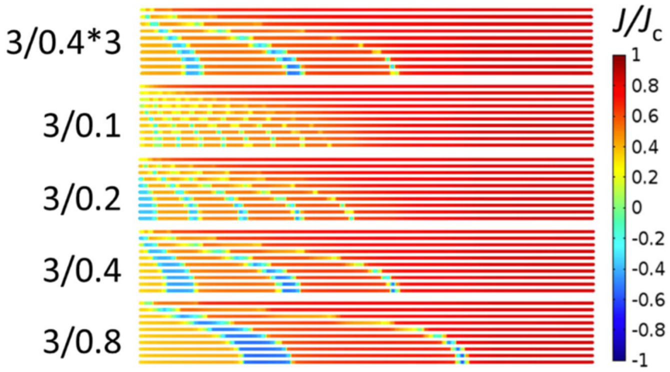

Figure 4.11–Final normalized critical current density of the pulse sequences with different amplitude intervals. Only quarter of the cross-section of the stack is shown. Thickness of the HTS layer is exaggerated for visualisation. Reproduced from [134].

However, the model of course does not reproduce the flux jumps observed during the experiments, however it is likely that the large current density (and magnetic field) gradients in the sample as shown in Figure 4.11 for sequence 3/0.1 may lead to relaxation by a flux jump during an applied magnetic pulse.

4.8 Effect of duration of the pulse

The duration of the pulse has a strong effect on the final trapped field. Zero field cooling can be considered as a very long pulse, but because the sample temperature can be kept constant during the magnetic field ramp, the maximum possible trapped field can be achieved (same as for field cooling). As the “pulse” gets shorter, sample heating cannot be avoided. However, by extending the pulse duration, the sample may be given more time to dissipate the heat generated during the rapid flux motion during the pulse. In this section we consider two different pulsed field durations.

The RCL circuit in the pulsed field magnetisation system described in 2.4 was modified to add additional resistance in line with the pulsed field coil to extend the pulsed field duration. The two pulsed field profiles tested are illustrated in Figure 4.12a. Due to the specifics of the magnetisation system used, it is difficult to decouple the field duration and the shape of the pulse. Hence, the two pulses show different shapes, namely, the longer pulse has a shorter rise time, but a much longer fall time.

The same sample from the previous sub-sections was used to determine the effect on trapped field. The results are shown in Figure 4.12b. A relatively small increase in pulsed field duration (8 ms, or 29%) has shown significant improvement in trapped field after a single pulse, close to 20% in trapped field above the sample for the optimum field of 2.8 T.

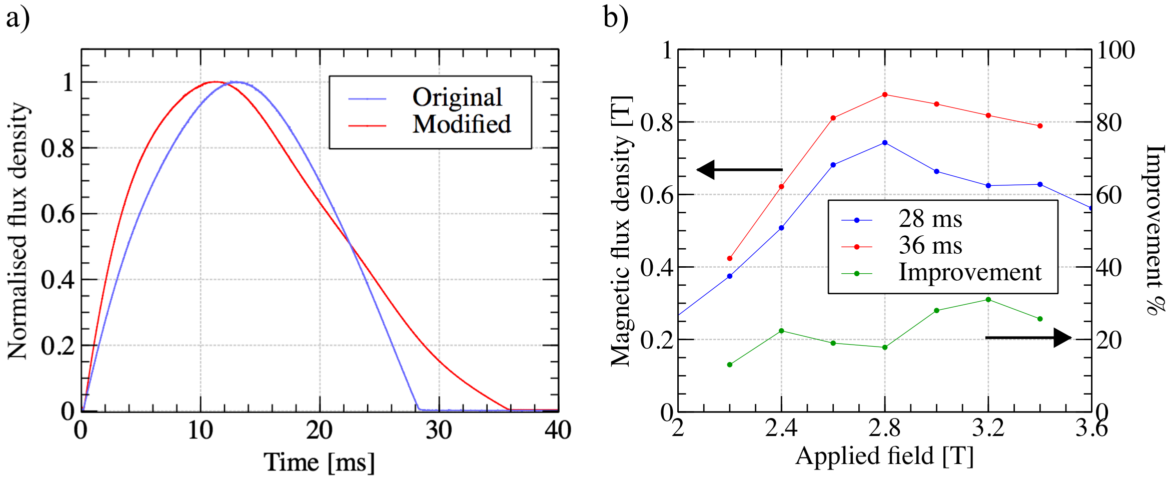

Figure 4.12–a) normalised profiles of the 28 ms and 36 ms magnetic field pulses tested; b) trapped field above a 20-layer stack resulting from single pulses for the two pulsed field profiles in a).

The same comparison is made for multi-pulse magnetisation and the results are summarised in Figure 4.13. We see a similar improvement in the trapped field as in the case for a single pulse, although the final trapped flux is very similar, due to the fact that mostly the outer portion of the sample contributes to the flux, and the low magnitude pulses (even for shorter pulses) are effective in trapping flux in the periphery of the sample. However, as was seen previously in Figure 4.4, for all sequences tested, the trapped flux in the sample increases sharply below a certain threshold of about ~2.6 T. However, Figure 4.13b shows that the trapped flux starts increasing at higher applied fields indicating that the temperature rise in the periphery of the sample is lower for longer applied field of the same magnitude.

It is important to note that the starting field of the sequence of 3 T is too low to achieve maximum trapped field as indicated by data shown in Figure 4.3, however the current modification of the system does not allow fields much higher than 3 T, but modifications are planned to allow for higher applied field with much greater pulse durations.

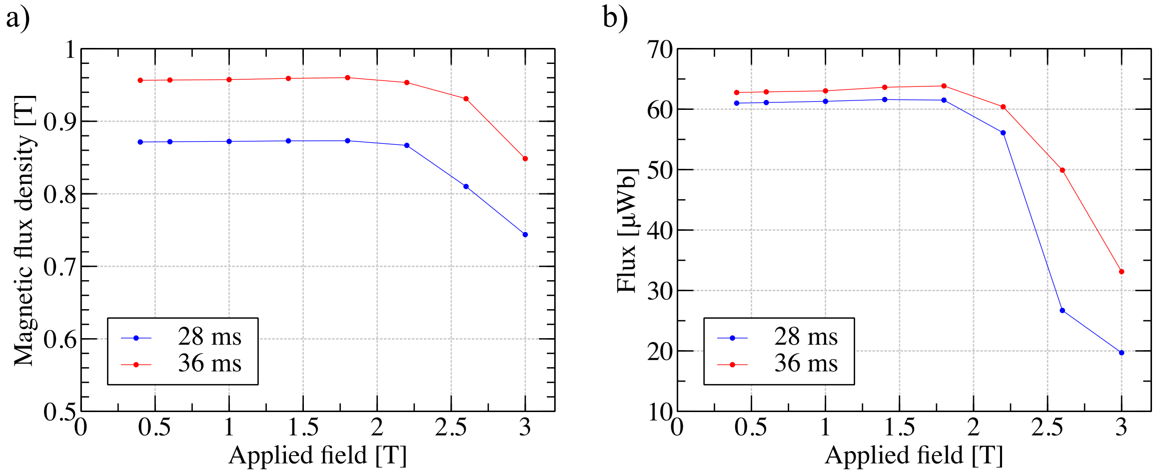

Figure 4.13–Trapped field a) and flux b) above a 20-layer sample after a multi-pulse sequence starting at 3 T applied field for the two applied field durations tested.

4.9 Conclusions

It was proved that despite the fact that the optimal pulse sequence can't be known a priori and there is not one universal magnetisation sequence for all samples, both the elaborated experiments and simulations can help to optimise the pulse sequence for maximising the trapped field and flux. In particular, single-pulse magnetisation experiments can show in which field ranges to apply pulsed fields to optimise either the peak field or the trapped flux. Both can be maximised by applying pulses with as small as possible field decrement. However, to reduce the total number of pulses (and thus time taken for magnetisation), one can focus on pulses in the vicinity of the optimal pulse for single-pulse magnetisation to effectively increase the peak-trapped field, and below that optimal field to increase the trapped flux. At low temperatures, flux jumps may be a factor to make the results of a magnetisation sequence less reproducible, however, this problem is not present at higher temperatures, which are more forgiving due to better thermal stability of the HTS tape stack (owing to higher heat capacities of materials at temperature above ~40 K).

Another important parameter of the magnetic pulse is its duration. Initial testing was performed showing a substantial increase in trapped field with only marginal increases in applied field duration. Moreover, the pulse can be engineered to have different rise and fall times, that may facilitate flux jumps on the rising edge, allowing a relatively small applied field to penetrate the sample, whilst slow subsequent decay, does not cause significant temperature rise, or another flux jump. Such pulse shapes have already been used as described in section 1.4.4.2, but detailed studies are still required for investigating the effect of the shape of the applied field.

Chapter 5 Modelling and experiments of field cooling

As in one of the postulates presented in section 1.8, the predictable behaviour of stacked HTS tapes due to the uniformity of the starting material, allow for more deterministic prediction of field profile and magnitude. However, most FEM models of trapped field magnets do not incorporate such parameters as critical current and n-value dependency on the angle of applied magnetic field, leading to only qualitative modelling results. More quantitative results can be obtained from incorporating more data for superconductivity and thermal properties of the material. Such models can be used as a starting point for most geometries and both trapped field and current transport modelling problems. An FEM model of a stack of tapes was constructed using the H formulation, incorporating goniometric critical current and n-value measurements. The modelling results were compared to field cooling experiments for stacks of different heights. The experiment and modelling show good agreement. Some of the results presented in this section are published in the article [135].

5.1 Methods and techniques

5.1.1 Superconducting tape samples

Superconducting tape used for this work was produced by SuperPower Inc. to specification SP12050 AP, i.e. $(Y,Gd)_{1+x}Ba_2Cu_3O_{7-\delta}$ with 7.5% of Zr added. The stated $I_{c,\min}$ was 240 A, at 77 K and self-field, over the whole length of the tape. However, segments tested showed much higher I_c, as shown in section 5.2.1. The tape was 12 mm wide with a 50 μm thick Hastelloy substrate and a 2 μm thickness silver over-layer. The overall thickness of the tape was ~55 μm.

The tape was cut to 12x12 mm square pieces to make stacks for field-cooling tests and 40 mm long segments for goniometric critical current measurements.

5.1.2 Goniometric critical current measurements

Goniometric measurements were performed at 77 K in liquid nitrogen and a magnetic flux density range of 0 to 0.5 T. The measurement system used in this study is described in section 2.2.2. For the purpose of this study, the rotational angle θ was varied between -180° and +180° while the tilt angle ϕ was kept at 0°. Orientation $\theta = 0°$ and $\phi = 0°$ corresponds to tape normal being parallel to the applied field (see Figure 2.3b).

The sample voltage was measured across 1 cm and an electric field criterion of 1 μV/cm was used to determine the critical current, although values of up to 5 μV/cm were measured to make power law fits to the *I-V* curves in order to determine the *n*-value. Full width samples were tested at 0.5 T and 0.4 T, however, in order to keep I_c below 200 A due to limitations of the experimental setup, further tests were made on samples with the width reduced to 6 mm. The measured I_c values were then extrapolated to those expected for full width samples by direct comparison of values obtained for both half-width and full-width samples at 0.5 T, 0.4 T and self-field. The half-width sample consistently showed 2.85 times lower I_c, likely due to properties of the tape being slightly worse at the edges of the tape compared to the centre. Narrower width also makes the tape's performance more susceptible to localized defects. A total of three samples were measured, each showing I_c values within 5 A of each other.

It is worth noting that the effect of self-field in current transport measurements is a concern only for small applied fields, when the self-field is comparable to the applied field. Simulations show that the self-field on the tape (averaged across the cross-section of the tape) did not exceed 20 mT during the experimental tests. However, this could add to the discrepancy in FEM modelling when the stack contains only a few tape layers. For this reason, the effect of self-field for I_c measurements is addressed in section 5.2.3.

5.1.3 Field Cooling of Stacks of Tape

A number of field cooling tests were performed with a varying number of tape layers. The orientation of each layer in the stack was kept identical: both the up-down and longitudinal-transverse orientation. The top surface of the stack corresponds to the (RE)BCO facing side of the tape. Field cooling was performed at 77 K in liquid nitrogen. The magnetic field was applied via an electromagnet. The magnetic field was ramped down from 1 T at a rate of 0.1 T/s to ensure that the sample is fully magnetized. After field cooling the sample was removed from the electromagnet whilst keeping it in liquid nitrogen to ensure that the measurement is not affected by the proximity of ferromagnetic electromagnet poles. The field was recorded 2 minutes after the end of field cooling to ensure flux creep, which is most rapid just after magnetization, does not affect the results significantly. The field was measured 1 mm above the surface of the stack, centred in the middle.

5.1.4 Modelling Framework

Modelling was done in COMSOL Multiphysics 5.1 using the *H* formulation, which is widely used for modelling problems that involve superconductivity [136]. And is described in more detail in section 2.6. The *E-J* power law was modified to include magnetic field and field angle dependent superconductivity properties

$$E = E_0 \left(\frac{J}{J_c(B,\theta)}\right)^{n(B,\theta)} \tag{5.1}$$

where $E_0 = 1$ μV/cm, J is the current density, $J_c(B,\theta)$ and $n(B,\theta)$ are the critical current density and n-value dependencies on the magnetic field magnitude B and orientation θ. The critical current density was obtained from the ratio of critical current (from goniometric measurements) and total cross-sectional area of the superconducting tape (see 5.1.1). No functional form was fitted to $J_c(B,\theta)$ or $n(B,\theta)$. Instead, linear interpolation was used between data points shown in Figure 5.1. For $n(B,\theta)$, the data was first smoothed by considering two nearest neighbours of each data point before using the data in the model (the smoothed curve can be seen as a solid line in Figure 5.1b). For $B > 0.5$ T linear extrapolation was used, although fields of more than 0.5 T in the interior of the stack were achieved only for stacks larger than 40 layers. To match the experimental setup, the field was ramped from 1 T at the rate of 0.1 T/s and the trapped field was recorded after 120 s. The trapped field value was taken 1 mm above the stack, corresponding to the top side of Figure 5.2a.

In order to reduce the computational time needed, a 2D-axissymetric model was used, although the stacks themselves are rectangular. However, experimental tests have shown that fields trapped in square and round stacks differ by less than 4%, making this a reasonable simplification. Moreover, individual layers were not modelled, instead the stack was homogenized, as in [137], maintaining the same engineering critical current density as in the real stack. All tests were isothermal, hence the thermal physics were not considered, thus the magnetic field ramp rate is not critical for the simulation. On the other hand, the flux creep just after the magnetization procedure is significant, and it is crucial that the trapped field measurement is done at the same time after the magnetization for both the experiment and simulation.

It is worth noting that an axisymmetric model is more suitable for HTS tape showing symmetric $J_c(B,\theta)$ and $n(B,\theta)$ with respect to $\theta = 0^\circ$. This is often the case in tapes with no artificial pinning centres, or spherical pinning centres only, as produced by e.g. SuperOx [59] and Fujikura. The superconducting tape used in this study contains columnar pinning centres [20] giving rise to more intricate $J_c(B,\theta)$ curves. In this instance, the model fails to capture differing J_c values, for example, for two opposite radial directions, where the magnetic field orientations have an opposite sign. Given that for the tape used $J_c(B,\theta) \neq J_c(B,-\theta)$, especially at low fields (when the stack contains a low number of tape layers), this may introduce an error in the modelling results.

5.2 Results

5.2.1 Goniometric characterisation of the coated conductor

The results from goniometric tests are shown in Figure 5.1. The critical current shows marked asymmetry with respect to $\theta = 0^\circ$, which is chosen as the direction of tape normal, the *a-b* plane peak is also shifted slightly away from $\theta = 90^\circ$ due to the *a-b* plane not being parallel to the tape surface (vicinal) as described in [138]. At magnetic fields larger than 100 mT, another peak near $\theta = 0^\circ$ emerges due to *c*-axis aligned pinning.

Figure 5.1b also shows the *n*-value variation with magnetic field and its angle. The data is noisy, due to fact that data was only gathered until the electric field reached 5 μV/cm in order to avoid heating the sample. This resulted in relatively few data points for each fit. Nevertheless, it can be clearly seen that the *n*-value is slightly larger near the *a-b* plane peaks in the $I_c(\theta)$ curve.

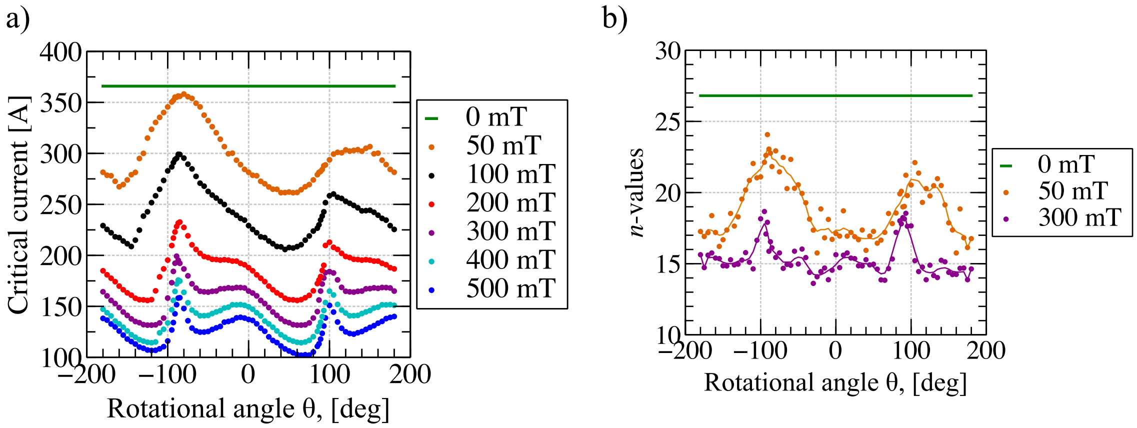

Figure 5.1– Critical current at 77 K for magnetic flux density up to 0.5 T across the whole rotational angle range (a). The peak near $\theta = 0^{\circ}$ at higher fields corresponds to *c*-axis aligned pinning due to Zr additions. The *n*-values for selected field values (for clarity) are shown in (b). Note that the (b) also has an angular dependency.

5.2.2 Modelling results and the comparison to experiment

The experimental data shows that the trapped field tends to saturate rather quickly as the number of layers is increased. As can be seen from Figure 5.2b, the model that incorporates J_c dependence on the magnetic field direction (full $J_c(B,\theta)$ and $n(B,\theta)$ dependence) agrees well with the experimental data, whist the model that only considers the magnetic field magnitude (reduced $J_c(B,\theta = 0^{\circ})$ and $n(B,\theta = 0^{\circ})$ dependence) overestimates the trapped field for larger stacks. This highlights the importance of J_c anisotropy in predicting trapped fields in stacks of tape.

Small discrepancies are observed between experimental and modelling data for low numbers of layers, this is most likely due to the fact that small variations in the individual layer performance are most significant when there are only a few layers in the stack and limitations of the model described in section 5.1.4. A small percentage of the layers may also suffer from damage during cutting [131].

Interestingly, the non-symmetric $J_c(B,\theta)$ gives rise to non-symmetric current density with respect to the mid-plane of the sample (Figure 5.2a), and the trapped field below the sample is expected to be up to 5% larger (in the 100 layer case) than above the sample. This still needs to be verified experimentally as the trapped field was only measured on one side of the stack (corresponding to the top side of Figure 5.2a. However, if the tape is stacked in random orientations, this effect should be diminished.

Other factors that may influence the accuracy of the predictions is the fact that the stacks in reality are square and not 2D-axisymetric. Also, regions in the stack, near corners experience magnetic field that is not in the plane perpendicular to the current direction, i.e. $\phi \neq 0^{\circ}$. However, it is expected that in those regions, the critical current density is in fact larger as goniometric scans spanning a range of ϕ and θ values [138] show that the lowest critical current densities are recorded for $\phi = 0^{\circ}$. Hence, the current is limited by sections in the stack where ϕ is indeed 0° and J_c dependence on the tilt angle ϕ is not the limiting factor for trapped field. Nevertheless, these factors are secondary and the model predictions fit the data within experimental error.

5.2.3 Further improvements to modelling

The $J_c(B,\theta)$ calculated from $I_c(B,\theta)$ by just considering the cross-section of the tape does not take into account the self-field, and therefore, for low external applied magnetic fields, the actual magnetic field in the superconductor is the superposition of the applied magnetic field and self-field and may differ significantly from the applied field. The effect of the self-field

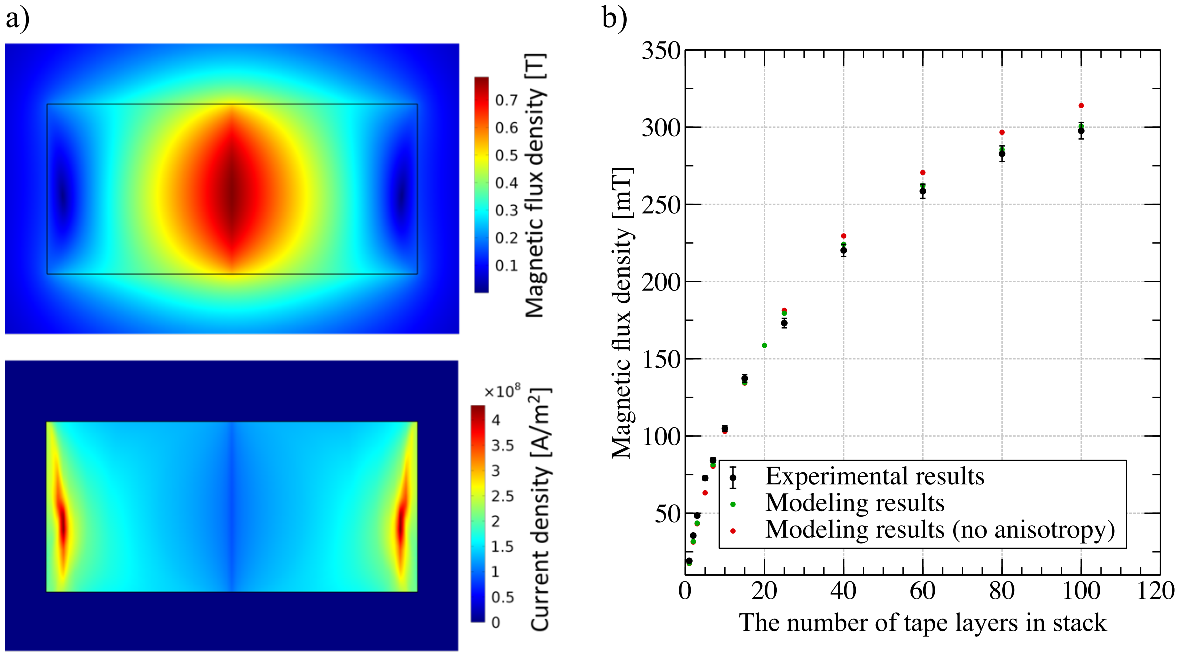

Figure 5.2– a) Modelled magnetic flux density and the current distribution. Interestingly, the figures are not symmetrical in the vertical direction as the $J_c(B,\theta)$ is not an even function; b) experimental data and modelling results of trapped field after field cooling a stack of (RE)BCO tape with varying number of layers. FEM model that includes anisotropic J_c agrees with experiment very well, while the model that did not include anisotropy shows overestimates for trapped field for large stacks.

was subtracted from the measured $I_c(B,\theta)$ data by a parameter free method described in [107], which iteratively corrects the $J_c(B,\theta)$ until modelled forward problem (calculating $I_c(B,\theta)$) matches the measured $I_c(B,\theta)$. The comparison of $J_c(B,\theta)$ corrected for self-field and data just scaled by the cross-sectional area is given in Figure 5.3. The figure shows that the critical current density is underestimated using uncorrected data up to fields of 50 mT, and as expected the $J_c(B,\theta)$ is not modified at fields above 50 mT. The corrected $J_c(B,\theta)$ was then used to re-run the simulations for stacks with 1-10 tape layers. The difference between the modelling results with corrected and not corrected $J_c(B,\theta)$ was from 4% for a single layer down to 0.2% by the time the stack contains 7 layers. The mismatch between the experimentally measured trapped field and modelling was reduced, however 3-9% error remained for stacks with number of layers below 10. Nevertheless, absolute magnitude of the mismatch is small (< 5 mT) and may be attributed to other assumptions in the model and the error in the placement of the Hall probe and critical current variation between the individual layers.

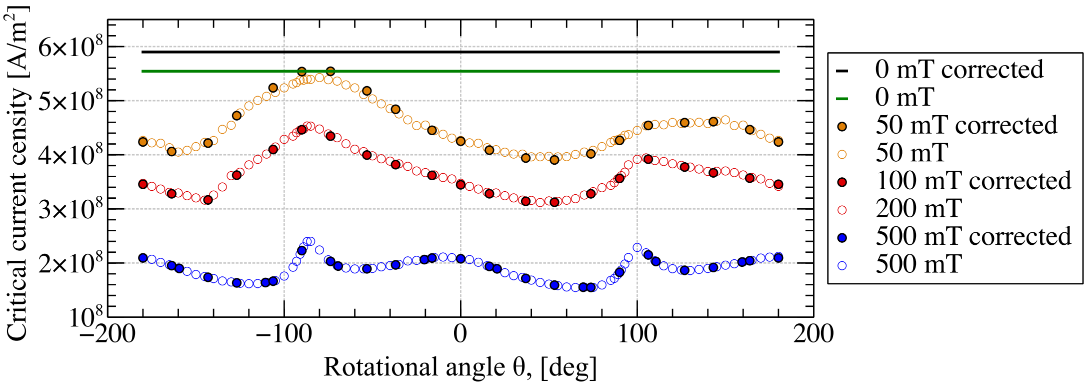

Figure 5.3–Critical current density of the HTS tape determined from I_c by considering only the cross-sectional area (empty circles) and the values corrected for self-field (filled circles).

5.3 Time independent (stationary) model

The model described in section 5.2.2 yielded good agreement with the experimental data, however, since it solves for the complete evolution of magnetic flux density during magnetisation and afterwards (minutes in simulated time), it can take substantial amount of computing power and time to solve. Ideally, one would like a model that can tell the maximum trapped field in the tape stack (or bulk) given the measured critical current dependence on temperature, magnetic field (and its direction) in a time-independent way. However, this is essentially impossible as the trapped field decays over time due to flux creep (described in section 1.4.5.1), so at best we can solve for flux density after a specific time following magnetisation procedure. Moreover, the measured critical current is somewhat arbitrary as it is determined according to some electric field criterion (usually 0.1 to 1 μV/cm). A superconductor carrying a modest 500 A current at a criterion of E = 1 μV/cm is already dissipating 0.5 mW/cm, which constitutes a significant energy loss. Hence, measurements for persistent current magnets, the electric field criterion for determining critical current is as much as 6 orders of magnitude lower [17]. Similarly, the electric field in a tape stack or a bulk will quickly decay below 1 μV/cm. It is then natural to think that a smaller critical current criterion should be used, if one wants to solve for trapped field in a stationary model (non-time dependant). The time dependent model described above, can give some insight on the time evolution of the electric field within the sample, which can then be used for obtaining the electric field criterion to be used for determining the trapped magnetic field a certain time after the magnetisation procedure.

Figure 5.4a presents the average electric field in the stack obtained from the time-dependant simulation described adobe, showing a linear behaviour in log-log space after magnetisation, as expected for a power law behaviour. The curve constitutes time-dependant electric field criterion that can be used in the in the stationary model to compute the flux density above the

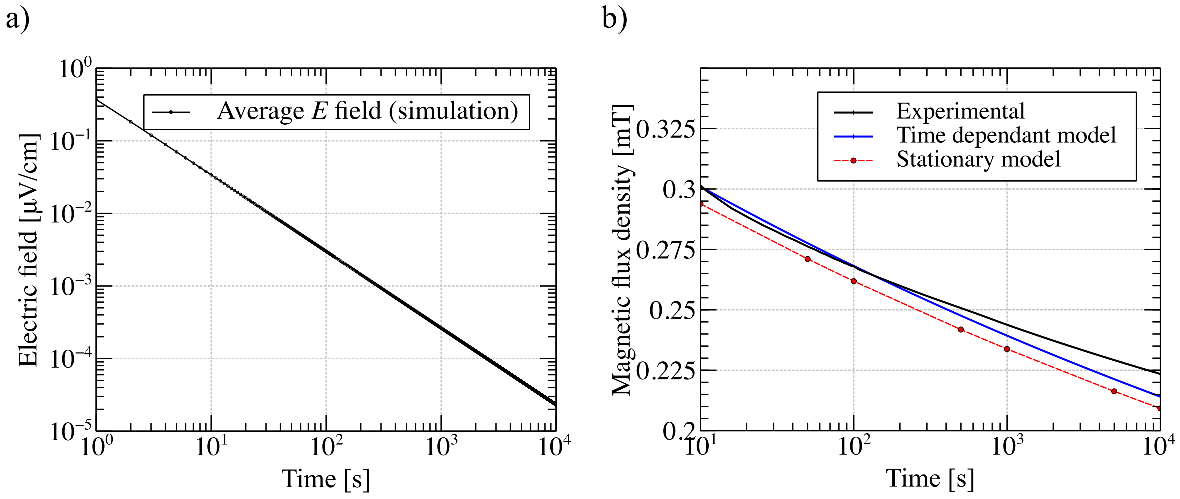

Figure 5.4– a) average of electric field within the stack obtained from the time-dependant model described in section 5.1.4; b) Relaxation of the flux density measured above the sample as well as obtained by the time dependant and stationary models.

tape stack for a specific time after magnetisation. In the time independent (stationary) model, the current at every point in the stack is simply set according to the power law:

$$J = J_c(B,\theta)\left(\frac{E}{E_0}\right)^{\frac{1}{n(B,\theta)}} \tag{5.2}$$

where E_0 is the electric field criterion used for determining $J_c(B,\theta)$, whilst E is the electric field for which the current is determined (E is time dependent). The results obtained by the stationary (non-time dependant) model were then compared to the trapped field obtained by the time dependant model and experimentally measured values for a stack with 100 layers. The experiment was performed in a different sample holder with the Hall probe at a distance of 1.3 mm from the stack surface, as compared to previous experiments that were done with the Hall probe at a separation of 1 mm. The results are summarised in Figure 5.4b. The stationary model reproduces the same decay rate as the time dependant model, however the absolute value is noticeably smaller. The reason is that the electric field within the sample is not uniform, hence the electric field average is not sufficient to find the current distribution within the sample. The region in the sample with the maximum current as shown Figure 5.2a contributes to the measured trapped field significantly, and the electric field in this region is higher than electric field averaged over the whole sample.

Also from the comparison of experimentally measured magnetic field decay and that obtained by time dependant model, it is apparent that the model overestimates the flux creep. The experimental data shows curvature in the log-linear plot as predicted in the collective creep theory (see section 1.4.5.1). This is not reflected in the modelling results, because the E-J power law does not describe the electric behaviour of the superconductor for low J/J_c and a flux percolation model would be more suitable [139]. Nevertheless, the deviation from the results obtained by modelling is relatively small.

5.3.1 Non axis-symmetric geometries

In the previous section we considered a cylindrical, axis-symmetric geometry where the current is automatically conserved as it circulates in perfect concentric circles. However, the current conservation must be considered separately for the case of rectangular samples, where rotational symmetry is not present. If the current at each point in the sample is defined by equation (5.2), then the current conservation is not ensured. This problem was addressed in joint publication with Victor Zermeno et. al. [140] from Karlsruhe Institute of Technology, the modeling was mainly performed in KIT, while I have collected and elaborated on the experimental data.

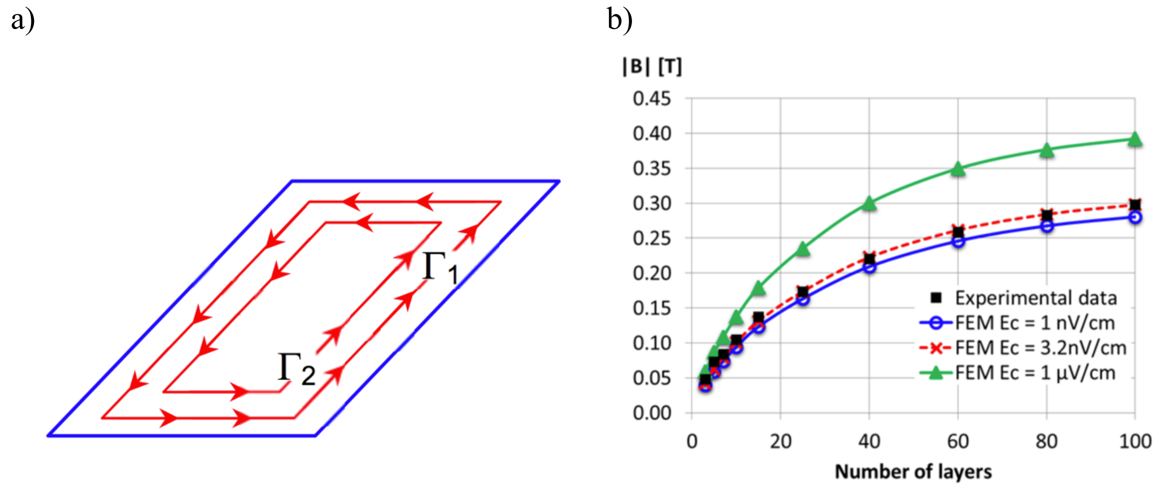

Figure 5.5– a) current streamlines in the superconducting tape following the contours of the sample; b) experimentally measured trapped field above a stack with different number of tape layers together with calculated values using different electric field criterions. From [140].

We know that the current circulating in the tape layers follow the contours of the sample to a good degree (high *n*-value) as predicted by the Bean model (see section 1.2.3) and indeed it can be shown from the current reconstruction using Hall probe magnetometry (see section 2.3.1). Moreover, the supercurrent is confined to the individual, flat layers. Then the sample can be subdivided into a set of streamlines Γ_i as shown in Figure 5.5a. The *minimum* current is computed along each streamline according to a specific electric field criterion. The minimum value along the entire streamline sets the current value for that specific streamline. The electric field criterion was then found by fitting the modeling data to experimental values, and was determined to be 3.2 nV/cm (see Figure 5.5b). The resulting fit to the data is very good considering that due to different magnetic field magnitude and orientations, the mean electric field for stacks with different number of tape layers will be slightly different.

5.4 Conclusions

The trapped field within a stack of HTS tape layers with different sizes (different number of layers) was successfully predicted by a time dependant FEM model using materials data collected from a single layer of the HTS tape. Both the critical current and the *n*-value dependence on the magnetic field and its orientation were included in the *E-J* power law to model the HTS stack. The model showed good agreement despite the simplified geometry of the model used, which was further improved by accounting for the self-field contribution in the $J_c(B,\theta)$. Small deviation from the experimental data were observed at for thin stacks (low number of tape layers) that is considered to be due to differences in the individual tape layer performance and possibly a small error in the exact Hall probe location.

A time independent model was also developed for more rapid trapped field determination, that reduced computation time significantly. Axially symmetric, and more complicated rectangular geometries were investigated. However, the results were less encouraging as the accuracy depends on the electric field criterion used, which is essentially a fitting parameter. The electric field varies with time and is not uniform within the stack, however, reasonable estimates of how the electric field varies with time can be obtained from the time-dependant model or by fitting the results to experimental data. It is expected that the criterion will also change for samples with substantially different $J_c(B,\theta)$ values. Even more fundamentally, the *E-J* power law breaks down for low J/J_c values (i.e. long times after magnetisation). Nevertheless, this stationary model is useful for comparative estimations. The average electric criterion shows power law behaviour with time, and can be extrapolated, from even short time-dependant simulations. The difference between estimated field by stationary model and experimentally measured field was below 10%.

Chapter 6 Towards record trapped field values

The currently held record for the highest trapped field value in (RE)BCO trapped field magnet is an impressive 17.6 T by Durrell et al. [37]. Although this record value is not going to be attainable for most applications due to the geometry of the measurement (field measured between two (RE)BCO bulks in close proximity), it displays the potential and the limitations of the material. At low temperatures, bulk (RE)BCO is primarily limited by the mechanical properties (see section 1.5.3) and not critical current, which is very difficult to improve, necessitating external reinforcement and application of pre-stress using carbon fibre [69] or a steel-band [37]. However, it is hoped that the strong metallic substrate of coated conductors will help to sustain mechanical stresses to fields above 20 T. This section explores the current limitations of achievable trapped field using stacks of 2G HTS coated conductor tape.

6.1 Samples

Three sets of samples were tested from Fujikura, SuperOx and SuperPower. Tape from Fujikura and Superpower we formed into stacks as loose layers compressed in the sample holder, whereas SuperOx tape was soldered into self-supporting stacks as described in 3.1.2. The tape was cut to form 12x12 mm stacks for SuperPower and SuperOx, whereas tape from Fujikura was stacked into 10x10 mm stacks, as it is provided in 10 mm width. Table 6.1 summarizes the properties of tape. It is evident from the data that the SuperPower HTS tape has at least twice the engineering critical current density, owing to its extremely thin substrate. To maintain a similar size of the stack, 200 layers were used instead of 100 as for the other two stacks. The 6.9 mm height of the SuperPower tape stack makes for a good comparison to previously published data on trapped field for ~65 µm thickness SuperPower tape [56].

Table 6.1 – Properties of three superconducting tapes tested

Parameter	Fujikura	SuperOx	SuperPower
Stated J_c at 77 K and S.F. [A]	450	400	450
Tape width [mm]	10	12	12
Overall thickness [µm]	~85	~82 (after soldering)	~34
Stabilisation	8.2 µm Ag	1 µm Ag, 5 µm Cu and 10 µm PbSn	3 µm Ag
Engineering critical current density J_e at 77 K and S.F. [kA/cm^2]	52.9	40.7	107.1
Number of layers per stack	100	100	200
Height of a single stack [mm]	8.9	8.2	6.9

The extremely small thickness of SuperPower tape tested required additional precautions when handling the tape. The tape possesses significant curvature in direction perpendicular to the intended current transport axis, which can make it buckle akin to a metallic measuring tape. Hall probe scans were made to investigate whether there is significant damage on cutting the tape by scanning the tape layers before and after they have been cut (see Figure 6.1). No significant damage was observed, although the resolution of the scans is limited due to large tape-sensor distance (0.95 mm) required to accommodate for the significant curvature of the sample.

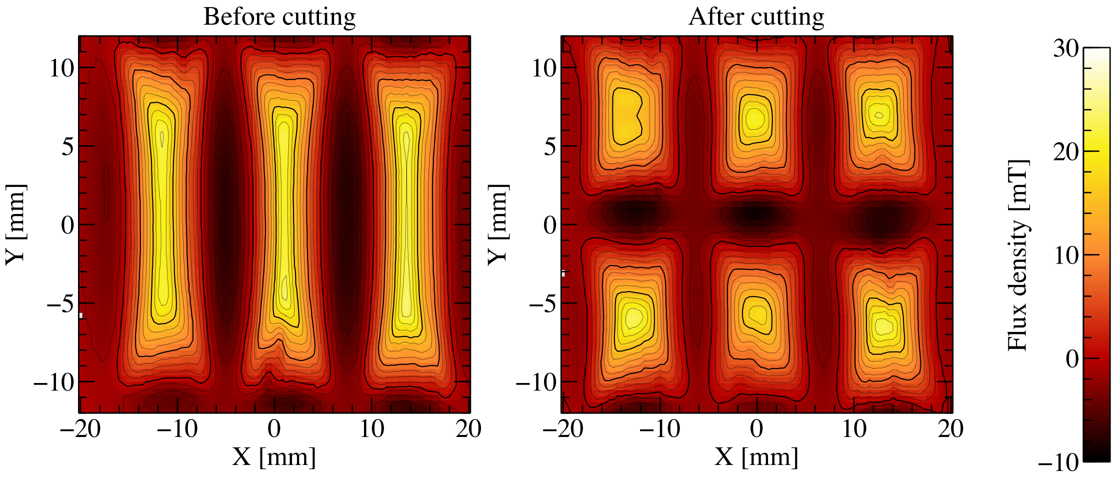

Figure 6.1–Hall probe scan (scan height of 0.95 mm) of three 24x12 mm tape layers from SuperPower before and after cutting them into six 12x12 mm tape layers. No significant damage is evident in the cut interfaces.

However, if there were pre-existing defects aligned with the transport axis, they could not be distinguished from cutting damage, as the current density is only perpendicular to the transport direction in the vicinity of the cuts. Nevertheless, more consistent and reproducible cutting technique are being investigated for future research, such as punching, as currently used for Roebel cable production [141].

6.2 Field cooling

Field cooling measurements were done in International Laboratory of High Magnetic Fields and Low Temperatures in Wroclaw, Poland as described in section 2.5.2. The field was measured between two stacks of the same tape, and the details for a single stack are outlined in Table 6.1. The results for the field cooling of HTS tape stacks from the three manufacturers is summarised in Figure 6.2. The temperature in the plots below is taken to be the temperature of the sample at the end of the field ramp.

It is evident that the extremely high engineering critical current density of SuperPower 35 μm thick tape gives a significantly higher trapped field values. In fact, an engineering critical current density of at least 107.1 kA/cm^2 is approaching the values typical of bulk superconductors, even though the volume fraction of the superconductor is less than 6%. It is interesting to note that the trapped field is almost linear with temperature and despite the

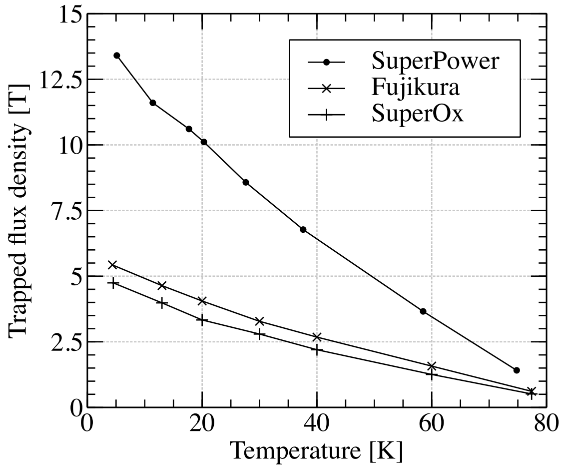

Figure 6.2–Field cooling results for the tree different types of HTS tape tested.

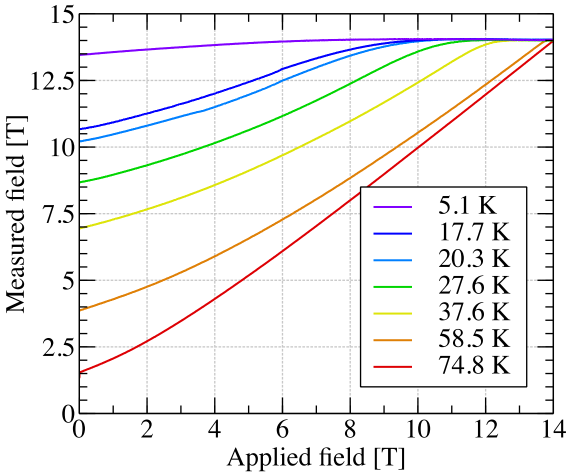

Figure 6.3– The measured field between two tape stacks (SuperPower) as the applied field is ramped down from 14 T.

differences in field and temperature scaling for the different tapes. The trapped field values for any temperature scale quite well with J_e at 77 K and self-field (after correction by a factor of 1.2 for Fujikura tape due to smaller width). Another point to make is that the trapped field is limited by the critical current and not by mechanical properties or flux jumps down to liquid helium temperatures, unlike bulk superconductors (as depicted in Figure 1.27). In fact, the tapes were magnetised several times with no observable degradation. Figure 6.3 shows the field measured in between two stacks of SuperPower tape as the external magnetic field is ramped down from 14 T. It is obvious that the applied field of 14 T is very marginal, and higher magnetic field would ideally be required to ensure that the sample is fully saturated at 4.2 K.

Figure 6.4 shows two field cooling attempts of SuperPower tape stacks at a starting temperature of 4.2 K. Due to aggressive ramp rate used, the first attempt (Figure 6.4a) resulted in a flux jump with a peak temperature of more than 30 K and the field magnitude rapidly decreased to 5.2 T. On second attempt (Figure 6.4b), a slower ramp rate was used and a temperature increase was detected, however it did not result in flux avalanche and the sample managed to trap 13.4 T. It is worth noting that at the end of the ramp the sample temperature was over 5 K, and a slightly higher trapped field would be expected if the ramp rate was even slower and the sample was maintained at a constant 4.2 K.

The metallic substrate and highly thermally conductive stabilisation layers allowed for much faster field ramp rates, than typically used for bulk superconductors (i.e. 1-2 T/hr), and in the temperature range where the heat capacities are even lower. Even though a flux avalanche was

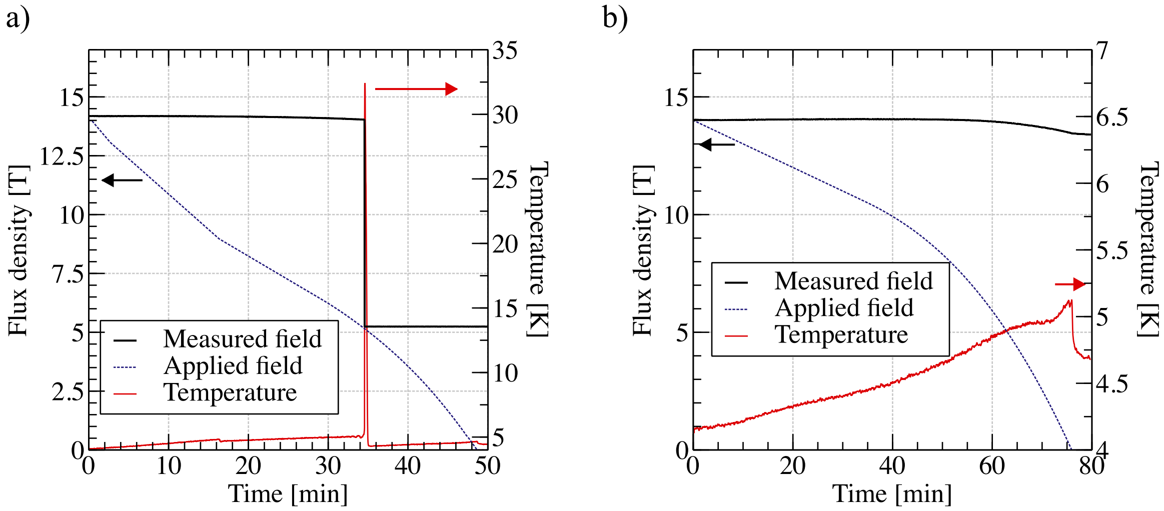

Figure 6.4– Field cooling of SuperPower tape stacks starting at 4.2 K. First a) and second b) ramp attempt. First ramp attempt resulted in flux jump due to fast ramp rate used.

observed near liquid helium temperatures, relatively fast ramp rates of 5-15 T/hr could be used for Fujikura and SuperOx samples and 10-15 T/hr for the SuperPower sample across all temperature ranges.

As mentioned before, the trapped field in stacks is limited by the critical current, as opposed to bulk (RE)BCO, which is limited by the mechanical properties. Consequently, stacks are operating in a fully saturated critical state, where the current density is close to the critical current density throughout the stack. It can be expected that the creep rate for stacks would be higher in the temperature range where bulk (RE)BCO is limited by mechanical properties and operates in non-saturated state, with the central region of the bulk being subcritical. This will affect the relaxation of the current density within the bulk. As it was observed, that the temperature could be raised from 26 to 32 K without decrease in the central field.

Figure 6.5a shows the relaxation of the measured field between the stacks of SuperOx tape after field cooling. The measured field decay is well described by a logarithmic function after the initial ~100 s period where the decay is slower. As expected, the rate of decay decreases with temperature. Figure 6.5b shows the rate of decay in % of trapped field per time decade for all three samples tested. However, due to limited access time to the magnet used for measurements, the creep rate for Fujikura and SuperPower samples were estimated from a smaller dataset, spanning from 3 to 5 min after the magnetisation. Moreover, at temperatures below 10 K sample heating during ramp have exceeded 1 K, as shown in Figure 6.4b, but dropped down quickly after magnetisation. It is worth remembering that the creep rate can be reduced by field cooling at a higher temperature before reducing it back to operational temperature, in effect lowering J/J_c, potentially at a loss in trapped field magnitude that would be achieved if magnetisation was performed at the operational temperature (see section 1.4.5.1). Therefore, the creep rate at lower temperatures may be an underestimate. The creep rate, however generally decreases with temperature, and the reduction is quite rapid for temperatures below 20 K. Also, interestingly, the creep rate of the SuperPower sample was the highest for high temperatures, but decreased most rapidly as the temperature was lowered. Creep rate for the current record holding (RE)BCO sample by Durrell et. al. [37] was estimated from data in the publication and included in the figure, although, logarithmic trend was less clear in the data. The flux creep rate was slightly lower for the bulk sample for the same temperatures, however, due to the logarithmic nature of the decay, it is unlikely to be issue for motor applications for either bulk or stacked tape trapped field magnets.

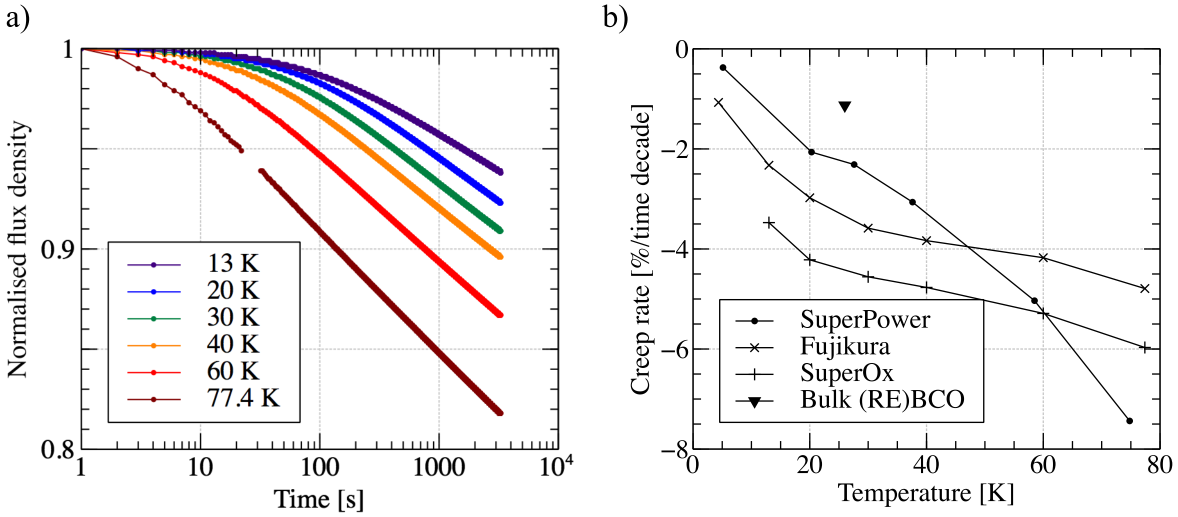

Figure 6.5–a) Relaxation of trapped field for SuperOx sample at different temperatures showing logarithmic decay; b) creep rates for all three types of tape tested and comparison to a value for the currently record holding bulk (RE)BCO sample from [37].

The trapped field of 13.4 T at 5.1 K or 10 T at 20 K is still lower than the record trapped field for bulk superconductors, however it is worth noting that only a portion of identically prepared bulk (RE)BCO samples can sustain fields of more than 10 T due to cracks present within the sample, even when external reinforcement is applied. This probability of mechanical failure for bulks at low temperatures and high fields combined with degradation due to thermal cycling make the bulks less attractive for engineering applications, especially those where there is low tolerance to critical failure, regardless of the potential advantage in performance. However, as the coated conductor manufacturers matures, the availability of tape with high critical current will be increasing (even now a 450 A critical current for 12 mm width is considered average), which may eventually close the gap between performance of bulk (RE)BCO and 2G HTS tape stacks.

6.3 Pulsed field magnetisation

Pulsed field magnetisation experiments were also performed for the three different types of tape. However, only a single stack of each tape was magnetised with the field measured 0.8 mm above the stack surface. This measurement geometry is more indicative of the ones that will be used in applications.

For pulsed field magnetisation tests, an IMRA sequence with sequential cooling was used as per Table 6.2. The sample was not heated between temperature stages, just lowered to down in temperature where another sequence was performed. Due to higher engineering critical current density for the SuperPower sample, much higher magnitude pulses needed to be applied to fully penetrate the sample.

Table 6.2 – Pulse sequence starting fields. Pulses were applied with 0.2 T decrement until trapped field starts to decrease with additional pulses.

Temperature	Fujikura	SuperOx	SuperPower
[K]	Start field [T]	Start field [T]	Start field [T]
77.4	2.6	2.6	2.8
60	4	4	6.4
50	4.6	4.6	6.8
40	5	5	7.2
30	5	5	7.2
20	4.8	4.8	7.2
10	4.4	4.4	7.2

The pulsed field magnetisation results for the three stacks are summarised in Figure 6.6. As expected, the SuperPower sample performed the best, followed by Fujikura, consistent with field cooling experiments. As before, at high temperatures (60-77 K) the trapped field ratios follow the engineering critical current density ratios quite well, however, this is no longer true for lower temperatures. As described in section 1.4.4, during pulsed field a magnetisation substantial amount of heat is generated, which raises the sample temperature and reduces the trapped field.

The temperature rise is more evident at lower temperatures due to lower heat capacities at low temperatures and higher critical current. For the same reason, samples with higher J_e, will exhibit more heating. Therefore, increasing J_e does eventually lead to diminishing results for trapped field. The flux density profiles above the SuperPower sample in Figure 6.7 show a large increase in trapped field as the temperature is reduced from 77 to 60 K, where the heat capacities of materials are still relatively, high, but only very marginal improvements are achieved as the temperature is lowered further. Also, the profile at low temperatures has a rather blunt shape, suggesting that the sample is not saturated, i.e. the current near the centre of the sample is much lower than the critical current.

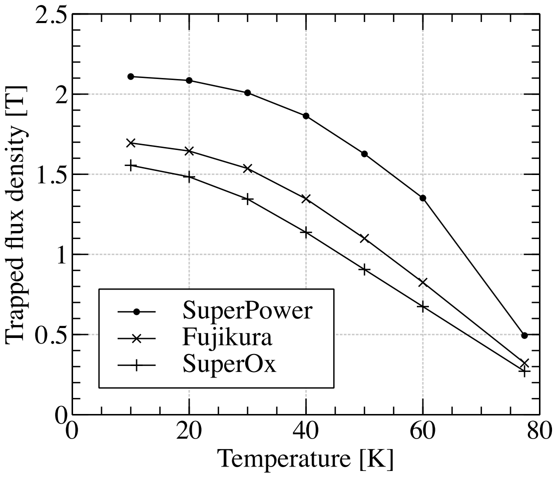

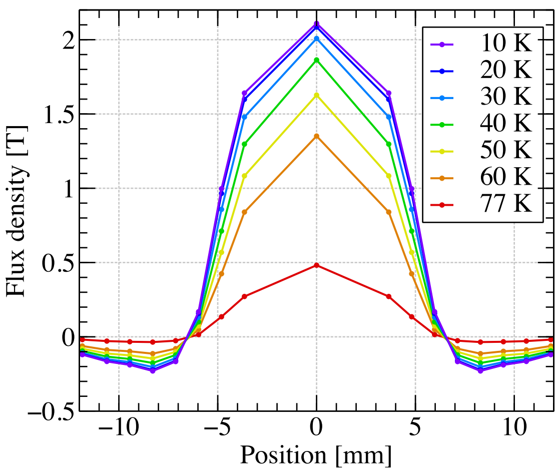

Figure 6.6–Pulsed field magnetisation results for a single stack of each type of tape. Field measured 0.8 mm above the sample surface. IMRA sequence with sequential cooling was used.

Figure 6.7–Flux density profile above the SuperPower sample after each temperature stage of the pulse sequence. The profiles at low temperatures are clearly not saturated.

6.4 Conclusions

Field cooling of three different types of tape was performed, showing the current state of the art for trapped field in trapped field magnets made from 2G HTS coated conductor. A maximum field of 13.4 T was achieved at ~5 K in the best sample with the highest engineering critical current density J_e. This is 70% higher than the previously reported [73] largest value for this type of trapped field magnet, and is approaching the record values set by bulk (RE)BCO trapped field magnets. No mechanical degradation was observed during multiple magnetic field ramps and temperature cycles. High thermal stability was shown by fast field ramps at very low temperatures. Unlike for bulk (RE)BCO, the performance is limited by the critical current, or rather the engineering critical current of the stack, hence the following approaches to further increase the trapped field values are suggested:

- increasing the critical current of each tape layer – larger J_e;
- decreasing the overall tape thickness (most likely the substrate thickness) – larger J_e;
- increasing the width of the tape, and hence the size of the stack.

On the other hand, for pulsed field magnetisation, the increase in J_e does not give equivalent increase in performance (compared to field cooling) at low temperatures, due to the increase in heating due to rapid flux motion during PFM. Therefore, a reduction in temperature rise is the key point for increasing the trapped field. This can be achieved by extracting the heat more quickly by sinking the heat using thermally conductive materials (Chapter 3), allowing more time for heat dissipation by extending the duration of the pulse itself (section 4.8) and optimising the applied pulse sequence (Chapter 4). Alternatively, inducing a flux jump which leads to relatively large trapped fields compared to applied fields as seen for high J_e bulk [43] may be attempted. This may be possible with further tailoring of the pulse shape.

Chapter 7 Pulsed field magnetisation of an array of trapped field magnets

Trapped field magnets (TFMs) such as bulk superconductors or stacks of coated conductor tape can unlock higher power densities for motors and generators by taking the role of field poles in the rotor. Engineering applications place stringent requirements on the mechanical properties of TFMs. Therefore stacks of tape are becoming an increasingly attractive option for use in motors and generators. Fields trapped in HTS stacks are approaching those trapped in bulk (RE)BCO (see Chapter 6) and have reached the level required for some applications.

Two approaches exist for scaling up stacks of tape for applications as illustrated in Figure 7.1. Wider tape offers both higher trapped field and flux. At the time of writing, large width tape (up to 46 mm wide) is commercially available, but its performance in terms of A/cm-width does not match that of the best tape, available in smaller widths. This does not

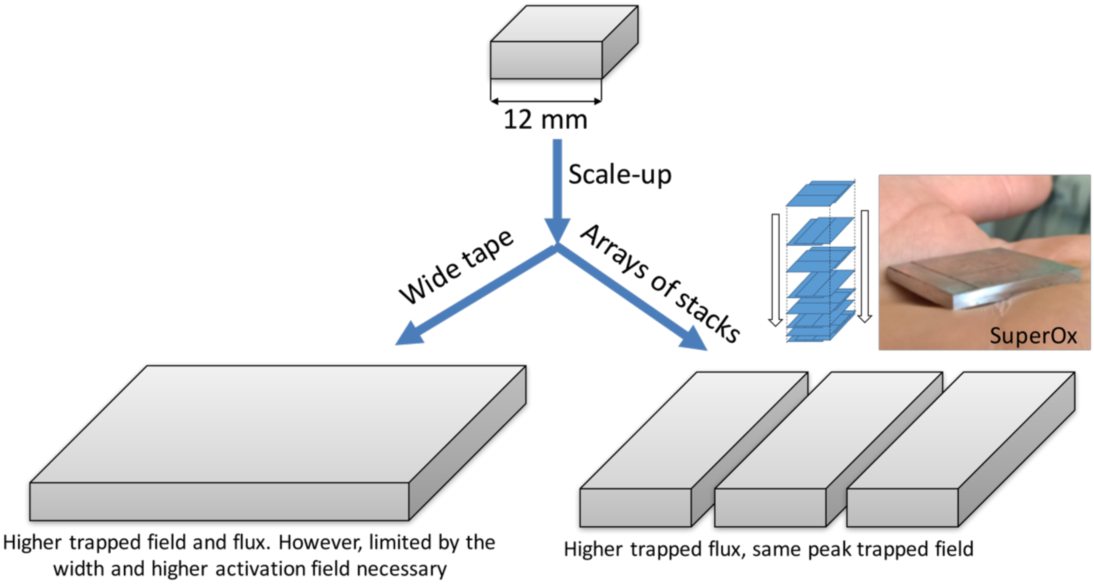

Figure 7.1–Approaches of scaling up of stacks of HTS tape for use in applications

reflect the limitations for developing high performance large width coated conductors, but rather a current lack of demand for larger width HTS tape. Nevertheless, an array of narrower stacks can be scaled up to any size and the field required to activate the stack is lower. More uniform fields can be achieved by varying the stacking arrangements (inset in Figure 7.1) and such stacks have already been field cooled [142,143] and used for magnetic levitation [103]. However, pulse magnetisation of stack arrays is yet to be demonstrated. This work focuses on a simple 3×1 array of stacks with variable separation to compare and contrast magnetisation of a single stack and an array.

7.1 Experimental setup and modelling framework

7.1.1 Samples

The 2G HTS coated conductor used in this work was produced by Fujikura and has a width of 10 mm and an 85 µm overall thickness comprising of a 75 µm Hastelloy substrate, ~0.4 µm buffer stack, 2.9 µm GdBCO layer and 8.2 µm Ag over-layer. The tape has an average critical current of 547 A at 77 K and self-field). Three stacks of 30 layers each were formed. The dimensions of the stacks and the overall array are given in Figure 7.2. The tape layers had the same orientation throughout the stack. Three sample holders were made corresponding to the three tested stack separations, namely 0.5, 2 and 4 mm. The same three stacks were used for all experiments and their relative positions when transferring from one sample holder to another were maintained the same.

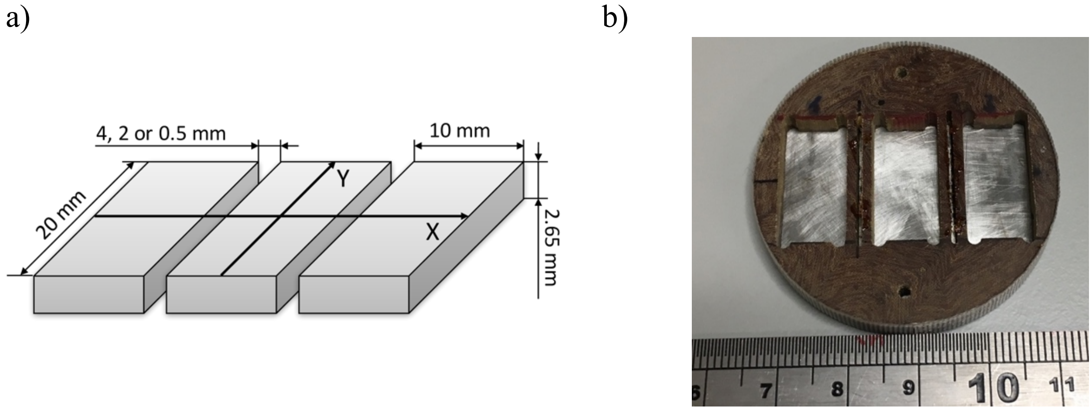

Figure 7.2– a) dimensions of the HTS stack array, *X* and *Y* arrows show the directions referred to later on; b) sample holder for the array with 4 mm separation

7.1.2 Pulsed field magnetization

The TFM setup is described in detail in section 2.4. The same three stacks were mounted in the different sample holders and pulse magnetised in the bore of a solenoid coil. The results were compared to pulse magnetisation of a single (central) stack alone. The samples were magnetized using both a single pulse and multiple pulses (iterative magnetisation with reducing amplitude, IMRA). All pulses were delivered at a temperature of 40 K. Between each magnetisation test the sample temperature was raised above the critical temperature, to 100 K, to ensure that no field is trapped in the sample prior the magnetisation procedure. The pulse sequence for IMRA magnetisation started at 5 T then successive pulses were applied, each reducing in amplitude by 0.4 T to a field of 1 T. The trapped field was measured via an array of hall probes 0.8 mm above the sample surface 30 s after delivering each pulse.

7.1.3 Modelling framework

The Finite Element Method modelling was done in COMSOL Multiphysics 5.1 using the **H** formulation as described in section 2.6. An *E*-*J* power law was used that incorporates the magnetic field dependency of the critical current and the *n*-value. The problem was reduced to a 2D-infinite model and due to symmetry, only ¼ of the geometry was actually modelled. Each stack in the experiment has an aspect ratio of 2, and the field is measured across the central line of the stack (arrow X in Figure 7.2a), thus the end effects are less important and the 2D-infinite approximation is justifiable. The geometry of the model and the mesh is depicted in Figure 7.3.

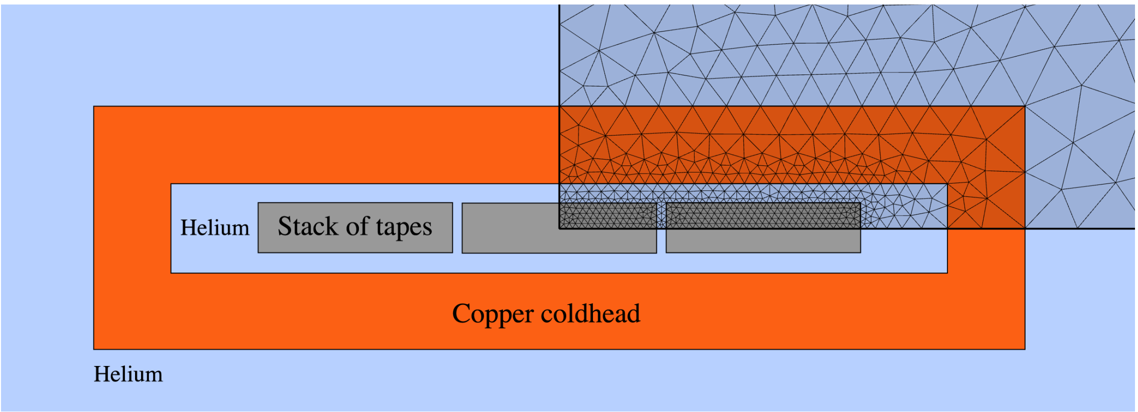

Figure 7.3–Simulated geometry of the problem. The meshed area indicates the actual simulated geometry, i.e. reduction to a ¼ of the problem via symmetry

To enable the use of symmetry, a global constraint for no net current in the outer stacks had to be applied (the current is circulating within the stack).

The individual layers were not modelled; instead the properties of the stack were homogenized to avoid large element counts necessary to model the thin HTS layers. This approach was successfully used before [136]. The homogenisation procedure ensures that the critical engineering current density of the stack is maintained. The thermal properties are also homogenised, however the overall thermal conductivity perpendicular and parallel to the tape layers is maintained anisotropic. The thermal conductivity was calculated as outlined in [137]. The cooling power in the experimental system is difficult to replicate as the sample is cooled via convective heat transfer between the cold-head of the cryocooler and the sample via helium gas. This allows for variable sample geometry and mounting options, however makes it difficult to know the cooling power exactly. The model employs a similar approach where the stacks are not directly attached to the cold-head, but are separated by the Helium gas. The cooling power of the cold-head is taken as described in section 2.6 and previously reported in [137].

7.1.3.1 Materials properties used for modelling

One of the difficulties for modelling pulsed field magnetization is that superconducting properties are dependent on a variety of operating conditions and that materials data is not always readily available across all the relevant temperature and magnetic field ranges. This is especially true for the n-value parameter of the *E-J* power law fit. Very limited literature exists on the n-values for HTS tape at temperatures below 77 K and high magnetic fields. Hence, a numeric function, that is in line with measured data presented in [123] was used:

$$n(B) = \frac{0.15}{(0.095 + B^2)} - 1.58 \times B + 21.3 \quad (\text{for } 0 < B < 6\,\text{T}) \tag{7.1}$$

The n-value data from [123] for SuperPower coated conductor alongside the relationship (7.1) is shown in Figure 7.4b. For the sake of simplicity, the n-value is taken to be independent of temperature as the data available has significant scatter and a clear trend in this temperature is not evident. Also, the n-value is not expected to vary hugely in the temperature range of 40-50 K, relevant to the model. On the other hand, the $J_c(T,B)$ data used was for a coated conductor from the same manufacturer and with the same architecture [121]. The data was scaled to match the average critical current at 77 K for the batch of tape used in our experiments. Moreover, the critical current data above 3 T was extrapolated using an exponential fit of the data in [121] in the region of 1.5-3.0 T. The used critical current and *n*-value is shown in Figure 7.4. Other materials properties, including thermal properties, were taken as described in section 2.6.

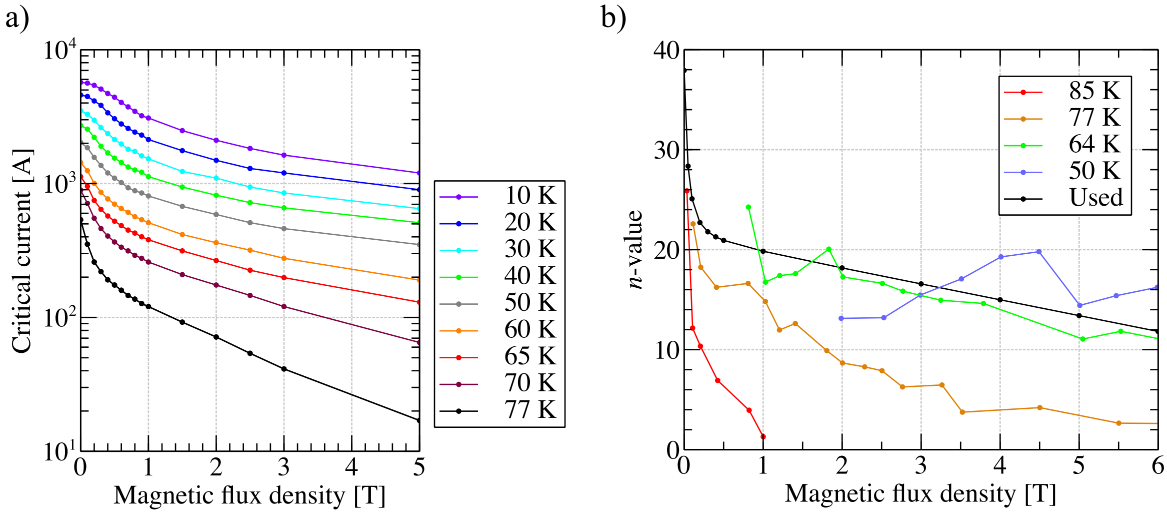

Figure 7.4– a) critical current density data for Fujikura coated conductor, data taken from [121] and extrapolated past 3 T; b) measured *n*-values for coated conductor at various temperatures (data taken from [123]) and a smoothed version was used in simulations.

7.2 Experimental results

7.2.1 Pulsed-field magnetisation

Single pulse magnetisation was carried out to investigate the effect of the proximity of the stacks with each other on the trapped field. Figure 7.5a shows the trapped field above the central stack for a single stack and a three-stack array with varying separation between the stacks. Before each pulse, the samples were heated above the critical temperature to ensure that there are no pre-existing currents in the sample. The Figure 7.5 shows that the magnetic field decreases after the introduction of the neighbouring stacks and the reduction in trapped field gets worse as the stack separation decreases. At the same time, the peak trapped field shifts to lower applied fields. The trapped field is reduced by 11-15% depending on the proximity of the neighbouring stacks. The reduction is already significant for separations as high as 4 mm, but the reduction seems to saturate at around 2 mm, as 0.5 mm separation gives almost identical results as 2 mm separation.

The trapped field can be increased using multi-pulse techniques (see section 1.4.4.1). A multi-pulse sequence starting from 5 T with subsequent pulses reduced by 0.4 T was applied resulting in an increase of trapped field by about 10% in each case. However, the decrease for trapped field compared to a single stack stays at 10-15% as shown in Figure 7.5b.

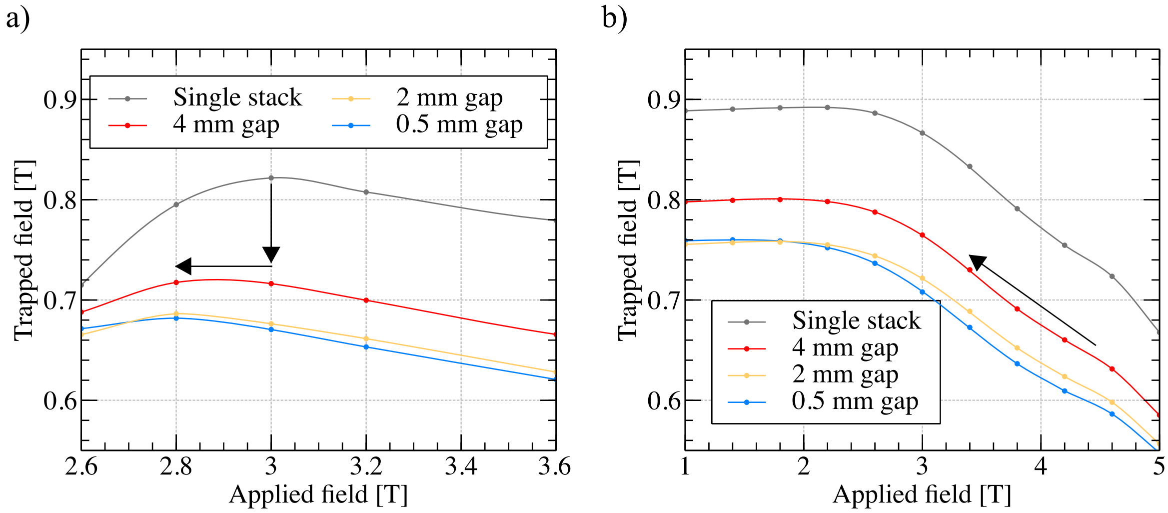

Figure 7.5– a) Single pulse magnetisation of a single and array of stacks, sample was heated to above T_c after each pulse, arrows indicate the decrease in magnitude and shift in the peak field; b) Multi-pulse magnetisation of the same, the sequence starts at 5 T and applied field is reduced by 0.4 T for each successive pulse (sequence direction indicated by the arrow), sample heated above T_c after each sequence.

7.2.2 Flux density profiles above the stacks

To determine if magnetising the stacks in an array affects the flux density profiles (component of magnetic field perpendicular to tape surface only) above the stacks, the field profiles were measured using a linear array of hall probes along the *Y* and *X* direction in the stack (refer to Figure 7.2a for representation of these directions). Figure 7.6 shows the profiles for a single stack and for an array of stacks with 0.5 mm separation after a multi-pulse sequence shown in Figure 7.5b. The magnetic flux density profiles exhibit the expected roof-top outline and pulse magnetisation in an array does not seem to influence the trapped field profile significantly. It is expected that the stacks are not fully saturated, however the resolution around the peak central stack is insufficient to determine this. The magnitude of the central peak is different in the measurements along the X and Y directions for the same array as there was some relaxation of the trapped field between the measurements.

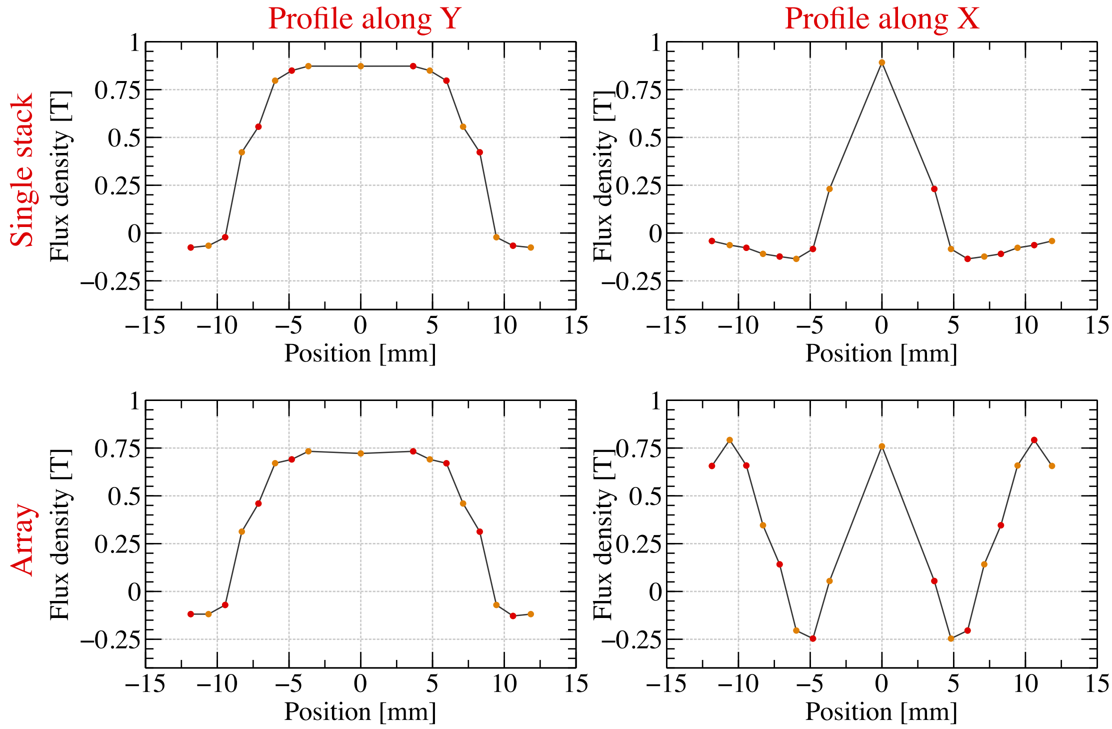

Figure 7.6–Flux density profiles along X and Y directions (refer to Figure 7.2a) for a single stack and an array of three stacks with 0.5 mm separation. The data points in red are not measured but inferred by symmetry and mirrored from the equivalent measured position across the origin.

7.3 Modelling

The results of the numerical simulation were used to determine the reasons for the reduction in trapped field in the array configuration. For the first attempt, to determine how the magnetisation procedure is affected by neighbouring stacks, we can linearly superimpose the profile expected for magnetisation of a single stack to form a field distribution of three arrayed stacks. In effect, we simulate the case where the stacks do not influence one another at all, and the resultant field is just the superposition of three separate distributions. This exercise was performed using modelled field profile of a single stack after a 3 T pulse. The results are shown in Figure 7.7.

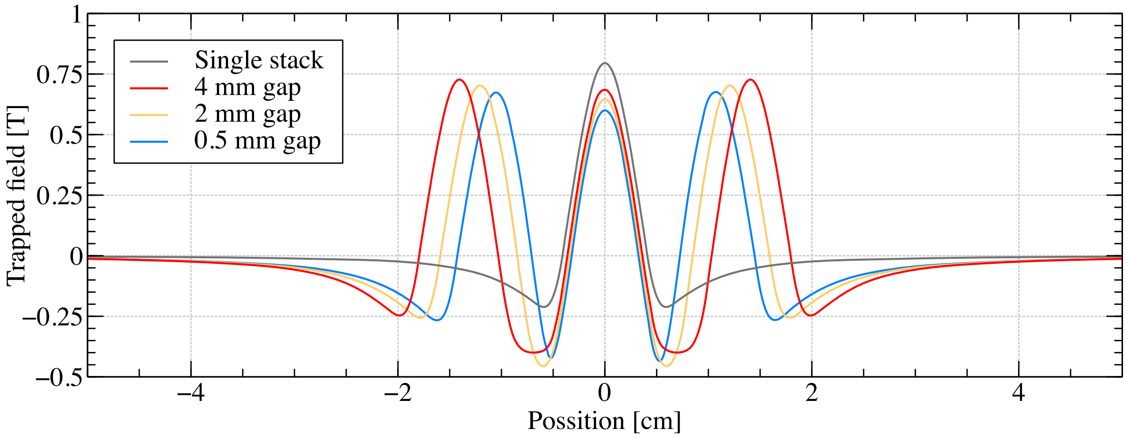

Figure 7.7–Results of simple linear superposition of trapped flux density profiles gives a fair approximation of the results, but fails to reproduce key features of experimental data in Figure 7.5a.

Essentially, the peak field is reduced above all three stacks as they reside in positions of negative flux density created by the neighbouring stack. This simplistic picture reproduces the measured central field remarkably well, thus, to first approximation we can state that the neighbouring stacks do not influence the magnetisation procedure significantly, even though the trapped field is smaller. However, by repeating the same exercise for 2.8 T applied field, we fail to reproduce the shift of optimum applied field to lower magnitudes for the arrayed configuration (as shown in Figure 7.5a), also the predicted flux density above the central stack is underestimated.

For this reason, a pulsed field FEM model considering all three stacks was developed and the results are summarised in (Figure 7.8). The model has successfully replicated both the position of the peak trapped field with respect to the applied pulsed field magnitude as well as the shift of this peak to lower applied fields upon introduction of the neighbouring stacks. As expected, the trapped field values also decrease as the separation between the stacks gets smaller. The discrepancy at very small stack separations can be attributed to the thermal interaction between the stacks, which is hard to model accurately due to the convective nature of the cooling used.

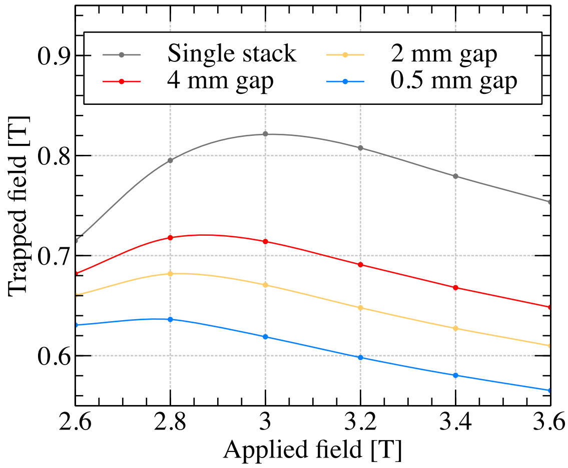

Figure 7.8–Modelling results of single pulse magnetisation, the results reproduce the experimental results well.

We can gain further insight by looking at magnetic field and current distributions during and after the pulse. Figure 7.9 shows the magnetic flux density in the middle of a 3 T pulse and 30 s after it for the different stack separations. It can be seen that the magnetic field in between the stacks gets intensified by the shielding currents within the stacks and reaches 4 T for the smallest separations.

This effect will increase the heating of the stack, reduce the critical current and result in smaller trapped field. For this reason, the peak trapped field shifts from 3 T to 2.8 T which results in less heating during the pulse. Even after the pulse, the edges next to neighbouring stacks experience higher magnetic flux density, which is going to reduce the critical current density and increase flux creep rate in that region. Figure 7.10 shows that the current distribution is markedly distorted by the presence of the adjacent stack, and the peak current position (which coincides with the position of minimum magnetic field strength) shifts away from the neighbouring stack.

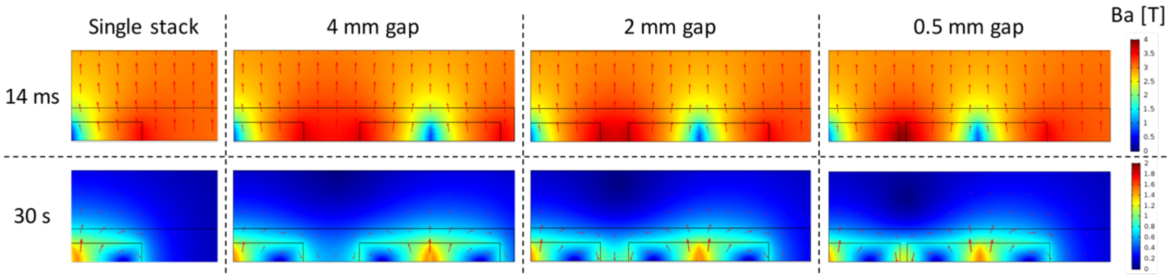

Figure 7.9–Magnetic flux density in the middle of the pulse and 30 s after a 3 T pulse for different stack separations. The results show that the magnetic field is intensified near the edges of the stack that are adjacent to neighbouring stack.

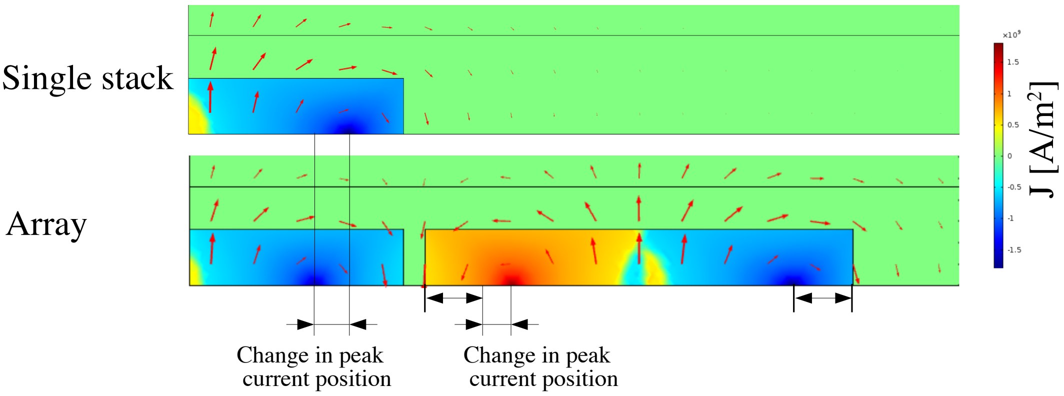

Figure 7.10–Change in the peak current position (lowest magnetic field) at the edge adjacent to a neighbouring stack.

7.4 Ferromagnetic additions

Additional heating due to enhanced field in the region between the stacks was identified as a contributing factor for the decrease in trapped field in the arrayed configuration. To test this hypothesis and to guide the magnetic flux density in the channel between the stacks, instead of increasing the flux density within the stacks themselves, the addition of ferromagnetic material was investigated. This was done by inserting thin strips of soft ferromagnetic NiFe alloy between the stacks (50% Ni and 50% Fe, magnetic data can be found in [144]). The strips had the same height and length as the stacks, each strip was 30 µm thick, and 12 strips were combined for a total thickness of ~0.5mm together with the binding material (GE varnish). The

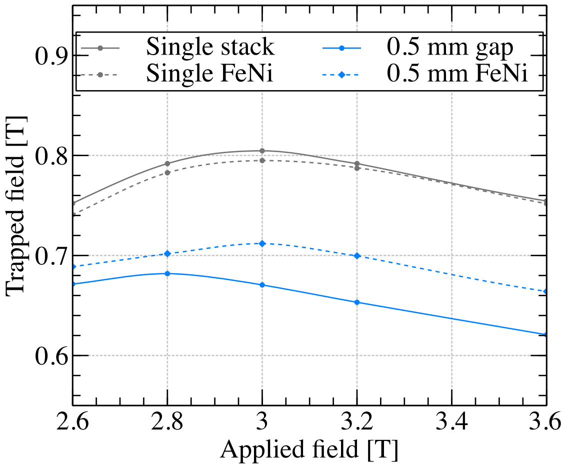

Figure 7.11–The effect of soft ferromagnetic material placed between the stacks for an array or either side of a single stack.

layers were stacked so that the applied field and the *c*-axis of the HTS tape are in the plane of the NiFe layers. The results for a single stack and an array with 0.5 mm separation are summarised in Figure 7.11. Other separations omitted for clarity, but follow the same trend. The performance of a single stack was not enhanced by the presence of NiFe, however, for an array with 0.5 mm separation, the trapped field was slightly higher and the peak applied field shifted back to 3 T. However, the positive effect of FeNi was less as the separation of the stacks increases. As the separation increases, the fraction of space between the stacks occupied by FeNi decreases (FeNi strip bundle of the same size was used for all stack separations). As the strip is centred in the gap between stacks, the reduction of field in the very vicinity of the stack is not as significant.

7.5 Conclusions

In conclusion, arrays of HTS stacks can be successfully pulse-magnetised to increase the overall trapped flux. Such arrays can then be used for field poles in motors and generators. To a first approximation, the adjacent stacks do not influence each other significantly and the trapped field profile is close to one achieved by simple superposition of single stack field profiles. However, the optimum applied field shifts towards lower applied field values due to increased heating at the periphery of stack, as shown by FEM modelling. As a result, the current distribution within the stack also changes, with the current density being shifted away from the edges that are adjacent to neighbouring stacks. Initial experiments with soft ferromagnetic material between the stacks has shown that the effect of neighbouring stacks can be reduced, but further optimisation is required for determining the best choice of material and investigation of potential problems due to hysteretic heating if the stack array is to be used for applications.

Chapter 8 Overall conclusions and further work

This section outlines the main conclusions of the thesis and describes the direction of further work that will be undertaken during my postdoctoral research.

8.1 Conclusions and further work

This work investigates the suitability of coated conductors for use as trapped field magnets and confirms their readiness for first demonstrator projects. Magnetisation by field cooling was successfully used to trap more than 13 T between two 12 mm square stacks highlighting the recent advancements in 2G HTS coated conductor technology, both in increasing the critical current density of the superconducting material, and reducing the substrate thickness. Both advancements help improve the engineering critical current density, which allowed for almost a doubling of the trapped field value in HTS stacks over the last 4 years from 7.34 to 13.4 T. Moreover, high thermal conductivity of the tape makes stacks more resilient against flux jumps during fast magnetic field ramps as compared to bulk (RE)BCO. No degradation or mechanical failure was observed during multiple magnetic field ramps and temperature cycling, enforcing the evidence, that the performance of the stacks is currently limited only by the engineering critical current density and the width of the tape. As coated conductor manufacturers further increase the critical current and produce wider tapes, trapped field values, higher than the current record of 17.6 T, are likely to be achievable.

Field cooling gives the upper limit for trapped field, however, pulsed field magnetisation is much more practical, and it is considered to be the primary way of magnetising trapped field magnets for applications. Therefore, ways of optimising PFM, to reduce the gap between the field achievable by field cooling and pulsed field magnetisation were investigated. Namely, by optimising the magnetic pulse sequence, it was shown that initial pulses must be high enough to generate current density in the very interior of the sample, however, the trapped flux only starts increasing below a threshold field, where the outer regions of the sample no longer experience excessive heating. By successive pulses with small decrements in magnitude, we can maximise the current density at all distances from the surface of the sample, despite the heat generated. Using thermally conductive structures attached directly to the stack was also been shown to be effective, resulting in a 10% improvement in trapped field for single pulse magnetisation, however, care must be taken to limit eddy current heating in these metallic (and electrically conductive) parts of the sample. The net thermal conductivity of (RE)BCO tape is much higher in the plane of the tape due to the highly thermally conductive silver over-layer and copper stabilisation. Therefore, the thermal mass was chosen to be attached on the sides of the stack, which is also where the most heating during a magnetic pulse occurs. However, as the width of the tape increases, the thermal mass is likely to become less effective, therefore internally embedded copper may be required, which would come at the expense of engineering critical current. Lastly and unsurprisingly, the duration of the magnetic pulse was also shown to increase the trapped field significantly, by nearly 20% in the case of single pulse magnetisation (pulsed field duration increased from 28 to 36 ms). However, whist it is obvious that longer pulses would result in higher trapped field, as the generated heat is allowed to dissipate, the shape of the pulse is also of significant importance, as some evidence in literature suggests that fast rising edge of the pulse may be beneficial for “flux jump assisted magnetisation”, while a slow decay allows for dissipation of heat, and suppresses the possibility of further flux jumps which lower the flux density within the trapped field magnet. Further studies that investigate both the duration and the pulse shape separately are required. While all the mentioned strategies contribute to increasing the trapped field for PFM, the combination of all three is expected to give best results as the strategies are not mutually exclusive, but rather complimentary. The in depth experience gained over the last four years will be used to increase the current record value of 2.1 T for pulsed magnetisation of stacks of HTS tape in future work. Finite element method computer models were used to model the behaviour of stacks using critical current measured in the laboratory or available directly from HTS tape manufacturers. The modelling results for both field cooling and pulsed field magnetisation matched the experimentally measured values well, which is possible due to the good uniformity of superconducting properties along the length of the tape. The modelling served as a useful tool to explain the experimental observations, as well as allowing extrapolation of the results to conditions where experiments could not be performed. As mentioned, the modelling results hinge on the accurate determination of critical current of the coated conductor at different operating conditions. To that end, a critical current measurement facility was designed and constructed during the PhD for measurements in helium vapour down to 10 K, 900 A and 1.5 T at variable magnetic field orientation.

Lastly, magnetisation of an array of stacks was performed, investigating the possibility of scaling up the size of trapped field magnets for motor applications, while the availability of high performance wide HTS tape is limited. The effect between neighbouring stacks during PFM was investigated. The results showed a reduction in the trapped field magnitude, but the reduction is similar to what would be predicted just by overlapping individual field profiles. Also, the applied field, required to fully penetrate the samples did not differ much from a single stack case. This may be an advantage over large width HTS tape, which would require higher applied field to magnetise the samples.

Overall, the high trapped field magnitudes combined with attractive mechanical properties suggest that stacks of HTS tape could be a viable option for field poles in electric motors. In future work, a prototype synchronous motor with stacks of HTS the on the rotor acting as permanent magnets will be developed in our ASCG research group in close collaboration with national and international partners. Such prototypes will answer the remaining questions on the viability of this technology in actual operating conditions. One such question is the effect of crossed field demagnetisation, which has not been characterised at low temperature and high AC magnetic field frequencies.

Publication list

First author publications:

- **Baskys A**, Filar K, Patel A, Glowacki B A 2017 Trapped field of 13.4 T in a stack of HTS tapes with 30 µm substrate (in preparation).
- **Baskys A**, Hopkins S C, Bader J and Glowacki B A 2016 Forced flow He vapor cooled critical current testing facility for measurements of superconductors in a wide temperature and magnetic field range Cryogenics (Guildf). 79 1–6
- **Baskys A**, Patel A, Hopkins S C and Glowacki B A 2016 Modeling of Trapped Fields by Stacked (RE)BCO Tape Using Angular Transversal Field Dependence IEEE Trans. Appl. Supercond. 26 6601004
- **Baskys A**, Patel A, Hopkins S C, Kalitka V, Molodyk A and Glowacki B A 2015 Self-supporting stacks of commercial superconducting tape trapping fields up to 1.6 T using pulsed field magnetization IEEE Trans. Appl. Supercond. 25 6600304
- **Baskys A**, Patel A, Hopkins S, Kenfaui D, Chaud X, Zhang M and Glowacki B A 2014 Composite superconducting bulks for efficient heat dissipation during pulse magnetization J. Phys. Conf. Ser. 507 12003

Co-authored publications:

- Mitchell-Williams T B, **Baskys A**, Guo Y, Hopkins S C, Bangert U, Molodyk A, Petrykin V, Gomory F, Frolek L and Glowacki B A 2017 Spark-Discharge Plasma as a Method to Produce Low AC Loss Multifilamentary (RE)Ba2Cu3O7 Coated Conductors IEEE Trans. Appl. Supercond. 27 5900405
- Zou S, Zermeño V M R, **Baskys A**, Patel A, Grilli F and Glowacki B A 2017 Simulation and experiments of stacks of high temperature superconducting coated conductors magnetized by pulsed field magnetization with multi-pulse technique Supercond. Sci. Technol. 30 14010
- Patel A, Hahn S, Voccio J, **Baskys A**, Hopkins S C and Glowacki B A 2017 Magnetic levitation using a stack of high temperature superconducting tape annuli Supercond. Sci. Technol. 30 24007
- Zermeño V M R, **Baskys A**, Zou S, Patel A and Grilli F Estimation of maximum possible trapped field in superconducting permanent magnets in 2D and 3D, (submitted)
- Mitchell-Williams T B, **Baskys A**, Hopkins S C, Kalitka V, Molodyk A, Glowacki B A and Patel A 2016 Uniform trapped fields produced by stacks of HTS coated conductor tape Supercond. Sci. Technol. 29 85008
- Atamert S, Kutukcu M N, Scandella J, **Baskys A**, Zhong Z and Glowacki B A 2016 Novel Superconducting MgB 2 Wires Made By Continuous Process 26 6201104
- Patel A, Kalitka V, Hopkins S C, **Baskys A**, Albisetti A F, Giunchi G, Molodyk A and Glowacki B A 2016 Magnetic Levitation between a Slab of Soldered HTS Tape and a Cylindrical Permanent Magnet IEEE Trans. Appl. Supercond. 26 3601305
- Mitchell-Williams T B, Patel A, **Baskys A**, Hopkins S C, Kario A, Goldacker W and Glowacki B A 2016 Toward Uniform Trapped Field Magnets Using a Stack of Roebel Cable Offcuts IEEE Trans. Appl. Supercond. 26 6800404
- Patel A, Hopkins S C, **Baskys A**, Kalitka V, Molodyk A and Glowacki B A 2015 Magnetic levitation using high temperature superconducting pancake coils as composite bulk cylinders Supercond. Sci. Technol. 28 115007

- Page A G, Patel A, **Baskys A**, Hopkins S C, Kalitka V, Molodyk A and Glowacki B A 2015 The effect of stabilizer on the trapped field of stacks of superconducting tape magnetized by a pulsed field Supercond. Sci. Technol. 28 85009
- Patel A, Usoskin A, **Baskys A**, Hopkins S C and Glowacki B A 2015 Trapped Field Profiles for 40-mm Wide Superconducting Tape Pieces J. Supercond. Nov. Magn. 28 397–401

References

[1] de Bruyn Ouboter R 1997 Heike Kamerlingh Onnes's Discovery of Superconductivity *Sci. Am.* **276** 98–103

[2] Schmüser P 2002 Superconductivity in High Energy Particle Accelerators *Prog. Part. Nucl. Phys.* **49** 155–244

[3] CCAS Timeline of superconducting materials, http://www.ccas-web.org/superconductivity/#image1

[4] Bednorz J and Müller K 1986 Possible high T_c superconductivity in the Ba−La−Cu−O system *Zeitschrift für Phys. B Condens. Matter* **193** 189–93

[5] Wu M K, Ashburn J R, Torng C J, Hor P H, Meng R L, Gao L, Huang Z J, Wang Y Q and Chu C W 1987 Superconductivity at 93 K in a new mixed-phase Yb-Ba-Cu-O compound system at ambient pressure *Phys. Rev. Lett.* **58** 908–10

[6] C G J and Adam H 1992 *SQUIDS, the Josephson effect and superconducting electronics.* (Bristol: CRC Press)

[7] London F and London H 1935 The Electromagnetic Equations of the Supraconductor *Proc. R. Soc. A Math. Phys. Eng. Sci.* **149** 71–88

[8] Ginzburg V L and Landau L 1950 On the theory of superconductivity *Zh. Eksp. Teor. Fiz* **20** 1064

[9] Abrikosov A A 1957 The magnetic properties of superconducting alloys *J. Phys. Chem. Solids* **2** 199–208

[10] Krabbes G, Fuchs G, Canders W-R, May H and Palka R 2006 *High Temperature Superconductor Bulk Materials* (Weinheim, FRG: Wiley-VCH Verlag GmbH & Co. KGaA)

[11] Schwarz a, Liebmann M, Pi U H and Wiesendanger R 2010 Real space visualization of thermal fluctuations in a triangular flux-line lattice *New J. Phys.* **12** 33022

[12] Bean C 1962 Magnetization of Hard Superconductors *Phys. Rev. Lett.* **8** 250–3

[13] Bean C 1964 Magnetization of High-Field Superconductors *Rev. Mod. Phys.* **267** 31–9

[14] Kim Y B, Hempstead C F and Strnad A R 1963 Magnetization and Critical Supercurrents *Phys. Rev. Lett.* **129** 528–35

[15] Rush J P, May-Miller C J, Palmer K G B, Rutter N A, Dennis A R, Shi Y-H, Cardwell D A and Durrell J H 2016 Transport in Bulk Superconductors: A Practical Approach? *IEEE Trans. Appl. Supercond.* **26** 1–4

[16] Lao M, Bernardi J, Bauer M and Eisterer M 2015 Critical current anisotropy of GdBCO tapes grown on ISD-MgO buffered substrate *Supercond. Sci. Technol.* **28** 124002

[17] Cardwell D A and Ginley D S 2003 *Handbook of Superconducting Materials* (CRC Press)

[18] Ercolano G, Bianchetti M, Wimbush S C, Harrington S A, Wang H, Lee J H and MacManus-Driscoll J L 2011 State-of-the-art flux pinning in $YBa_2Cu_3O_{7-x}$ by the creation of highly linear, segmented nanorods of $Ba_2(YGd)(Nb/Ta)O_6$ together with nanoparticles of $(Y/Gd)_2O_3$ and $(YGd)Ba_2Cu_4O_8$ *Supercond. Sci. Technol.* **24** 95012

[19] Konczykowski M, Rullier-Albenque F, Yacoby E R, Shaulov A, Yeshurun Y and Lejay P 1991 Effect of 5.3-GeV Pb-ion irradiation on irreversible magnetization in Y-Ba-Cu-O crystals *Phys. Rev. B* **44** 7167–70

[20] Selvamanickam V, Xu A, Liu Y, Khatri N D, Lei C, Chen Y, Galstyan E and Majkic G 2014 Correlation between in-field critical currents in Zr-added (Gd,Y)$Ba_2Cu_3O_{7-x}$ superconducting tapes at 30 and 77 K *Supercond. Sci. Technol.* **27** 55010

[21] Gurevich A 2011 To use or not to use cool superconductors? *Nat. Mater.* **10** 255–9

[22] Adam J D, Boutboul T, Cavallari G, Charifoulline Z, Denarie C-H, Le Naour S, Leroy D F, Oberli L R, Richter D, Verweij A P and Wolf R 2002 Status of the LHC superconducting cable mass production *IEEE Trans. Appiled Supercond.* **12** 1056–62

[23] Mitchell N 2003 Summary, assessment and implications of the ITER model coil test results *Fusion Eng. Des.* **66–68** 971–93

[24] Sharma R G 1987 Review on the fabrication techniques of A-15 superconductors *Cryogenics (Guildf).* **27** 361–78

[25] Nagamatsu J, Nakagawa N, Muranaka T, Zenitani Y and Akimitsu J 2001 Superconductivity at 39 K in Magnesium Diboride *Nature* **410** 63–4

[26] Glowacki B A, Majoros M, Vickers M, Evetts J E, Shi Y and McDougall I 2001 Superconductivity of powder-in-tube MgB_2 wires *Supercond. Sci. Technol.* **14** 193–9

[27] Giunchi G, Ripamonti G, Cavallin T and Bassani E 2006 The reactive liquid Mg infiltration process to produce large superconducting bulk MgB_2 manufacts *Cryogenics (Guildf).* **46** 237–42

[28] Cai Z, Clarke R H, Glowacki B A, Nuttall W J and Ward N 2010 Ongoing ascent to the helium production plateau—Insights from system dynamics *Resour. Policy* **35** 77–89

[29] Buzea C and Yamashita T 2001 Review of the superconducting properties of MgB2 *Supercond. Sci. Technol.* **14** R115–46

[30] Fujishiro H and Tamura T 2012 Pulsed field magnetization of large MgB_2 bulk fabricated by reactive liquid mg infiltration *Jpn. J. Appl. Phys.* **51** 103005

[31] Yuan D and Kajuch J 1998 Process optimization for Ag-sheathed Bi-2212 superconductors *J. Supercond.* **11** 569–73

[32] Bernhard C, Wenger C and Niedermayer C 1995 Anisotropy and dimensional crossover of the vortex state in $Bi_2Sr_2CaCu_2O_{8+x}$ crystals *Phys. Rev. B* **52** 7050–3

[33] Group S research http://hoffman.physics.harvard.edu/research/STMresearch.php

[34] Dimos D, Chaudhari P and Mannhart J 1990 Superconducting transport properties of grain boundaries in $YBa_2Cu_3O_7$ bicrystals *Phys. Rev. B* **41** 4038–49

[35] Cyrot M and Pavuna D 1995 *Introduction to Superconductivity and High T_c materials.* (Singapore; London: World Scientific)

[36] Naito T, Sasaki T and Fujishiro H 2012 Trapped magnetic field and vortex pinning properties of MgB_2 superconducting bulk fabricated by a capsule method *Supercond. Sci. Technol.* **25** 95012

[37] Durrell J H, Dennis A R, Jaroszynski J, Ainslie M D, Palmer K G B, Shi Y-H, Campbell A M, Hull J, Strasik M, Hellstrom E E and Cardwell D A 2014 A trapped field of 17.6 T in melt-processed, bulk Gd-Ba-Cu-O reinforced with shrink-fit steel *Supercond. Sci. Technol.* **27** 82001

[38] Nariki S, Teshima H and Morita M 2016 Performance and applications of quench melt-growth bulk magnets *Supercond. Sci. Technol.* **29** 34002

[39] Sander M, Sutter U, Koch R and Klaser M 2000 Pulsed magnetization of HTS bulk parts at T <77 K *Supercond. Sci. Technol.* **13** 841–5

[40] Mizutani U, Oka T, Itoh Y, Yanagi Y, Yoshikawa M and Ikuta H 1998 Pulsed-field magnetization applied to high-T_c superconductors *Appl. Supercond.* **6** 235–46

[41] Fujishiro H, Tateiwa T, Fujiwara A, Oka T and Hayashi H 2006 Higher trapped field over 5T on HTSC bulk by modified pulse field magnetizing *Phys. C Supercond.* **445–448** 334–8

[42] Weinstein R, Parks D, Sawh R, Carpenter K and Davey K 2016 Anomalous results observed in magnetization of bulk high temperature superconductors - a windfall for applications *J. Appl. Phys.* **119** 133906

[43] Zhou D, Ainslie M D, Shi Y, Dennis A R, Huang K, Hull J R, Cardwell D A and Durrell J H 2017 A portable magnetic field of >3 T generated by the flux jump assisted, pulsed field magnetization of bulk

superconductors *Appl. Phys. Lett.* **110** 62601

[44] Mints R G 1996 Flux creep and flux jumping *Phys. Rev. B* **53** 12311–7

[45] Ainslie M D, Zhou D, Fujishiro H, Takahashi K, Shi Y-H and Durrell J H 2016 Flux jump-assisted pulsed field magnetisation of high-J_c bulk high-temperature superconductors *Supercond. Sci. Technol.* **29** 124004

[46] Yeshurun Y, Malozemoff A P, Holtzberg F and Dinger T R 1988 Magnetic relaxation and the lower critical fields in a Y-Ba-Cu-O crystal *Phys. Rev. B* **38** 11828–31

[47] Feigel'man M V., Geshkenbein V B, Larkin A I and Vinokur V M 1989 Theory of collective flux creep *Phys. Rev. Lett.* **63** 2303–6

[48] Weinstein R, Liu J, Ren Y, Sawh R, Parks D, Foster C and Obot V 1996 No Title *Proceedings 10th Anniversary HTS Workshop on Physics, Materials and Applications,* ed B Batlogg, C W Chu, W K Chu, D U Gubser and K A Muller (World Scientific, Singapore) p 625

[49] Vanderbemden P, Hong Z, Coombs T A, Denis S, Ausloos M, Schwartz J, Rutel I B, Hari Babu N, Cardwell D A and Campbell A M 2007 Behavior of bulk high-temperature superconductors of finite thickness subjected to crossed magnetic fields: Experiment and model *Phys. Rev. B* **75** 174515

[50] Jia Y, Welp U, Crabtree G W, Kwok W K, Malozemoff A P, Rupich M W, Fleshler S and Clem J R 2011 Microstructure dependence of the c-axis critical current density in second-generation YBCO tapes *J. Appl. Phys.* **110** 83923

[51] Baghdadi M, Ruiz H S and Coombs T A 2014 Crossed-magnetic-field experiments on stacked second generation superconducting tapes: Reduction of the demagnetization effects *Appl. Phys. Lett.* **104** 232602

[52] Campbell A, Baghdadi M, Patel A, Zhou D, Huang K Y, Shi Y and Coombs T 2017 Demagnetisation by crossed fields in superconductors *Supercond. Sci. Technol.* **30** 34005

[53] Brandt E H and Mikitik G P 2002 Why an ac Magnetic Field Shifts the Irreversibility Line in Type-II Superconductors *Phys. Rev. Lett.* **89** 27002

[54] Sundaram A, Zhang Y, Knoll A R, Abraimov D, Brownsey P, Kasahara M, Carota G M, Nakasaki R, Cameron J B, Schwab G, Hope L V, Schmidt R M, Kuraseko H, Fukushima T and Hazelton D W 2016 2G HTS wires made on 30 μm thick Hastelloy substrate *Supercond. Sci. Technol.* **29** 104007

[55] Hahn S, Voccio J, Bermond S, Park D-K, Bascuñán J, Kim S-B, Masaru T and Iwasa Y 2011 Field Performance of an Optimized Stack of YBCO Square "Annuli" for a Compact NMR Magnet. *IEEE Trans. Appl. Supercond.* **21** 1632–5

[56] Patel A, Filar K, Nizhankovskii V I, Hopkins S C and Glowacki B A 2013 Trapped fields greater than 7 T in a 12 mm square stack of commercial high-temperature superconducting tape *Appl. Phys. Lett.* **102** 102601

[57] Patel A, Hopkins S C and Glowacki B A 2013 Trapped fields up to 2 T in a 12 mm square stack of commercial superconducting tape using pulsed field magnetization *Supercond. Sci. Technol.* **26** 32001

[58] Durrschnabel M, Aabdin Z, Bauer M, Semerad R, Prusseit W and Eibl O 2012 $DyBa_2Cu_3O_{7-x}$ superconducting coated conductors with critical currents exceeding 1000 A cm^{-1} *Supercond. Sci. Technol.* **25** 105007

[59] Samoilenkov S, Molodyk A, Lee S, Petrykin V, Kalitka V, Martynova I, Makarevich A, Markelov A, Moyzykh M and Blednov A 2016 Customised 2G HTS wire for applications *Supercond. Sci. Technol.* **29** 24001

[60] Hari Babu N, Jackson K P, Dennis A R, Shi Y H, Mancini C, Durrell J H and Cardwell D A 2012 Growth of large sized $YBa_2Cu_3O_7$ single crystals using the top seeded melt growth process *Supercond. Sci. Technol.* **25** 75012

[61] Iida K, Babu N H, Shi Y and Cardwell D A 2005 Seeded infiltration and growth of large, single domain $YBa_2Cu_3O_7$ bulk superconductors with very high critical current densities *Supercond. Sci. Technol.* **18** 1421–7

[62] Zhou D, Hara S, Li B, Xu K, Noudem J and Izumi M 2013 Significant improvement of trapped flux in bulk Gd–Ba–Cu–O grains fabricated by a modified top-seeded melt growth process *Supercond. Sci. Technol.* **26** 15003

[63] Ainslie M D, Fujishiro H, Ujiie T, Zou J, Dennis A R, Shi Y-H and Cardwell D A 2014 Modelling and comparison of trapped fields in (RE)BCO bulk superconductors for activation using pulsed field

magnetization *Supercond. Sci. Technol.* **27** 65008

[64] Fujishiro H, Naito T and Oyama M 2012 Three-dimensional Simulation of Magnetic Flux Dynamics and Temperature Rise in HTSC Bulk during Pulsed Field Magnetization *Phys. Procedia* **36** 687–92

[65] Chaud X, Noudem J, Prikhna T, Savchuk Y, Haanappel E, Diko P and Zhang C P 2009 Flux mapping at 77K and local measurement at lower temperature of thin-wall YBaCuO single-domain samples oxygenated under high pressure *Phys. C Supercond.* **469** 1200–6

[66] Gautier-Picard P, Chaud X, Beaugnon E, Erraud A and Tournier R 1998 Growth of YBaCuO single-domains up to 7 cm *Mater. Sci. Eng. B* **53** 66–9

[67] STI Conductus process, http://www.suptech.com/the_conductus_process_n.php

[68] Fujishiro H, Yokoyama K, Kaneyama M, Oka T and Noto K 2005 Effect of Metal Ring Setting Outside HTSC Bulk Disk on Trapped Field and Temperature Rise in Pulse Field Magnetizing *IEEE Trans. Appiled Supercond.* **15** 3762–5

[69] Tomita M and Murakami M 2003 High-temperature superconductor bulk magnets that can trap magnetic fields of over 17 tesla at 29 K. *Nature* **421** 517–20

[70] Tomita M, Murakami M and Yoneda K 2002 Improvements in the mechanical properties of bulk YBCO superconductors with carbon fibre fabrics *Supercond. Sci. Technol.* **15** 803–7

[71] Leenders A, Mich M and Freyhard H 1997 Influence of thermal cycling on the mechanical properties of VGF melt-textured YBCO *Phys. C Supercond.* **279** 173–80

[72] Ceballos J M, Alvarez A, Suarez P, Amaro N and Perez B 2015 Device for Measuring the Thermal Cycling Degradation in 2G Tapes for Electrical Power Applications *IEEE Trans. Appl. Supercond.* **25** 6603603

[73] Tamegai T, Hirai T, Sun Y and Pyon S 2016 Trapping a magnetic field of 7.9 T using a bulk magnet fabricated from stack of coated conductors *Phys. C Supercond. its Appl.* **530** 20–3

[74] Fujishiro H, Ikebe M, Naito T, Noto K, Kohayashi S and Yoshizawa S 1994 Anisotropic Thermal Diffusivity and Conductivity of YBCO(123) and YBCO(211) Mixed Crystals. I *Jpn. J. Appl. Phys.* **33** 4965–70

[75] Patel A and Glowacki B A 2012 Enhanced trapped field achieved in a superconducting bulk using high thermal conductivity structures following simulated pulsed field magnetization *Supercond. Sci. Technol.* **25** 125015

[76] Baskys A, Patel A, Hopkins S, Kenfaui D, Chaud X, Zhang M and Glowacki B A 2014 Composite superconducting bulks for efficient heat dissipation during pulse magnetization *J. Phys. Conf. Ser.* **507** 12003

[77] Lousberg G P, Fagnard J-F, Chaud X, Ausloos M, Vanderbemden P and Vanderheyden B 2011 Magnetic properties of drilled bulk high-temperature superconductors filled with a ferromagnetic powder *Supercond. Sci. Technol.* **24** 35008

[78] Philippe M P, Fagnard J-F, Kirsch S, Xu Z, Dennis A R, Shi Y-H, Cardwell D A, Vanderheyden B and Vanderbemden P 2014 Magnetic characterisation of large grain, bulk $YBa_2Cu_3O_7$ superconductor-soft ferromagnetic alloy hybrid structures *Phys. C Supercond.* **502** 20–30

[79] Baskys A 2013 *Part III project:* Composite Superconducting Bulks for Efficient Heat Dissipation During Pulse Magnetization (Cambridge)

[80] Gamble B, Snitchler G and MacDonald T 2011 Full Power Test of a 36.5 MW HTS Propulsion Motor *IEEE Trans. Appl. Supercond.* **21** 1083–8

[81] Luongo C A, Masson P J, Nam T, Mavris D, Kim H D, Brown G V., Waters M and Hall D 2009 Next generation more-electric aircraft: a potential application for hts superconductors *IEEE Trans. Appl. Supercond.* **19** 1055–68

[82] Berg F, Palmer J, Miller P and Dodds G 2017 HTS System and Component Targets for a Distributed Aircraft Propulsion System *IEEE Trans. Appl. Supercond.* **27** 3600307

[83] Snitchler G, Gamble B, King C and Winn P 2011 10 MW class superconductor wind turbine generators *IEEE Trans. Appl. Supercond.* **21** 1089–92

[84] Zhang Y, Zhou D, Ida T, Miki M and Izumi M 2016 Melt-growth bulk superconductors and application to an axial-gap-type rotating machine *Supercond. Sci. Technol.* **29** 44005

[85] Zhou D, Izumi M, Miki M, Felder B, Ida T and Kitano M 2012 An overview of rotating machine systems with high-temperature bulk superconductors *Supercond. Sci. Technol.* **25** 103001

[86] Nishijima S, Mishima F, Tabata Y, Iseki H, Muragaki Y, Sasaki A and Saho N 2009 Research and Development of Magnetic Drug Delivery System Using Bulk High Temperature Superconducting Magnet *IEEE Trans. Appl. Supercond.* **19** 2257–2260

[87] Nishijima S, Takeda S, Mishima F, Tabata Y, Yamamoto M, Joh J, Iseki H, Muragaki Y, Sasaki A, Jun K and Saho N 2008 A Study of Magnetic Drug Delivery System Using Bulk High Temperature Superconducting Magnet *IEEE Trans. Appl. Supercond.* **18** 874–7

[88] Saho N, Nishijima N, Tanaka H and Sasaki A 2009 Development of portable superconducting bulk magnet system *Phys. C Supercond. its Appl.* **469** 1286–9

[89] Oka T, Kanayama H, Tanaka K, Fukui S, Ogawa J, Sato T, Yamaguchi M, Ooizumi M, Yokoyama K and Noto K 2009 Study on magnetic separation system using high T_c superconducting bulk magnets for water purification technique *J. Phys. Conf. Ser.* **156** 12031

[90] Yokoyama K, Oka T, Okada H, Fujine Y, Chiba A and Noto K 2003 Solid-liquid magnetic separation using bulk superconducting magnets *IEEE Trans. Appiled Supercond.* **13** 1592–5

[91] Wera L, Fagnard J-F, Namburi D K, Shi Y, Vanderheyden B and Vanderbemden P 2017 Magnetic Shielding Above 1 T at 20 K With Bulk, Large Grain YBCO Tubes Made by Buffer-Aided Top Seeded Melt Growth *IEEE Trans. Appl. Supercond.* **27** 6800305

[92] Wera L, Fagnard J F, Levin G A, Vanderheyden B and Vanderbemden P 2013 Magnetic Shielding With YBCO Coated Conductors: Influence of the Geometry on Its Performances *IEEE Trans. Appl. Supercond.* **23** 8200504

[93] Rabbers J J, Oomen M P, Bassani E, Ripamonti G and Giunchi G 2010 Magnetic shielding capability of MgB_2 cylinders *Supercond. Sci. Technol.* **23** 125003

[94] Earnshaw S 1842 On the Nature of the Molecular Forces which Regulate the Constitution of the Luminiferous Ether *Trans. Camb. Phil. Soc.* **7** 97–114

[95] Werfel F N, Floegel-Delor U, Rothfeld R, Riedel T, Goebel B, Wippich D and Schirrmeister P 2012 Superconductor bearings, flywheels and transportation *Supercond. Sci. Technol.* **25** 14007

[96] Strasik M, Johnson P E, Day A C, Mittleider J, Higgins M D, Edwards J, Schindler J R, McCrary K E, McIver C R, Carlson D, Gonder J F and Hull J R 2007 Design, Fabrication, and Test of a 5-kWh/100-kW Flywheel Energy Storage Utilizing a High-Temperature Superconducting Bearing *IEEE Trans. Appl. Supercond.* **17** 2133–7

[97] Wang J, Wang S, Zeng Y, Huang H, Luo F, Xu Z, Tang Q, Lin G, Zhang C, Ren Z, Zhao G, Zhu D, Wang S, Jiang H, Zhu M, Deng C, Hu P, Li C, Liu F, Lian J, Wang X, Wang L, Shen X and Dong X 2002 The first man-loading high temperature superconducting Maglev test vehicle in the world *Phys. C Supercond. its Appl.* **378–381** 809–14

[98] Mattos L S, Rodriguez E, Costa F, Sotelo G G, de Andrade R and Stephan R M 2016 MagLev-Cobra Operational Tests *IEEE Trans. Appl. Supercond.* **26** 3600704

[99] Schultz L, De Haas O, Verges P, Beyer C, Röhlig S, Olsen H, Kühn L, Berger D, Noteboom U and Funk U 2005 Superconductively levitated transport system-the SupraTrans project *IEEE Trans. Appl. Supercond.* **15** 2301–5

[100] Takeda H 1990 Japanese superconducting maglev: Present state and future perspective *Phys. B Condens. Matter* **164** 229–35

[101] Patel A, Hahn S, Voccio J, Baskys A, Hopkins S C and Glowacki B A 2017 Magnetic levitation using a stack of high temperature superconducting tape annuli *Supercond. Sci. Technol.* **30** 24007

[102] Patel A, Hopkins S C, Baskys A, Kalitka V, Molodyk A and Glowacki B A 2015 Magnetic levitation using high temperature superconducting pancake coils as composite bulk cylinders *Supercond. Sci. Technol.* **28** 115007

[103] Patel A, Kalitka V, Hopkins S C, Baskys A, Albisetti A F, Giunchi G, Molodyk A and Glowacki B A 2016 Magnetic Levitation Between a Slab of Soldered HTS Tape and a Cylindrical Permanent Magnet *IEEE Trans. Appl. Supercond.* **26** 3601305

[104] Strasik M, Hull J R, Mittleider J a, Gonder J F, Johnson P E, McCrary K E and McIver C R 2010 An

overview of Boeing flywheel energy storage systems with high-temperature superconducting bearings *Supercond. Sci. Technol.* **23** 34021

[105] Nakamura T, Tamada D, Yanagi Y, Itoh Y, Nemoto T, Utumi H and Kose K 2015 Development of a superconducting bulk magnet for NMR and MRI *J. Magn. Reson.* **259** 68–75

[106] Hahn S, Kim Y, Song J, Voccio J P, Chu Y, Bascunan J, Tomita M and Iwasa Y 2015 Operation of a 130-MHz/9-mm Compact HTS Annulus Magnet With a Micro-NMR Probe *IEEE Trans. Appl. Supercond.* **25** 4300905

[107] Zermeño V M R, Habelok K, Stępień M and Grilli F 2017 A parameter-free method to extract the superconductor's $J_c(B,\theta)$ field-dependence from in-field current–voltage characteristics of high temperature superconductor tapes *Supercond. Sci. Technol.* **30** 34001

[108] Hopkins S C, Woźniak M, Glowacki B A, Chen Y, Kesgin I and Selvamanickam V 2012 Two-axis Magnetic Field Orientation Dependence of Critical Current in Full-Width REBCO Coated Conductors *Phys. Procedia* **36** 582–7

[109] Grilli F 2016 Numerical modeling of HTS applications *IEEE Trans. Appl. Supercond.* **26** 500408

[110] Sirois F and Grilli F 2015 Potential and limits of numerical modelling for supporting the development of HTS devices *Supercond. Sci. Technol.* **28** 43002

[111] Goodrich L F and Stauffer T C 2001 Hysteresis in transport critical-current measurements of oxide superconductors *IEEE Trans. Appiled Supercond.* **11** 3234–7

[112] Nishijima G, Kitaguchi H, Tshuchiya Y, Nishimura T and Kato T 2013 Transport critical current measurement apparatus using liquid nitrogen cooled high-Tc superconducting magnet with variable temperature insert *Rev. Sci. Instrum.* **84** 15113

[113] Baskys A, Hopkins S C, Bader J and Glowacki B A 2016 Forced flow He vapor cooled critical current testing facility for measurements of superconductors in a wide temperature and magnetic field range *Cryogenics (Guildf).* **79** 1–6

[114] Ekin J W, Clark A F and Ho J C 1978 Current transfer in multifilamentary superconductors. II. Experimental results *J. Appl. Phys.* **49** 3410

[115] Polak M, Zhang W, Parrell J, Cai X Y, Polyanskii A, Hellstrom E E, Larbalestier D C and Majoros M 1997 Current transfer lengths and the origin of linear components in the voltage - current curves of Ag-sheathed BSCCO components *Supercond. Sci. Technol.* **10** 769–77

[116] Miyoshi Y, Nishijima G, Kitaguchi H and Chaud X 2015 High field Ic characterizations of commercial HTS conductors *Phys. C Supercond. its Appl.* **516** 31–5

[117] Roth B J, Sepulveda N G and Wikswo J P 1989 Using a magnetometer to image a two-dimensional current distribution *J. Appl. Phys.* **65** 361–72

[118] Higashikawa K, Inoue M, Kawaguchi T, Shiohara K, Imamura K, Kiss T, Iijima Y, Kakimoto K, Saitoh T and Izumi T 2011 Scanning Hall-probe microscopy system for two-dimensional imaging of critical current density in RE-123 coated conductors *Phys. C Supercond.* **471** 1036–40

[119] Patel A, Giunchi G, Albisetti A F, Shi Y, Hopkins S C, Palka R, Cardwell D A and Glowacki B A 2012 High Force Magnetic Levitation Using Magnetized Superconducting Bulks as a Field Source for Bearing Applications *Phys. Procedia* **36** 937–42

[120] Zhang M and Coombs T A 2012 3D modeling of high-T_c superconductors by finite element software *Supercond. Sci. Technol.* **25** 15009

[121] Fujita S, Daibo M, Igarashi M, Kikutake R, Kakimoto K, Iijima Y, Itoh M and Saitoh T 2014 In-field critical current property of IBAD/PLD coated conductors *J. Phys. Conf. Ser.* **507** 22007

[122] Yamasaki H and Mawatari Y 1999 Current-voltage characteristics of melt-textured YBCO obtained from the field-sweep rate dependence of magnetization *IEEE Trans. Appiled Supercond.* **9** 2651–4

[123] Chudy M, Zhong Z, Eisterer M and Coombs T 2015 n-Values of commercial YBCO tapes before and after irradiation by fast neutrons *Supercond. Sci. Technol.* **28** 35008

[124] Duron J, Grilli F, Dutoit B and Stavrev S 2004 Modelling the E-J relation of high-Tc superconductors in an arbitrary current range *Phys. C Supercond. its Appl.* **401** 231–5

[125] Van Sciver S W 2012 *Helium Cryogenics* (New York, NY: Springer New York)

[126] Lu J, Choi E S and Zhou H D 2008 Physical properties of Hastelloy® C-276™ at cryogenic temperatures

J. Appl. Phys. **103** 64908

[127] Smith D R and Fickett F R 1995 Low-Temperature Properties of Silver *J. Res. Natl. Inst. Stand. Technol.* **100** 119–70

[128] Swenson C A 1997 Linear thermal expansivity (1.5–300 K) and heat capacity (1.2–90 K) of Stycast 2850FT *Rev. Sci. Instrum.* **68** 1312

[129] Page A G, Patel A, Baskys A, Hopkins S C, Kalitka V, Molodyk A and Glowacki B A 2015 The effect of stabilizer on the trapped field of stacks of superconducting tape magnetized by a pulsed field *Supercond. Sci. Technol.* **28** 85009

[130] Patel A, Baskys A, Hopkins S C, Kalitka V, Molodyk A and Glowacki B A 2015 Pulsed-Field Magnetization of Superconducting Tape Stacks for Motor Applications *IEEE Trans. Appl. Supercond.* **25** 5203405

[131] Baskys A, Patel A, Hopkins S C, Kalitka V, Molodyk A and Glowacki B A 2015 Self-supporting stacks of commercial superconducting tape trapping fields up to 1.6 T using pulsed field magnetization *IEEE Trans. Appl. Supercond.* **25** 6600304

[132] Preuss A, Wolf M J and Fietz W H 2016 Critical current degradation of commercially available coated conductors due to short thermal loads *Applied Superconductivity Conference* (Denver)

[133] Pishchik V, Lytvynov L A and Dobrovinskaya E R 2009 *Sapphire* (Boston, MA: Springer US)

[134] Zou S, Zermeño V M R, Baskys A, Patel A, Grilli F and Glowacki B A 2017 Simulation and experiments of stacks of high temperature superconducting coated conductors magnetized by pulsed field magnetization with multi-pulse technique *Supercond. Sci. Technol.* **30** 14010

[135] Baskys A, Patel A, Hopkins S and Glowacki B 2016 Modeling of trapped fields by stacked (RE)BCO tape using angular transversal field dependency *IEEE Trans. Appl. Supercond.* **26** 6601004

[136] Ainslie M D and Fujishiro H 2015 Modelling of bulk superconductor magnetization *Supercond. Sci. Technol.* **28** 53002

[137] Patel A and Glowacki B A 2014 Optimisation of composite superconducting bulks made from (RE)BCO coated conductor stacks using pulsed field magnetization modelling *J. Phys. Conf. Ser.* **507** 22024

[138] Chudý M, Hopkins S C, Woźniak M, Glowacki B A, Eisterer M and Weber H W 2011 Full angular critical current characteristics of coated conductors studied using a two-axis high current goniometer *Supercond. Sci. Technol.* **24** 75018

[139] Yamafuji K and Kiss T 1996 A new interpretation of the glass-liquid transition of pinned fluxoids in high-Tc superconductors *Phys. C Supercond.* **258** 197–212

[140] Zermeño V M R, Baskys A, Zou S, Patel A and Grilli F 2016 Estimation of maximum possible trapped field in superconducting permanent magnets in 2D and 3D (submitted)

[141] Goldacker W, Grilli F, Pardo E, Kario A, Schlachter S I and Vojenčiak M 2014 Roebel cables from REBCO coated conductors: a one-century-old concept for the superconductivity of the future *Supercond. Sci. Technol.* **27** 93001

[142] Mitchell-Williams T B, Baskys A, Hopkins S C, Kalitka V, Molodyk A, Glowacki B A and Patel A 2016 Uniform trapped fields produced by stacks of HTS coated conductor tape *Supercond. Sci. Technol.* **29** 85008

[143] Selva K, Li X-F, Majkic G and Masson P 2015 Assessment of critical factors affecting the performance of trapped field magnets using thin film superconductor tapes *IOP Conf. Ser. Mater. Sci. Eng.* **102** 12031

[144] Krings A, Mousavi S A, Wallmark O and Soulard J 2013 Temperature Influence of NiFe Steel Laminations on the Characteristics of Small Slotless Permanent Magnet Machines *IEEE Trans. Magn.* **49** 4064–7

Appendix A Critical current reconstruction using Hall probe magnetometry

This section contains Matlab code written for current density reconstruction in a thin film and based on algorithm described in [117,118].

A.1 Matlab code

```
function [X, Y, J, Bz0] = current_density(data, z, bg, res, calib)
% current_density computes the current density in a thin film from the flux
% density above the film (component parallel to the tape normal).
% Input parameters:
% data:  the measured Hall voltage in grid form where first column and
%       first row are the X and Y coordinates;
% z:    height above the film where the magnetic flux density is measured;
% bg:   voltage offset due to background field of hall sensor;
% res:  smoothing of the reconstruction to limit noise.
% calib: calibration of the Hall probe.
%
% Output parameters:
% X:    vecotr with all X coordinates
% Y:    vector with all Y coordinates
% J:    3D array, slices of which contain X and Y components and the
%       modulus of current density
% Bz0:  flux density extrapolated to the surface of the film

% Preconditioning data and assigning variables
Y=data(1,2:end);
X=data(2:end,1);

dx=(X(size(X,1))-X(1))/(size(X,1)-1);
dy=(Y(size(Y,2))-Y(1))/(size(Y,2)-1);

data(1,:)=[];
data(:,1)=[];

calib_data=(data-bg)*calib*1e-3;
```

```
sz=size(calib_data);
cx=floor(sz(2)/2 +1);    % indices of zero frequency component
cy=floor(sz(1)/2 +1);

kcut=2*pi/res;           % cut-off frequency for high frequency noise

dkx=2*pi/(dx*(sz(2)-1));% step size in frequency domain
dky=2*pi/(dy*(sz(1)-1));

ft=fft2(ifftshift(calib_data));
shfft=fftshift(ft);

% Translating to magnetic field at the surface of the tape

Bz0ft = zeros(sz(1), sz(2));

for j=1:sz(1)
    for k=1:sz(2)
        Bz0ft(j,k)=exp(sqrt( ((j-cy)*dky)^2 + ((k-cx)*dkx)^2
)*z)*shfft(j,k);
    end
end

% Filter mask, for filtering out highest spatial frequencies (k>kcut)

window = zeros(sz(1), sz(2));

for j=1:sz(1)
    for k=1:sz(2)
        k_val=sqrt(((cy-j)*dky)^2+ ((cx-k)*dkx)^2);

        if ( k_val < kcut)
            window(j,k)=(1+cos(pi*k_val/kcut))/2;
        else
            window(j,k)=0;
        end
    end
end

% Filtered FFT of Bz0

Bz0ft_filtered = times(Bz0ft, window);
Bz0 = fftshift(ifft2(ifftshift(Bz0ft_filtered)));
```

```
% Finding Jx:

Jxft=zeros(sz(1),sz(2));

for j=1:sz(1)
    for k=1:sz(2)
        Jxft(j,k)=-1i*2*(j-cy)*dky*Bz0ft_filtered(j,k)/((1.256e-6)*sqrt(
((j-cy)*dky)^2 + ((k-cx)*dkx)^2 ));
        if k==cx && j==cy
            Jxft(j,k) = 0;
        end
    end
end

Jx=fftshift(ifft2(ifftshift(Jxft)));

% Finding Jy:

Jyft=zeros(sz(1),sz(2));

for j=1:sz(1)
    for k=1:sz(2)
        Jyft(j,k)=1i*2*(k-cx)*dkx*Bz0ft_filtered(j,k)/((1.256e-6)*sqrt(
((j-cy)*dky)^2 + ((k-cx)*dkx)^2 ));

        if k==cx && j==cy
            Jyft(j,k) = 0;
        end
    end
end

Jy=fftshift(ifft2(ifftshift(Jyft)));

% Finding modulus of current density JJ:

JJ = sqrt(times(Jy,Jy)+times(Jx, Jx));

J=cat(3, Jx, Jy, JJ);
```